

Bergische Universität -GH- Wuppertal
Fachbereich Elektrotechnik und Informationstechnik,
Institut für Materialwissenschaften

Structural and Optical Characterisation of Si/Si_{1-x}Ge_x Multiple Quantum Wells

PhD Thesis submitted by

Tamim P. Sidiki

Thesis supervised by

Prof. Dr. C.M. Sotomayor Torres

To my parents for
their continuous love,
support and patience.

Table of Context

Table of Context

German Summary

1. Introduction.....	1
2. Si and SiGe Heterostructures.....	6
2.1. Epitaxial Growth of Si and SiGe Layers.....	6
2.1.1. Molecular Beam Epitaxy.....	6
2.1.2. Rapid Thermal Chemical Vapour Deposition.....	7
2.2. Properties of Si/SiGe Heterostructures.....	9
2.2.1. The Concept of Pseudomorphic Growth.....	9
2.2.2. Heteroepitaxial Growth Modes.....	11
2.2.3. Band Structure.....	12
2.2.4. Quantum Confinement.....	18
2.2.5. Thermal Relaxation.....	25
2.2.6. Formation of Misfit Dislocation.....	26
3. Principles of Analytical Techniques.....	27
3.1. Secondary Ion Mass Spectroscopy.....	27
3.2. Photoluminescence Spectroscopy.....	28
3.2.1. Exciton Recombination.....	31
3.2.2. The Electron Hole Droplet Emission.....	35
3.2.3. T-Band Luminescence.....	38
3.3. Electroluminescence Spectroscopy.....	39
3.4. Raman Spectroscopy.....	40
3.5. X-ray Techniques.....	42
3.5.1. Refraction law for x-rays.....	42
3.5.2. Reflected and transmitted x-ray wavefields.....	44
3.5.3. Parrat-Formalism.....	47
3.5.4. X-ray Diffraction.....	49
3.5.5. X-ray Topography.....	50
3.6. Scanning Electron Microscopy.....	51
3.7. High Resolution Transmission Electron Microscopy.....	54
4. Experimental Setup.....	56
4.1. X-Ray Diffraction and Reflectivity.....	56

Table of Context

4.1.1. Sample Alignment	57
4.1.2. Illumination Correction.....	57
4.2. Photo- and Electroluminescence.....	58
4.3. Raman Spectroscopy.....	62
4.4. High Vacuum-Thermal Evaporator for ITO Deposition	65
4.4.1. Pumping System	66
4.4.2. Substrate Heater and Sample Holder	67
4.4.3. Pressure Measurement	67
4.4.4. Oxygen Supply.....	68
4.4.5. Evaporation Rates and Quartz Monitor	68
4.4.6. Tooling Factor.....	69
4.4.7. Electrical Characterisation:	70
5. Results and Discussion	72
5.1. MBE Samples	72
5.1.1. Emission Spectrum	73
5.1.2. Phonon Spectrum.....	79
5.1.3. Structural Properties.....	79
5.2. RTCVD Samples	85
5.2.1. Emission Spectrum	86
5.2.2. Structural Characterisation.....	99
5.3. Comparison of MBE and RTCVD Samples	105
5.4. Electroluminescence	109
5.4.1. Structure of the EL-Diode.....	109
5.4.2. PL of the EL structure.....	111
5.4.3. Contact Deposition	111
5.4.4. Electroluminescence Set-up.....	119
5.4.5. EL Spectrum	120
5.4.6. I-V Characteristics	122
5.4.7. Comparison of the EL- and PL-Spectrum	123
5.4.8. EL-Intensity as a Function of Current Density.....	124
5.4.9. Power Efficiency.....	125
6. Conclusions and Outlook.....	127

Publications

List of Publications arising from this work:

- 1) T.P. Sidiki and C.M. Sotomayor Torres, “*Silicon-Based Nanostructures*”, invited chapter in "Handbook of Nanostructured Materials and Nanotechnology", Vol.3, Chapter 5, 233-289, H.S. Nalwa (ed.), Academic Press (1999)
- 2) T.P. Sidiki, A. Rühm, W.-X. Ni, G.V. Hansson and C.M. Sotomayor Torres, “*Photoluminescence and x-ray characterisation of Si/Si_{1-x}Ge_x multiple quantum wells*”, Jour. of Luminescence 80, 503-507 (1999)
- 3) T.P. Sidiki and C.M. Sotomayor Torres, “*Silicon-Based Optoelectronics: Progress and Challenges*”, Tr. J. of Physics 23, 665-672, 1999
- 4) A. Rühm, T.P. Sidiki, W.B. de Boer, W.-X. Ni, T. Köpke and C.M. Sotomayor Torres, “*A study of growth temperature on interface quality and luminescence of Si/SiGe multiple-quantum wells*”, in “Lattice-Mismatched Thin Films”, E.A. Fitzgerald (ed.), 47-52, The Minerals, Metals & Materials Society, Cambridge (2000)
- 5) T. Sidiki, S. H. Christiansen, S. Chabert , W.B. de Boer, C. Ferrari , H.P. Strunk and C.M. Sotomayor Torres, “*Optical and structural characterisation of Si/SiGe heterostructures grown by RTCVD*”, Thin Solid Films 369, 431-435, 2000
- 6) T. P. Sidiki, C. Ferrari, S. H. Christiansen, M. Albrecht, W.B. de Boer, and C.M. Sotomayor Torres, “*Impact of the SiGe/Si interface structure upon the low temperature photoluminescence of a Si/Si_{1-x}Ge_x multiple quantum well*”, Materials Science in Semiconductor Processing 140, 1-5 (2000)
- 7) T.P. Sidiki and C.M. Sotomayor Torres, “*Carrier confinement in SiGe quantum wells, wires and dots*”, Chapter 5.1 in *Properties of strained and relaxed SiGe*, 2nd Edition, 181-195, E. Kasper, K. Lyutovich (Ed.), EMIS Datareviews Series No. 24, INSPEC (2000)
- 8) N. Roos, T.P. Sidiki, J. Seekamp and C.M. Sotomayor Torres, “*Self-Organized Growth of Indium-Tin-Oxide Nanowires*”, Proc. 14th International Winterschool on Electronic Properties of Novel Materials 2000, American Institute of Physics (in press)

German Summary

Zusammenfassung

Die vorliegende Arbeit behandelt im wesentlichen zwei Aspekte. Der erste Teil hat die Untersuchung struktureller und optischer Eigenschaften von Si/SiGe Multi Quantum Wells zum Gegenstand. Ziel der Arbeit war es insbesondere, den Einfluß lateraler Ge-Cluster in den SiGe Schichten sowie den Einfluß der SiGe/Si Grenzflächenrauigkeit auf die Photolumineszenz zu untersuchen.

Um die externe Quanteneffizienz von Si/SiGe Leuchtdioden zu erhöhen, wurde als zweiter Schwerpunkt dieser Arbeit gezeigt, daß die ternäre Legierung Indium-Zinn-Oxid (ITO) für den Einsatz als Top-Kontakt bei Si/SiGe Leuchtdioden geeignet ist.

Als Meßmethoden wurden Röntgenreflektivität und -streuung, Röntgentopographie, Sekundärelektronen-Massenspektroskopie, Transmissions-Elektronenmikroskopie, Photolumineszenz- und Ramanspektroskopie angewandt. Die unterschiedlichen Charakterisierungsmethoden ergänzen sich und erlauben eine gegenseitige Überprüfung der Ergebnisse. In dieser Arbeit wurde der Effekt der Schicht- und Grenzflächenstruktur auf die optischen Lumineszenzeigenschaften im Wesentlichen in fünf Teilaspekten behandelt:

- 1) Im ersten Teil wurde die Struktur der Si/SiGe Multiquantum Wells optimiert, so daß Photo- und Elektrolumineszenz bei Raumtemperatur möglich waren. Hierbei führte eine Quantum Well Dicke von 4 nm bei einer Ge-Konzentration von 23% zu einem ausreichenden Confinement der Ladungsträger, so daß trotz einer starken, thermisch bedingten Intensitätsschwächung noch Photolumineszenz bei Raumtemperatur vorhanden war.
- 2) Im zweiten Teil der Arbeit wurde gezeigt, daß entgegen jüngster Veröffentlichungen einer anderen Forschungsgruppe die Bildung von Ge-Clustern innerhalb der SiGe Legierung nicht zu einer Reduktion der Photolumineszenz führt. Vielmehr kann angenommen werden, daß Defekte und Verunreinigungen in den SiGe-Schichten zu der erwähnten Reduktion der Photolumineszenz geführt haben.
- 3) Im dritten Teil wurden mögliche Effekte von Exzitonenstreuung oder Lokalisierung durch rauhe SiGe/Si Grenzflächen untersucht. Es ergab sich ein relativ geringer Effekt von Grenzflächenrauigkeit auf die Photolumineszenzeigenschaften. Lediglich im Falle sehr rauher Grenzflächen können Potentialfluktuationen an der Grenzfläche zu einer Lokalisierung von Excitonen und damit zu einer Verschiebung der Photolumineszenz um etwa 8 meV zu höheren Energien führen. Die relevante Längenskala hierbei ist der Exziton Bohr Radius als Grenzwert für

German Summary

Lokalisierungseffekte. Sind die Potentialfluktuationen an der Grenzfläche kleiner als der Exziton Bohr Radius, dann mittelt die Exciton Wellenfunktion über diese Schwankungen hinweg ohne davon beeinflusst zu werden. Im Falle sehr großer Fluktuationen in der Größenordnung des Bohr Radius, für SiGe mit einer Ge-Konzentration von 23% ca. 7-8 nm, kommt es zu einer Exziton-Lokalisierung.

- 4) Im vierten Teil der Arbeit wurde die Defektlumineszenz in Gruppe-IV Halbleiter-Heterostrukturen behandelt. Aktuell wird die Bedeutung einer metallischen Dekoration von Versetzungen in Si Kristallen diskutiert. In dieser Arbeit konnte gezeigt werden, daß zusätzlich zur Existenz von Versetzungen auch eine Dekoration dieser Versetzungen mit einem Metall wie z.B. Eisen nötig ist, um in dieser Versetzung eine strahlende Rekombination von Ladungsträgern zu induzieren.
- 5) Im letzten Teil dieser Arbeit wurde eine Si/SiGe Leuchtdiode hergestellt. Hierbei ist zum ersten Mal die ternäre Indium-Zinn-Oxid Legierung (ITO) als ohmscher Kontakt für Si/Si_{1-x}Ge_x Heterostrukturen benutzt worden. Ein wichtiger Schritt bestand im Aufbau einer thermischen Verdampfungsanlage für ITO in Zusammenarbeit mit der Firma MBE-Komponenten. Es konnten ITO Schichten mit einer Transparenz von ca. 90% im sichtbaren Spektralbereich und mit ca. 60 - 80% im Bereich 1.2-1.3 µm hergestellt werden, in dem auch die Si/SiGe Leuchtdiode ihr Emissionsmaximum hat. Solche Schichten haben einen Flächenwiderstand von ca. 2000 µΩcm. Aufgrund eines starken Loch-Confinements in den SiGe Schichten zeigte die Leuchtdiode Elektrolumineszenz bis Raumtemperatur. Die Leistungs-Effizienz war jedoch mit 10⁻⁹ gering. In dieser Arbeit sollte gezeigt werden, daß man auf eine relativ einfache Weise ohmsche ITO Kontakte für den Einsatz bei Leuchtdioden herstellen kann. Auf diese Weise kann man die bei Halbleiter-Leuchtdioden üblichen metallischen Kontakte mit hoher Absorption durch ITO Kontakte mit sehr geringer Absorption ersetzen. Da das Wachstum der ITO Schichten unabhängig vom zugrundeliegenden Substrat ist, eignet sich dieses Material sowohl für III-V als auch für II-VI oder IV-IV Systeme.

1. Introduction

The realisation of photonic based Si/Si_{1-x}Ge_x microstructures is of considerable technological interest. Monolithic integration of mature Silicon technology with Silicon-based optoelectronic devices would open the field of optical signal processing to the Silicon world.

Beside porous silicon [1-3] and erbium doped Si [4-7] one promising approach to achieve an efficient light-emitting Silicon-based material is the synthesis of pseudomorphic Si/Si_{1-x}Ge_x quantum wells. Silicon-Germanium (SiGe) alloys are very attractive for monolithic integration of Si-based photonic and high-speed electronic devices with state-of-the-art CMOS chips. Preserving almost 100% compatibility with mainstream Si technology it provides at least a doubling of the heterojunction bipolar transistors (HBTs) speed [8]. Moreover, the SiGe alloy is a favoured candidate for optoelectronic applications as it can extend the detection wavelength range of Si, enabling the integration of waveguides, photodetectors and potentially also emitters. There are three key parameters of SiGe permitting an enhanced flexibility in material properties and device characteristics: alloy concentration, strain and heterostructure design in order to confine carriers in quantum wells. Si/SiGe quantum wells, wires and dots have attracted much attention because reduced dimensions lead to modifications in the band structure providing a possibility to realise optoelectronic as well as high-speed electronic devices.

Since visible light emission from porous silicon was observed in 1990 by Canham [1], which could be correlated to the creation of quantum wire-like structures with their modified electronic states, many different approaches to realise nanostructures have been tried. The Si/SiGe heterostructure was one attractive possibility to overcome the poor light emission of the indirect gap semiconductors Si and Ge, which gave new hopes to realise an all-optical Si-based chip system. A multi-article status report on silicon-based optoelectronics has been published in the Materials Research Society Bulletin issue of April 1998.

Due to confinement of carriers in the lower band-gap Si_{1-x}Ge_x quantum well layers, an efficient pumping mechanism overcomes the inherent low emission rates in Si_{1-x}Ge_x alloys due to the indirect fundamental gap. Although light emission from SiGe multiple quantum wells does not fulfil the demands for their use in optical interconnects, some promising results have been achieved leading to luminescence even at room temperature. To improve the light emission further, the radiative recombination mechanisms should be clarified in more detail.

1. Introduction

This thesis deals mainly with two aspects:

-) The first part deals with the effect of structural properties, i.e. Ge clusters in the SiGe alloy and SiGe interface roughness on the photoluminescence.

Despite extensive research on SiGe alloys since about 1975, the role of key epitaxial growth parameters in the emission strength were not clear. It was the contribution by the Hitachi research group [10-11] which reported a strong reduction of photoluminescence (PL) intensity from Si/SiGe multiple quantum wells grown by molecular beam epitaxy (MBE) in a certain range of substrate temperatures. In the lower part of Figure 1 (left) PL spectra of Si/Si_{0.7}Ge_{0.3} MQW samples grown at 300 °C, 500 °C and 800 °C are shown. SiGe band edge emission is only visible for the sample grown at 800 °C. Crystal imperfections in the low-temperature MBE growth were considered to decrease the PL intensity.

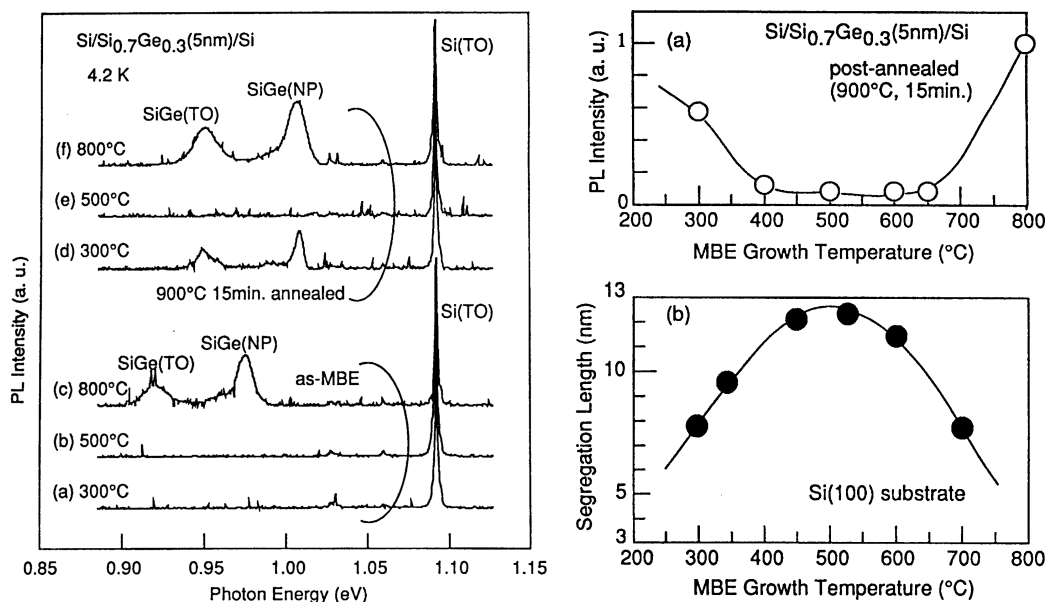


Figure 1: PL spectra of Si/SiGe MQW samples grown at 300 °C, 500 °C and 800 °C (bottom left) and PL spectra of the same samples after annealing at 900°C for 15 min (top left). PL intensity of the SiGe^{NP} line after annealing as a function of the growth temperature together with the Ge segregation length as a function of growth temperature (right) ([10]).

To improve the crystalline quality these authors carried out post-annealing experiments at 900 °C for 15 min in N₂ ambient. The PL spectra of such treated samples are shown in the upper part of Figure 1 (left). Whereas the sample grown at 300 °C now clearly shows SiGe related photoluminescence and the luminescence intensity increases for the sample grown at 800 °C, there is no photoluminescence observable for the sample grown at 500 °C.

1. Introduction

The upper part of Figure 1 (right) shows the PL intensity of annealed samples grown at various temperatures. The PL intensity seemed to be very weak for growth temperatures ranging between 400 and 650 °C. The authors argued that such a reverse temperature dependence of the photoluminescence intensity could not be explained by the improvement of the crystalline quality during post-annealing. The lower part of Figure 1 (right) shows the surface segregation length of Ge atoms during the growth measured by x-ray photoelectron spectroscopy [12]. With increasing growth temperature the Ge segregation length increased to a maximum at around 500 °C and then drops again at higher growth temperatures as the diffusion gets more and more isotropic and Ge atoms thus also diffuse into the substrate.

From these results the authors concluded that PL intensity was very low for temperatures where Ge surface segregation was active. As a potential mechanism they suggested clustering of Ge atoms to be responsible for this intensity decrease. These authors [10-11] even suggested this Ge clustering as a new model instead of the common explanation of alloy-scattering for the no-phonon emission in SiGe alloys. Based on local density approximation and the pseudopotential method they calculated electron probabilities at the valence band bottom and the conduction band top in $\text{Si}_{1-x}\text{Ge}_x$ mixed crystals. When Ge is dispersed in Si, s-like symmetry appears. This was explained due to charge transfer between Si and Ge in strained Si-Ge bonds as also present in III-V compounds. Forming Ge clusters relaxes the strain field and the local symmetry of Si-Ge bonds is modified from s-like to p-like making the dipole transition probability to disappear. However, these reports were regarded very critically in the SiGe community as no-one else had made such observations and because the local density approximation is developed for systems with a large electronegativity difference, as in the case of III-V alloys. It may thus not apply to Si and Ge whose electronegativities hardly differ [13].

To contribute towards the clarification of this issue we studied here two $\text{Si}/\text{Si}_{0.7}\text{Ge}_{0.3}$ samples grown at different temperatures using solid source MBE. The growth temperatures were both in the window with the highest segregation length and the lowest luminescence intensity as reported by Miyao et al. [10-11].

1. Introduction

For optical as well as electrical devices, the layer and interface quality is an important parameter. For example, alloy inhomogeneities can serve as centres for carrier scattering, which assist indirect excitonic recombination without requiring a phonon. They may also contribute to the localisation of excitons. Carrier scattering at rough interfaces can drastically reduce the transport properties in two dimensional electron or hole gases. Thus, the effect of SiGe/Si interfacial potential fluctuations on the low-temperature photoluminescence spectrum of a multiple SiGe quantum well is studied. The dependence of the PL spectrum on laser excitation level is discussed in terms of localised excitonic transitions.

A moderate annealing of the as-grown wafer at temperatures around 200°C leads to D-line emission. The intensity of these lines strongly depends on the annealing temperature. The formation of misfit dislocations is discussed in terms of local micrometer strain fluctuation inside the SiGe layers.

-) One of the major disadvantages of Si/SiGe heterostructures for optical devices is the strong thermal quenching of the luminescence intensity. One possibility to increase the external quantum efficiency of such light emitting diodes is the use of a transparent, ohmic top contact. This is why in the second part a basic Si/SiGe light emitting diode is fabricated using for the first time the transparent and at the same time highly conductive ternary alloy Indium-Tin-Oxide (ITO). Thus, the absorption of the top contact can drastically be reduced leading to an enhancement of the diode electroluminescence efficiency. A high vacuum chamber with effusion cells was built up and preliminary tests on the deposition parameters with respect to a high optical transparency together with a high electrical conductivity were performed. The electroluminescence of the diode was determined as a function of temperature and injection current density. Finally a brief formalism to estimate the external power efficiency is presented.

1. Introduction

These aspects are treated in several chapters. After an introduction in Chapter 1, general properties of Si and SiGe heterostructures are described in chapter 2. Molecular beam epitaxy and rapid thermal chemical vapour deposition are briefly discussed, followed by structural and optical properties of low dimensional SiGe heterostructures.

In Chapter 3 the principles underlying the various analytical techniques used in this work to characterise the samples structurally, optically and electrically are presented. X-ray reflectivity and diffraction and photoluminescence are discussed in more detail, as both techniques were central to this work.

Chapter 4 describes the experimental set-up. As main parts of this work the set-up of an photoluminescence experiment as well as the construction of a high vacuum thermal evaporator in close co-operation with the company “MBE Komponenten” is discussed.

Chapter 5 deals with the experimental results and their discussion. Finally, conclusions are presented together with suggestions for further work.

2. Si and SiGe Heterostructures

The high quality epitaxial material grown at temperatures of around 500-600°C offered an early opportunity to incorporate SiGe into Si microelectronics in order to realise novel devices such as HBTs [8,14], resonant tunnelling diodes [15] and high mobility two-dimensional-hole gases [16]. In addition, SiGe recently became an attractive buffer material for the growth of strained Si layers for MOS applications due to enhanced carrier mobility for faster transistor with the present technology [17,18].

2.1. Epitaxial Growth of Si and SiGe Layers

The growth of very high epitaxial quality Si films and Si-based multilayer structures was mainly driven by the industrial demand for very large scale integration (VLSI) of electrical components and for novel device structures. A scientifically useful epitaxial technique shall fulfil the following aspects:

- a) low-temperature process
- b) films of excellent crystalline, electrical and optical quality
- c) precise thickness and doping profile control and
- d) the possibility to grow heterojunctions of different bandgap materials

There are various techniques to grow thin epitaxial heterostructures, such as molecular beam epitaxy (MBE), gas source MBE (GSMBE), chemical vapour deposition (CVD), low pressure CVD (LPCVD) or ultra high vacuum CVD (UHVCVD) [19-24]. Much of the development in the SiGe field has been driven by progress in the growth process. Several authors [21,22] have shown that epitaxially flat interfaces can be grown without seriously smearing the heterointerface.

2.1.1. Molecular Beam Epitaxy

Silicon molecular beam epitaxy (MBE) describes in general the growth of any Si-based single-crystalline layer on top of atomically clean Si wafers in an ultra-high vacuum environment ($P \approx 10^{-10}$ - 10^{-11} mbar) out of an atomic or molecular flux from evaporation sources. As the term atomic or molecular flux already indicates, the atoms or molecules reach the surface without performing any collisions with each other or restgas atoms. This latter aspect together with the special design of the evaporation cells ensures a rather ideal statistical distribution of the evaporated species. Relatively low growth rates of

2.1. Epitaxial Growth of Si and SiGe Layers

~0.3-10 Å/sec in combination with sufficiently high substrate temperatures ensure a very low defect and contamination level as well as a precise control of composition and doping profiles of the epitaxially grown films. One particular advantage of the MBE technique is the compatibility of the UHV growth environment with the use of modern surface analytical techniques, in-situ techniques such as reflection high energy electron diffraction (RHEED) or ex-situ techniques such as Auger electron spectroscopy (AES) or low energy electron diffraction (LEED). Thus, the growth morphology and surface crystallinity can be studied in detail from the very first sub-monolayers. Together with the flexibility of the technique concerning the growth of new material systems, MBE has become a very powerful tool in fundamental science.

The growth of Silicon-Germanium alloys by MBE was first started in the seventies [25]. In the earliest stage of work on SiGe/Si heterojunctions, the effort was mainly concentrated on superlattices under different strain conditions. Through the rapid development of Si-MBE, n-p-n HBTs with reasonable performance were demonstrated for the first time by several groups within a short period at the end of 1987 [26-29]. Since then, intensive studies have been carried out and the improvements are significant [8].

During the last 20 years Si-MBE has developed remarkably into a very versatile technique. Among others the most important development was the demonstration of a defect-free pseudomorphical growth of $\text{Si}_{1-x}\text{Ge}_x$ layers on Si substrates [25,30]. The lattice mismatch of ~4.17% between Si and pure Ge is accommodated by a built-in strain instead of forming misfit dislocations, if the Ge or $\text{Si}_{1-x}\text{Ge}_x$ layer thickness is smaller than the so called critical thickness and if the growth temperature is kept at a moderately low level.

2.1.2. Rapid Thermal Chemical Vapour Deposition

Originally the growth of strained $\text{Si}_{1-x}\text{Ge}_x$ epitaxial layers on a Si substrate was the domain of molecular beam epitaxy (MBE). It was believed that high quality material could not be grown by chemical vapour deposition (CVD) below approximately 800°C. Smith and Ghidini [31,32] investigated criteria for oxygen and moisture levels required to obtain an oxide-free silicon surface at a given temperature. These data have been extrapolated and used by Meyerson [19] to design a CVD reactor allowing the growth of high quality epitaxial Si films at temperatures of around 600°C. In order to maintain a clean, oxide-free Si surface, the partial pressure of moisture has to be below about 10^{-7} mbar at 800°C and below 10^{-9} mbar at 600°C. The requirements for oxygen are slightly less strict. The reactor

2.1. Epitaxial Growth of Si and SiGe Layers

is capable of reaching 10^{-9} mbar and the technique is called ultrahigh vacuum CVD (UHVCVD). This approach proved successful, as epitaxial Si and SiGe films have been grown at temperatures down to 500°C [20].

Sedgwick, on the other hand, reported selective Si-epitaxial growth at temperatures down to 600°C at atmospheric pressure [33] using SiH_2Cl_2 , in contrast to Meyerson who used SiH_4 . The reported moisture and oxygen levels, however, did not meet the Smith and Ghidini criteria and seemed too high to be compatible with good quality epi growth at high temperatures.

This gave rise to the thought that the growth of low-temperature SiGe SiGe films might be possible in a commercially available reactor, as it has been done in the meantime e.g. at Philips Research with an ASM reactor .

2.2. Properties of Si/SiGe Heterostructures

2.2.1. The Concept of Pseudomorphic Growth

Heterostructures of the five group IV elements C, Si, Ge, Sn and Pb are characterized by a large lattice mismatch due to the big difference in their constituent's covalent radii. This lattice mismatch leads to strain fields in the heterostructures, which in turn determines many characteristics such as the effective mass, the dielectric constant and the bandgap energy. The lattice mismatch restricts the realization of high quality heterostructures to thin Ge or Si_{1-x}Ge_x layers only.

Despite the large lattice mismatch of 4.17% between Si ($a_{\text{Si}}=5.430 \text{ \AA}$) and Ge ($a_{\text{Ge}}=5.658 \text{ \AA}$) the growth of Si/Si_{1-x}Ge_x heterostructures is possible with a very high epitaxial quality using MBE or CVD. As the epitaxial Si_{1-x}Ge_x layer is much thinner than the Si substrate, the in-plane lattice constant a_{\parallel} follows the one of Si ($a_{\parallel}=a_{\text{Si}}$). The lateral compression ε_{\parallel} of the Si_{1-x}Ge_x layer is determined by the difference of the lattice constant and is given by

$$\varepsilon_{\parallel} = \frac{a_{\parallel} - a_0}{a_0} = -0.0417 \cdot x,$$

with a_0 being the cubic lattice constant of Ge and the Ge concentration x as the only parameter. As long as the thickness of the Si_{1-x}Ge_x is smaller than the critical thickness (d_c) the lateral compression is compensated by an elongation ε_{\perp} of the Si_{1-x}Ge_x layer in the growth direction leading to a tetragonal distortion of the lattice. In this so-called pseudomorphical growth the Si_{1-x}Ge_x layer is strained (see Figure 2) and the distortion can be determined by elastic theory to [34]

$$\varepsilon_{\perp} = \xi \cdot \varepsilon_{\parallel}.$$

Using the elastic constants C_{ij} or the Poisson ratio ν the constant ξ can be determined to

$$\xi = -2 \frac{C_{12}}{C_{11}} = -2 \frac{\nu}{1-\nu}.$$

Most theories, together with experimental results, agree that the strain due to lattice mismatch can be accommodated elastically, if the layer is thinner than a certain critical thickness d_c [35,36].

d_c is inversely proportional to the misfit strain between two materials and is greatly increased with reduced growth temperature. At low growth temperatures (550°C and below) the epitaxial growth process is far from equilibrium and kinetically limited, resulting in a larger d_c (metastable regime) [37].

2.2. Properties of Si/SiGe Heterostructures

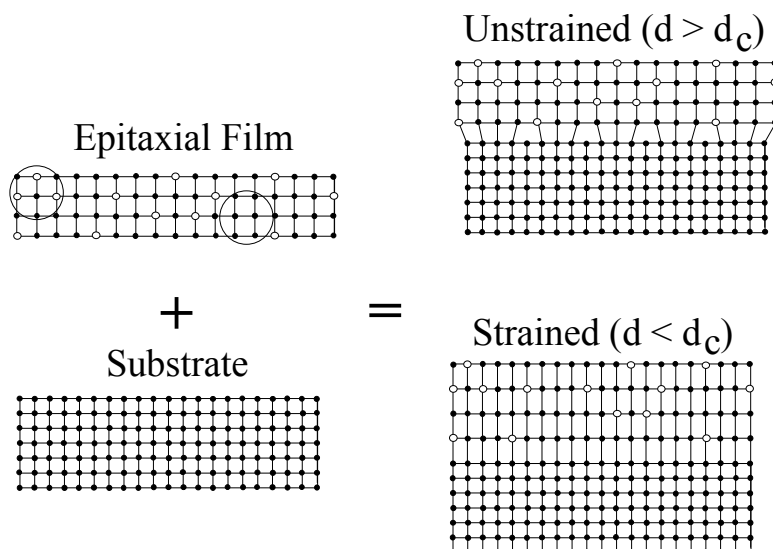


Figure 2: Schematics of the two different natural ways to accommodate lattice mismatch. Full circles denote Si atoms, open ones represent Ge atoms. The translational symmetry is broken due to compositional disorder (e.g. in the circled regions).

There is a cross-over from this elastic mismatch compensation to a plastic accommodation, if the layer thickness exceeds the critical thickness. In this case misfit dislocations are created at the interface or threading dislocations can pass through the whole layer leading to a relaxation of the stored elastic energy. The limits of the metastable regime are not really well defined, because of the dependence on details of the dislocation source configuration and differing sensitivity of dislocation measurements. The People-Bean fit [37] is a good estimate of growth at 550°C. At lattice misfits larger than 1% (Ge content > 25%) strain adjustment by relaxed buffer layers and nonplanar surface morphology are considered to be the main problems. Virtual substrates with a relaxed SiGe buffer on a Si-substrate may be considered as a new unit with a lattice constant different from Si. Thus, one can adjust the strain of the following layers. The drawback of the solutions so far are threading dislocations and/or larger buffer thicknesses of about micrometers as in the case of graded buffers (smooth increase of Ge content).

Figure 2 illustrates the two fundamental mismatch accommodation modes. Alternatively the strain relaxation can also lead to island formation during growth. Both relaxation mechanisms reduce the strain in the $\text{Si}_{1-x}\text{Ge}_x$ layer and an energetically favourable state is achieved. The in-plane $\text{Si}_{1-x}\text{Ge}_x$ lattice constant a_{\parallel} is determined by $a_{\text{Si}} < a_{\parallel} < a_0$. The occurrence of these two different strain relaxation processes is dependant on the strain energy, the surface energies and the energy for the formation of misfit dislocations. The kinetics of the system can also have a significant influence.

2.2. Properties of Si/SiGe Heterostructures

As a rule of thumb, for high Ge concentrations and high growth temperatures, island formation already occurs for relatively thin $\text{Si}_{1-x}\text{Ge}_x$ layers (≈ 10 nm). Misfit dislocations play an important role for low Ge concentrations and higher $\text{Si}_{1-x}\text{Ge}_x$ layer thicknesses (>10 nm). Additionally, misfit dislocations can also be observed in the case of very thick islands, if the strain cannot relax elastically.

A relatively low misfit dislocation density can lead to a strong modification of the luminescence properties of Si/Si $_{1-x}$ Ge $_x$ heterostructures. This aspect is of special interest with respect to light emitting diodes and other devices such as transistors.

The rapid development of Si/SiGe heterostructures, relying mainly on improved growth techniques such as MBE or chemical vapor deposition (CVD), enabled precise bandgap engineering in epitaxially grown wafers. This feature has been used efficiently in electronic applications to realize new high-speed devices.

2.2.2. Heteroepitaxial Growth Modes

Depending on the interface strains and surface energy in the case of thin films one can distinguish three different growth modes. The ideal layer growth, with the new layer only starting if the previous layer is completed, is called FM-growth (after Frank and Van der Merwe, see Figure 3 a) [38]. The step height in this two dimensional growth mode is at maximum one monolayer. FM-growth only occurs, if $\sigma_S > \sigma_F + \sigma_{SF}$, with σ_S , σ_F and σ_{SF} being the interface strain between substrate-vacuum, film-vacuum and substrate-film, respectively [39].

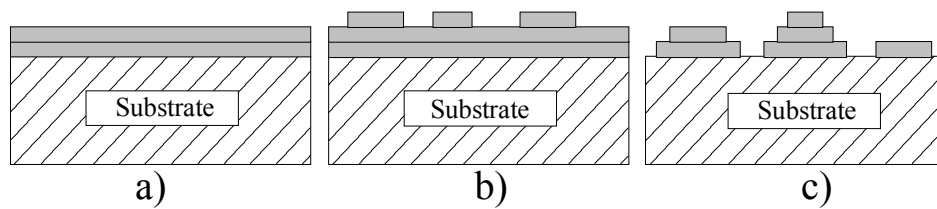


Figure 3: Fundamental growth modes depending on the interface strains: a) FM-growth, b) Stranski-Krastanov-growth and c) Volmer-Weber-growth .

Island growth (Figure 3 c) occurs if the relation between the interface strain is given by

$$\sigma_S < \sigma_F + \sigma_{SF} .$$

In this Volmer-Weber-growth mode (after Vollmer and Weber [40]) three dimensional islands are formed immediately from the first monolayer on. In the so called Stranski-Krastanov mode [41] layer growth proceeds as long as the cohesion forces of the film

2.2. Properties of Si/SiGe Heterostructures

dominate against the adhesion forces of the substrate, leading to the formation of islands. Thus, in certain material systems such as Ge or $\text{Si}_{1-x}\text{Ge}_x$ alloys with high Ge concentration grown on Si (or InAs grown on GaAs), one observes a mixture of both growth modes (see Figure 3 b). Figure 4 shows the different interface strains. An insufficient wetting of the substrate results due to large wetting angles Φ and the system is governed by VW-growth.

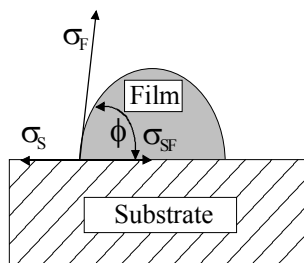


Figure 4: Wetting of a substrate by a thin film.

Growth mode transitions from two-dimensional to three-dimensional growth [42,43], optimum temperature windows [44] and effect of annealing steps [45] are well documented in the literature.

2.2.3. Band Structure

Silicon and Germanium crystallise in the diamond structure which consists of two face-centered cubic lattices (fcc) shifted by a quarter of the body diagonal ($\frac{1}{4}\frac{1}{4}\frac{1}{4}$) of the unit-cell. By contrast, GaAs crystallises in the zinc-blende structure and therefore it differs from Si since Ga and As atoms each occupy separate sublattices. This leads to a break of the inversion symmetry of the GaAs lattice, which is not the case in Si. The different electronic and optical properties of Si and GaAs can be derived from this structural difference, which is reflected in their respective band structure. The band structure is determined by the crystal structure, the bond type between the atoms, their bond lengths, the chemical species, the electronegativity, the stiffness and the elasticity. The band structure is the key to the dispersion relation of the charge carriers.

Conventionally, the band structure is represented by the dispersion relation $E_n(\mathbf{k})$, where E is the energy of an electron (or hole) at the band edge with a wave vector \mathbf{k} in the first Brillouin zone.

2.2. Properties of Si/SiGe Heterostructures

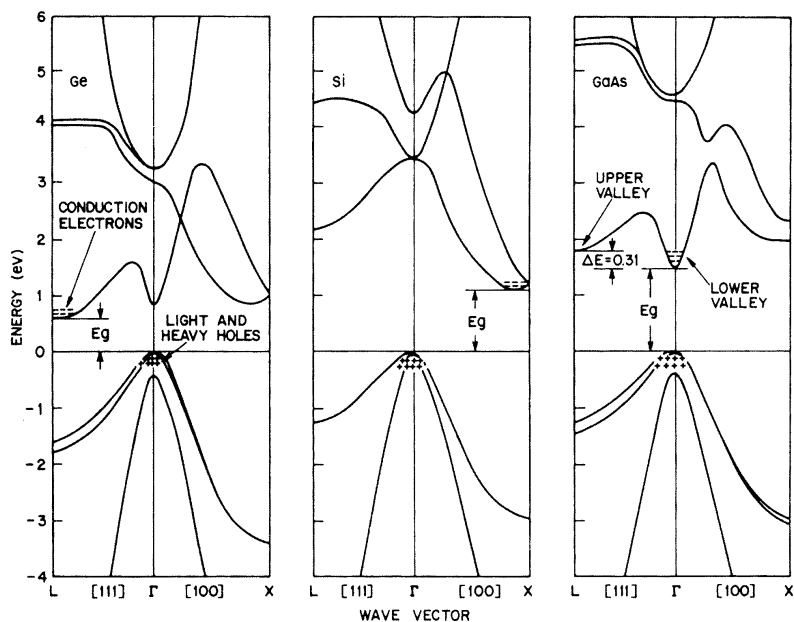


Figure 5: Energy dispersion relations of Ge (left), Si (middle) and GaAs (right) [46].

Figure 5 schematically shows energy dispersion relations for Si, Ge and as a comparison also for GaAs. Positive and negative energies refer to electrons and holes, respectively. Crystal symmetry requires that $E(\mathbf{k})$ have maxima at the zone center and the zone boundary. However, these are not the only points at which extrema can occur. In the case of the essentially covalent group IV elements and compounds additional extrema occur in the lowest laying conduction bands away from the zone center. Note that the valence band structure of most semiconductors is similar, exhibiting a maximum at the zone center $\mathbf{k}=0$ known as the Γ symmetry point. In the case of Si the maximum of the valence band is twofold degenerated. In accordance to the different band bending and the resulting effective masses the states of both bands are called heavy and light holes (hh and lh, respectively). Due to the spin-orbit interaction the degeneracy is partly broken shifting the so-called spin-orbit-holes (soh) by 0.04 eV in the case of Si and 0.30 eV in the case of Ge to lower energies.

Optical transitions are divided into direct and indirect ones, depending on whether conduction band minimum and valence band maximum occur at the same \vec{k} value. Figure 5 shows that the conduction band minimum of Si does not occur at $k = 0$ but at $k \approx 0.85X$ along the (001) direction (Δ -minimum). The Δ -minimum is six-fold degenerated. The conduction band of Ge is four-fold degenerated and lies along the (111) direction at the Brillouin zone edge (L-point).

2.2. Properties of Si/SiGe Heterostructures

In a direct bandgap semiconductor such as GaAs (see Figure 5, right) exciting an electron from the top of the valence band to the bottom of the conduction band, leaving a hole in the valence band, will lead to the emission of a photon after the recombination of these two carriers. The energy of this photon is the same energy as the band gap E_g . In the case of indirect semiconductors, e.g. Si or Ge, such direct recombination is not possible since the bulk selection rule $\Delta k = 0$ has to be fulfilled. The transition from the highest occupied level of the valence band to the lowest unoccupied level of the conduction band is forbidden unless one or several momentum conserving phonon participate (absorption or emission) are involved. As shown in Figure 6 electrons at the conduction band minimum need the assistance of a phonon to relax into the state filled with holes at the maximum of the valence band.

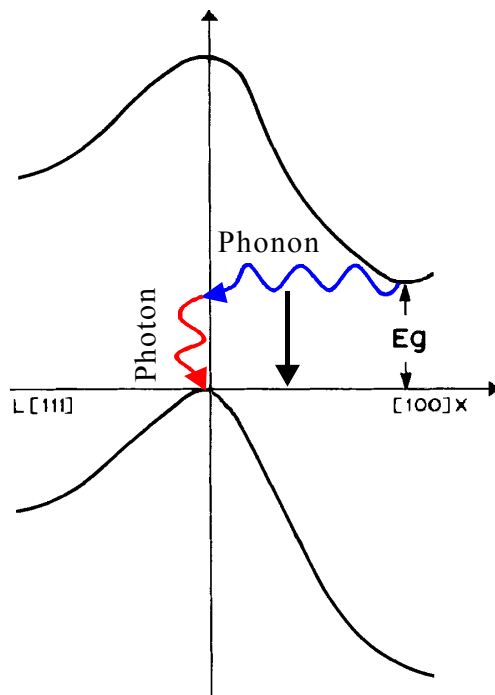


Figure 6: Schematic energy dispersion relation showing the assistance of a phonon in optical transitions in indirect semiconductors.

Such a three-body interaction is less likely than a two body interaction, thus the recombination rate in pure Si is much smaller compared to GaAs. Therefore the main drawback concerning Si as a light emitter is its extremely low efficiency of only 1 photon emitted per 10^7 generated electron-hole pairs.

The case of Ge is very interesting in that a higher order band actually has a slightly lower energy in the X, that is, $\langle 111 \rangle$ direction of the Brillouin zone. It is the nearest thing to a “direct semiconductor” that occurs naturally in the group IV systems.

2.2. Properties of Si/SiGe Heterostructures

A number of possibilities are available for the engineering of luminescence transitions in an otherwise indirect material. Luminescence is a result of significant overlap (in direct and reciprocal space) in the electron and hole wavefunctions. Whenever there is such overlap, luminescence is possible. However, the strength of the luminescence, that is, the emission rate, and therefore the quantum efficiency, depends on the extent of this overlap and the transition probability. Engineering solutions seek to increase this overlap and can be split into four classes:

- In impurity-mediated luminescence, an impurity that has an energy level in the gap of the semiconductor is used as an intermediate state through which the electron can recombine with the hole. The impurity level must be extended in \mathbf{k} -space to be efficient.
- Band structure engineering makes use of alloys. Two or more group IV elements are alloyed to shift the energy bands a little so that a direct transition is allowed.
- Quantum confinement can also increase the probability of a direct transition. One approach is the so called zone-folding, where an ultra-short-period superlattice with periodicity comparable with the lattice constant induces greater overlap of the conduction band states at the zone edge with the valence band states at the zone centre, increasing the possibility of a direct transition. The second approach is the strict quantum confinement in two, one or zero dimensions such as quantum wells, wires and dots.

In the case of pseudomorphic growth, strain induces further modifications on the band structure, including a further reduction of the band-gap and changes by splitting both the degenerate valence and conduction bands.

The degree of modifications are related to the strain in both the Si and the SiGe layers. Growing pseudomorphic SiGe layers on Si(100) substrates, the six-fold degeneracies of the Si conduction band minima are removed. The four valleys parallel to the growth plane shift downward, and the two valleys perpendicular to the growth plane shift upward. These variations will also influence the electron transport properties.

If a heterojunction of two semiconductors with different bandgaps (i.e. $\text{Si}_{1-x}\text{Ge}_x$ and Si) is formed, band-discontinuities (steps) occur at the interface. These band-discontinuities are the key features of heterostructures. Valence band discontinuities between strained $\text{Si}_{1-x}\text{Ge}_x$ and unstrained Si have been determined both theoretically [47-49] and experimentally [50-53], whereas all values agree well with each other within an uncertainty of about 10%.

2.2. Properties of Si/SiGe Heterostructures

An important feature of Si/SiGe quantum wells is the possibility to realise type-I and type-II band alignments by modifying the strain, i.e. confining the electrons and holes both in the SiGe layer (type-I) or confining the electrons in the Si barriers and the holes in the SiGe wells (type-II) .

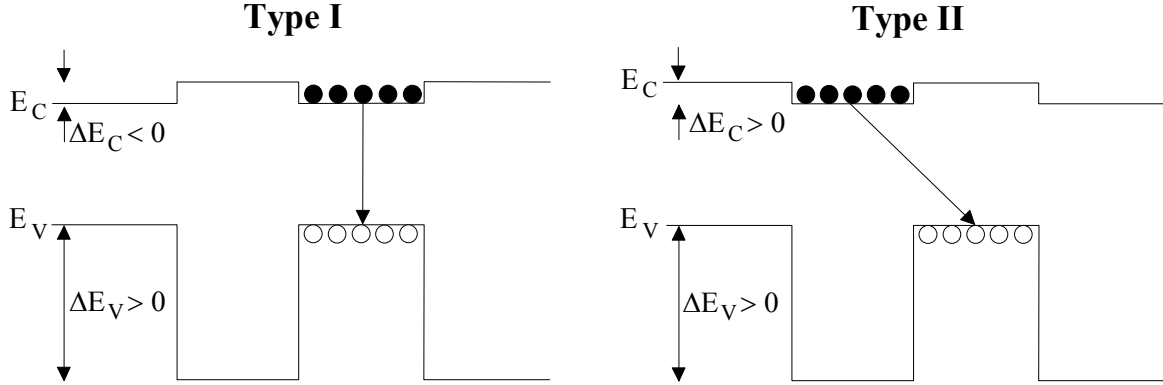


Figure 7: Type-I (left) and type-II (right) band alignment in Si/SiGe heterostructures.

In Si/SiGe the discontinuity in the conduction band is very small. However, there is a sign change if the Ge-concentration is bigger than about 0.65 [47], in other words, the band alignment changes from type-I to type-II at this composition. It is worthwhile mentioning that theoretical predictions suffer from a relatively high uncertainty in that the change from type-I to type-II can occur at very different Ge-concentrations or even the type-II is predicted to happen over the whole Ge-concentration range. Due to the small conduction band discontinuity, an experimental detection is not always possible. In principle the conduction band discontinuity can be determined from the bandgap difference and the valence band discontinuity using

$$\Delta E_C = E_g^{\text{SiGe}} - E_g^{\text{Si}} + \Delta E_V.$$

However, the theoretical value of the valence band discontinuity, as well as the experimental error, is of the order of this difference, so that a real prediction of the band alignment type is rather difficult. This problem has not yet been sufficiently clarified. The rather weak electron confinement can be significantly increased if a strained Si layer is grown on a relaxed or also tensile strained $\text{Si}_{1-x}\text{Ge}_x$ layer. Such heterostructures are of type-II.

$\text{Si}_{1-x}\text{Ge}_x$ alloys have a smaller fundamental bandgap than Si, and it decreases with increasing Ge content. For unstrained $\text{Si}_{1-x}\text{Ge}_x$ alloys with $x \leq 0.85$ the bandstructure is similar to that of Si with six-fold Δ -minima in the conduction band. At higher Ge concentrations the alloys become Ge-like with four-fold minima at the L-point.

2.2. Properties of Si/SiGe Heterostructures

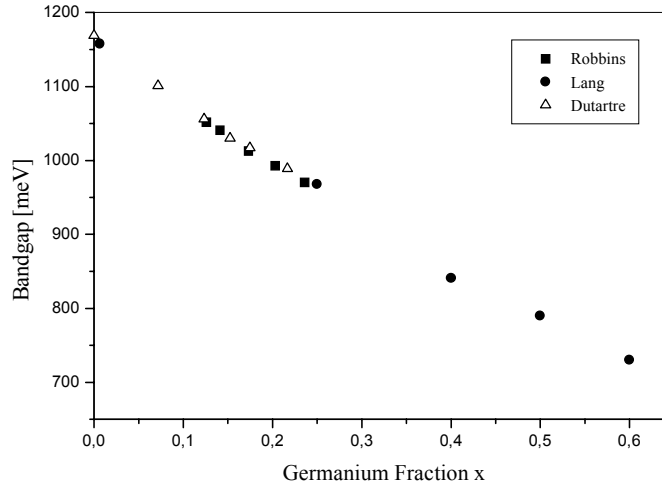


Figure 8: Energy of the SiGe no phonon line as a function of Ge concentration for 50 nm SiGe wells (squares) [54], for a 7.5 nm thick well corrected for the confinement shift (circles) [55] and for various well thicknesses (triangles) [56]

Figure 8 shows the decrease of the SiGe bandgap with the Ge concentration. The dotted line shows the bandgap of unstrained $\text{Si}_{1-x}\text{Ge}_x$ layers which can be described by [57]

$$E_{g,\Delta}^0(x) = 1.170 - 0.440 \cdot x + 0.206 \cdot x^2 \text{ for } \Delta\text{-minima with } 0 \leq x \leq 0.85 \text{ and by}$$

$$E_{g,L}^0(x) = 2.025 - 1.280 \cdot x \text{ for L-minima with } 0.85 \leq x \leq 1.$$

The symbols are experimental data of strained $\text{Si}_{1-x}\text{Ge}_x$ layer. The 4.2 K data of Robbins et al. (squares) [54] were recorded on a 50 nm quantum well grown by low pressure vapour phase epitaxy (LPVPE), where no confinement effects occur. Lang et al. (circles) [55] used a 7.5 nm quantum well grown by MBE and corrected their 90 K data for the confinement shift, determined to be 12 meV. Dutartre et al. (triangles) [56] measured 6 K PL spectra from RTCVD-grown SiGe quantum wells with a thicknesses varying between 25 and 100 nm depending on the Ge concentration.

Due to the thermal expansion of the lattice and due to the temperature dependent electron-phonon interaction the bandgap shows a temperature dependence that can be described after [58] by

2.2. Properties of Si/SiGe Heterostructures

$$E_g^0(T) = E_g^0(T=0) - \frac{\alpha \cdot T^2}{T + \beta},$$

where $E_g^0(T=0)$ as the bandgap at $T=0$ K,

$\alpha = 4.73 \cdot 10^{-4} \text{ eV} \cdot \text{K}^{-1}$ for Si and $\alpha = 4.77 \cdot 10^{-4} \text{ eV} \cdot \text{K}^{-1}$ for Ge and $\beta = 636\text{K}$ for Si and $\beta = 235\text{K}$ for Ge [59].

Assuming a linear dependence on the Ge concentration x one obtains

$\alpha = 4.740 \cdot 10^{-4} \text{ eV} \cdot \text{K}^{-1}$ and $\beta = 535.8\text{K}$ for $x=0.25$ and

$\alpha = 4.739 \cdot 10^{-4} \text{ eV} \cdot \text{K}^{-1}$ and $\beta = 543.8\text{K}$ for $x=0.23$.

2.2.4. Quantum Confinement

The wave description of quasi-particles in semiconductors allows us to associate a de Broglie wavelength, for example, to charge carriers and other excitations. Quantum confinement of charge carriers or phonons or excitons occurs when at least one of the lateral sizes of the volume where these waves are found is comparable to the de Broglie wavelength.

The physics of low dimensional semiconductors, i.e. quantum wells, wires and dots has been adequately treated by several authors [60,61]. A key aspect of semiconductor nanostructures is the modification of the energy levels, the density of states and, in optically active materials, a higher exciton binding energy as compared to the bulk case due to the confinement of charge carriers [60,62]. These modified intrinsic properties led to predictions of novel electrical and optical applications [60,63] some of which are already commercially available (e.g. quantum well lasers).

Since charge carriers behave like particles in a box, only discrete energy levels are allowed which, in turn, result in well-defined emission lines. Additionally, it has been shown that due to the high density of states in the case of quantum dots such lasers have a high optical gain, a very low threshold current J_{th} and are not temperature dependent. These emission lines allow the study of modified electronic levels. The overlap of the electron and hole wavefunctions plays an essential role in the radiative recombination efficiency.

Since confining these quasi-particles leads to an increased overlap of wavefunctions in real space and thus to a spreading out of their wave functions in momentum space, which increases the likelihood of strongly radiative transitions.

2.2. Properties of Si/SiGe Heterostructures

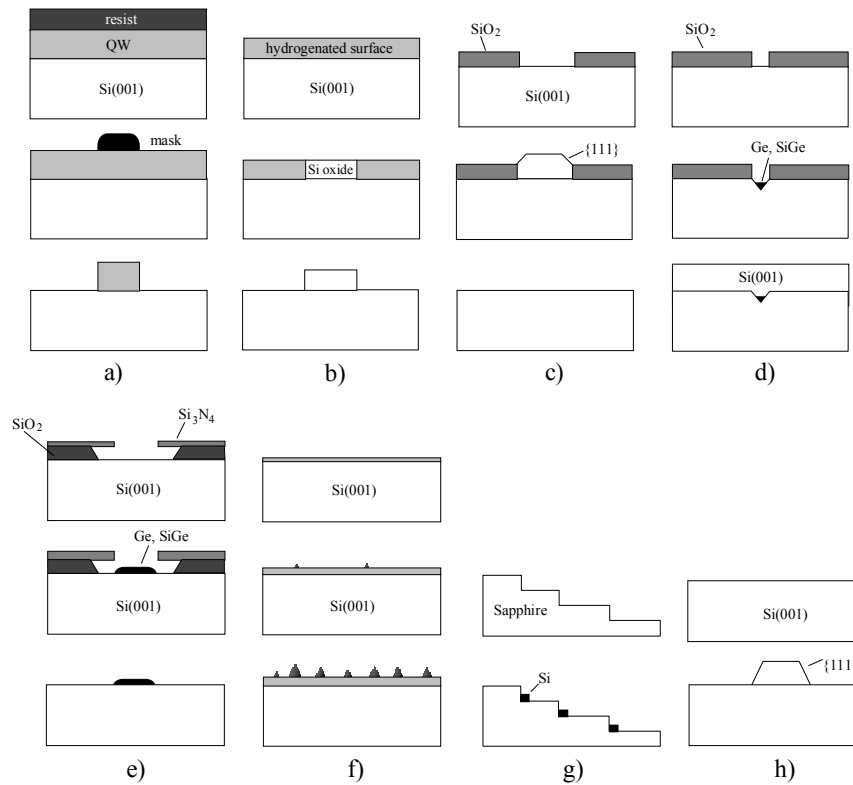


Figure 9: Sketch of different techniques to fabricate lateral nanostructures: (a) electron beam or other lithography and reactive ion etching, (b) scanning probe lithography by, for example, using a scanning tunneling microscope, (c) selective epitaxy, (d) growth in V-grooves, (e) growth through shadow masks, (f) self-organised growth, (g) growth on structured surfaces and (h) anisotropic wet etching.

There is also a concentration of the oscillator strength into the few optical transitions allowed in a quantum-confined electronic system. Furthermore, scattering at the wire or dot boundaries, a very likely event, can supply the needed momentum more readily in a confined structure. In addition, the recombination probability via nonradiative channels decreases simply due to the lower probability of the carriers reaching nonradiative recombination centres. However, since the presence of many particles leads to Auger non-radiative recombination processes, an ideal quantum dot would have only one carrier per dot. In practice, for luminescence spectroscopy low excitation power densities are used to excite the emission and, in structures driven by current injection, lower current densities are used to create few electrons and holes per dot in order to keep Auger processes at bay. Various experimental techniques have been successfully used to reduce the lateral extension of a layered structure to fabricate one-dimensional (1D) or quasi zero-dimensional (0D) systems. In general, these techniques can be separated into: (a) ex-situ methods, where the lateral dimensions are further restricted after the growth process, and (b) in-situ methods, where the lateral size reduction is achieved during the growth process.

2.2. Properties of Si/SiGe Heterostructures

An example of ex-situ techniques would be a combination of electron-beam writing of the features, followed by reactive ion etching (RIE) for mask transfer into the substrate [64]. Another is the selective epitaxial growth in small enough oxide windows patterned after growing part of the structure [62]. In-situ techniques comprise the local epitaxy with MBE using shadow masks [65,66], the use of film relaxation through island formation and growth on non-planar substrates (V-grooves) [67-69].

2.2.4.1. Quantum Wells (2D)

The 4.17% lattice mismatch between Si and Ge leads to strain fields in their heterostructures, which in turn determines characteristics such as the effective mass of carriers, the dielectric constant and the bandgap, among others. A detailed review on the Si/SiGe system is published by Jain [70] and Kasper [71]. As in other semiconductors, the in-plane stress is compensated by a tetragonal distortion of the lattice. There is a cross-over regime from this elastic mismatch compensation to a plastic accommodation, if the layer thickness exceeds a critical thickness. In this case misfit dislocations are created at the interface or threading dislocations can pass through the whole layer leading to a relaxation of the stored elastic energy.

The rapid development of Si/SiGe heterostructures, relying mainly on improved growth techniques such as MBE or CVD, enabled precise bandgap engineering in epitaxially grown wafers. This feature has been used effectively in electronic applications to realise new high-speed devices such as modulation-doped field effect transistors (MODFETs) or heterojunction bipolar transistors (HBTs). Top values for f_{\max} reported by Daimler Benz [8] are well in the range of 160 GHz and are comparable to state-of-the-art GaAs-based transistors.

Systematic shifts of the PL peaks to higher energies due to quantum confinement in strained SiGe/Si quantum wells have been reported independently in [72-74]. In [22,74,75] the Si barrier widths were chosen in order to avoid wavefunction spreading, to keep the quantum well nature and to maintain the strain of the SiGe well layers. Based on theoretical calculations [47] it was shown that a reduction of the barrier layer down to about 20 Å resulted in a shift of the PL energy [21,74].

2.2. Properties of Si/SiGe Heterostructures

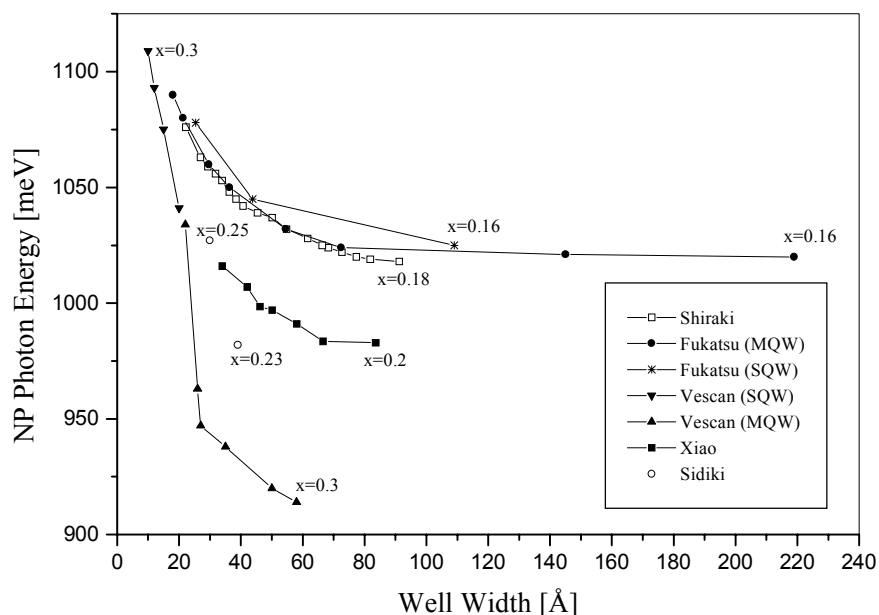


Figure 10: Energy of the SiGe NP emission line against the well width for a $\text{Si}_{0.82}\text{Ge}_{0.18}$ quantum well (open squares [21]), for a $\text{Si}_{0.84}\text{Ge}_{0.16}$ SQW and MQWs (stars and circles [74]), for a $\text{Si}_{0.80}\text{Ge}_{0.2}$ SQW and MQW (up and down triangles [72]), for a $\text{Si}_{0.80}\text{Ge}_{0.2}$ SQW (full square [73]) and for $\text{Si}_{0.75}\text{Ge}_{0.25}$ and $\text{Si}_{0.77}\text{Ge}_{0.23}$ MQWs (open circles [22,75]).

The data of [21,74] were recorded at 18 K and 19K, respectively, whereas those of [22,75] were taken at 5 K. Xiao et al. [73] performed PL experiments on RTCVD-grown $\text{Si}_{0.8}\text{Ge}_{0.2}$ single quantum wells (SQWs) at 5 K. Vescan et al. [72] used $\text{Si}_{0.7}\text{Ge}_{0.3}$ single quantum wells (SQW) and multiple quantum wells (MQW) grown by LPCVD for their optical and structural characterisation and recorded PL data at 4.2 K. In Figure 10 it can be seen that the emission energy increases with decreasing well width. In accordance with 2D confinement, the transition energies could be reproduced rather well using a standard square potential model [74], indicating, that very flat interfaces without significant interdiffusion could be grown. Significant interdiffusion would lead to a transformation of the initial square potential into a gaussian one of reduced height, thus the peaks associated with electronic energy levels would shift to higher energies.

2.2.4.2. Quantum Wires (1D)

Reducing the thickness of pure Ge wells to less than 1 monolayer (ML) can lead to the formation of self-assembled Ge wires. The energy of the SiGe emission monotonously increases with decreasing Ge thickness in a similar manner as in QWs. From plane view TEM studies these wires were found to grow at Si steps present on the (001) surface

2.2. Properties of Si/SiGe Heterostructures

oriented in the $\langle 0\bar{1}1 \rangle$ direction. In these structures, and in contrast to quantum wells, the power dependent PL does not show band-filling effects in the form of a blue shift of the emission lines. The absence of such a shift has been attributed to the higher density of states of the wire electronic levels [76].

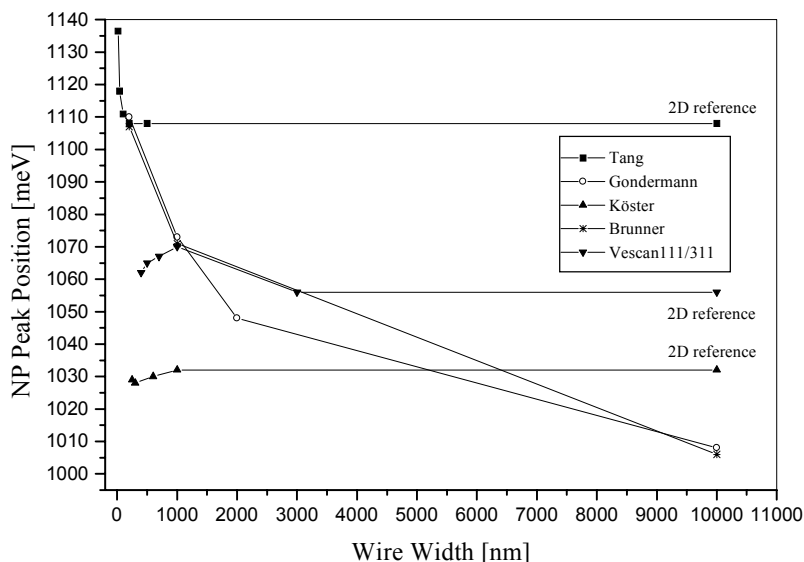


Figure 11: Energy of the SiGe^{NP} peak as a function of the geometrical lateral wire width. Squares: RIE etched Si_{0.8}Ge_{0.2} SQW [77]. Circles: locally grown 5.8 nm thick Si_{0.775}Ge_{0.225} SQWs [78]. Stars: 6 nm thick Si_{0.75}Ge_{0.25} SQWs [79]. Up-triangles: 5 nm thick Si_{0.75}Ge_{0.25} RIE etched SQW [80] and down-triangles: 1.7 nm selectively-grown Si_{0.7}Ge_{0.3} MQWs [81].

Figure 11 shows the SiGe^{NP} transition shift to higher energies with decreasing wire width for wires grown locally through micro-shadow masks (circles) [78]; (stars) [79], through oxide windows (down triangles) [81] and for wires fabricated using electron-beam lithography and reactive ion etching (squares) [82] (up triangles) [80]. Köster et al. [80] observed PL from deep etched SQW wires down to a lateral dimension of 250 nm, without a detectable SiGe peak energy shift. However, protecting the wire sidewalls with a plasma enhanced chemical vapour deposition (PECVD) oxide layer resulted in detectable luminescence from their 250nm wide wires.

Previously, Tang et al. [83] fabricated a series of 2.5 μm long and 10 to 500 nm wide wires in a modulation doped p⁺-Si/Si_{0.5}Ge_{0.5} SQW structure also by electron beam lithography and reactive ion etching. With decreasing wire width a strong shift to higher energies of the SiGe peaks occurs for wires smaller than about 100 nm. There are two contributions to this shift in the PL of structures with reduced lateral size, namely the modified strain and quantum confinement.

2.2. Properties of Si/SiGe Heterostructures

Additional techniques such as photoreflectance (PR) or x-ray diffraction are needed to distinguish between the two components. Generally, the smaller the nanostructure, the higher the strain relaxation in strained layer heterostructures.

2.2.4.3. Quantum Dots (0D)

Beside the fabrication of quantum dots by lithographic processes and growth on patterned substrates, in-situ self-organised growth of islands has attracted much interest. The main advantage of self-organisation is the simplicity of the process coupled to the possibility to grow defect-free structures with dot sizes well below 100 nm. However, the drawbacks of the technique are the large size distribution and the dot-to-dot distance fluctuations compared to dots fabricated by lithographic means, though recent results on stacking several dot layers show very promising ordering effects in terms of dot size and distribution homogeneity.

In the case of pure Ge wells, 2D layer-by-layer growth is observed up to about 4 monolayers (MLs). When the well thickness exceeds 4 MLs a new broad emission peak appears in the low energy region of the PL spectrum, together with no-phonon (NP) and transverse optical (TO) assisted phonon SiGe edge emission lines. From TEM experiments this broad emission could be attributed to the formation of Ge islands. The dot related luminescence has been found to be stable up to room temperature [76].

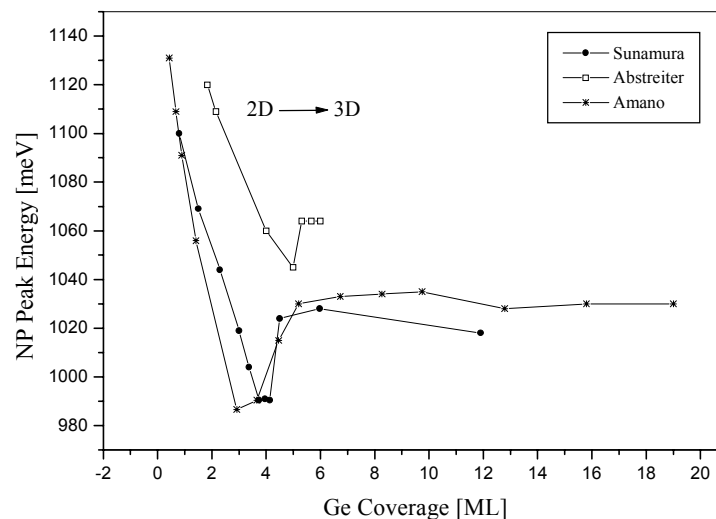


Figure 12: Ge-related NP PL emission energy of the 2D quantum wells against Ge coverage, indicating a 2D to 3D transition at around 3.7 ML (full circles [84], open squares [85] and crosses [86]).

2.2. Properties of Si/SiGe Heterostructures

Figure 12 shows the Ge NP photoluminescence energy with varying Ge coverage, showing the 2D to 3D transition at approximately 3.7 MLs [84]. It has been shown by TEM microscopy that for Ge concentrations higher than 40% in the SiGe wells islands form at the Si/SiGe interfaces [42]. MBE grown heterostructures show similar results to the GSMBE island formation. There is a red-shift of the PL signal with increasing thickness at low Ge coverage indicating the decreasing quantum confinement in the two dimensional wetting layer. In both cases the onset of the following blue-shift can be attributed to the formation of three dimensional islands combined with a lateral diffusion of Ge towards these islands leading to a strong confinement [43,84,85]. It was shown that the critical thickness for the onset of island formation is a function of Ge content, increasing with decreasing Ge content [85]. The lower temperatures used in GSMBE growth might lead to Ge-richer islands with a lower critical thickness. At lower temperatures lateral island diameters are also expected to be smaller due to a more limited surface diffusion leading to the energetic difference between the two different growth techniques previously mentioned.

Non-destructive x-ray diffraction is widely used to map the two-dimensional reciprocal space to characterise ordering, crystallinity or layer sequence in superlattices. However, the relative low diffraction intensity from an array of quantum dots or wires is usually too weak and therefore the use of synchrotron radiation is in most cases necessary.

Whereas reciprocal space mapping (RSM) of two dimensional superlattices shows satellites due to the periodicity of the superlattice in the q_z -direction, quantum dot arrays exhibit additional satellites in the $q_{||}$ direction, which originate from the periodicity of the dots within the array. Ni et al. [87] found a reduction of the mean lattice mismatch of reactive ion etched dots to the substrate in the growth direction from 0.0113 for a fully strained 30 period Si(3 nm)/Si_{0.7}Ge_{0.3}(3 nm) 2D-superlattice to 0.0070 due to strain relaxation after structuring the sample into 50 nm dots with a height of 300 nm and a pitch size of 130 nm. Such a lattice relaxation was only detected within dot structures compared to an area of 0.1x1 mm² of a Si/SiGe reference area. From two-dimensional RSM around an asymmetric reflection the authors also determined a mean in-plane lattice mismatch of 0.0059 with respect to the substrate.

A partial strain relaxation leads to the difference between these two values. The clear observation of the superlattice higher-order satellites within the dots indicates that the superlattice layers are still well ordered after the partial strain relaxation. However, the existence of some weak diffuse scattering in-between the superlattice reflections, suggests

2.2. Properties of Si/SiGe Heterostructures

the presence of an amorphous material layer surrounding the crystalline dots. This may be the result of crystal damage due to reactive ion etching or from redeposited SiGe alloy surrounding the dots.

Using bulk elastic theory for a homogeneous deformation the authors found a partial relaxation in the SiGe layers, whereas the Si layers are biaxially expanded. This strain symmetrisation makes the band offsets at the heterointerfaces to become type-II. The strain induces a splitting of the six-fold degenerated conduction band. Edge electrons in a $\Delta(2)$ band located near $k_{\parallel} \approx 0$ can recombine with holes located at $k_{\parallel} \approx 0$ across the interface without involving a phonon for the required momentum conservation. This is one possible explanation for the reported enhanced luminescence intensity of Si/SiGe quantum dots.

A comparable strain relaxation in similar dots fabricated in a 10 period $\text{Si}_{0.65}\text{Ge}_{0.35}$ consisting of 23 nm Si and 4 nm SiGe layers was obtained by x-ray diffraction. For dots with a diameter of 100 nm a strain relaxation of about 50 % was reported, increasing to around 85 % for dots with a diameter of 30 nm [88].

2.2.5. Thermal Relaxation

The pseudomorphic SiGe alloys are metastable, and the strain may relax at high temperatures. This fact can restrict the procedures for post-growth device processing. Various authors have reported an enhanced thermal stability of SiGe layers with a Si cladding layer relative to the equivalent strained films with a free surface [89-91]. Some results suggest that safe thermal processing is possible at 850 °C for 1 hour for Ge composition up to 20%, without detrimental effects on the Ge profile and the strain in the SiGe film [91]. This is apparently not a severe restriction for device processing.

Concerning the thermal stability of strained heterostructures under device processing and thermal cycles treatment, it has been observed and theoretically demonstrated that strained structures containing a capped layer, such as $\text{Si}_{1-x}\text{Ge}_x$ grown on Si substrate with a Si top layer as well, can have higher stability to thermal strain relaxation in comparison to uncapped heterostructures [92-94].

In the capped structure the alloy is placed between two interfaces and the relaxation process can produce misfit dislocation segments at both interfaces (the so-called double-kink mechanism) or only at the substrate-epilayer interface (single-kink mechanism) [92]. Essentially the double-kink introduces an additional term in the self-energy associated to the misfit dislocation.

2.2. Properties of Si/SiGe Heterostructures

This leads to a larger value of the restoring line tension in the force balance or excess stress formalism, suggesting a larger value of the critical thickness (and thus higher stability of the capped structure in comparison to a corresponding uncapped structure. The mechanism is certainly more complex than this simple description. Some experimental results have shown a dramatic increase in the stability of capped structures, while others indicated only a discrete difference [92,93]. One essential difference between the diverse measurements is perhaps related to the fact that a dramatic increase in the alloy stability is only expected for the cases where the cap layer is much thicker than the underlying alloy. Nevertheless, these results open a promising perspective, due to the fact that many high-quality heterostructure-based devices have a layer structure where a thin, highly strained alloy layer (for instance the base in a heterobipolar transistor) is buried under thicker Si caps. Still from the formal point of view, Tsao and Dodson presented suitable modifications to their kinetic relaxation models accounting for the case of buried heterostructures under the double- and single-kink mechanisms, by introducing an equivalent average of the varying strain over the layer depth [95].

2.2.6. Formation of Misfit Dislocation

Misfit dislocations are created, if the energy gain through the strain relaxation (dependent on the layer thickness) is bigger than the required energy for the formation of such dislocations (constant value) [34,36]. Misfit dislocations form an irregular network of lines parallel to the [110] crystalline directions. Whereas only few misfit dislocations are found within the $\text{Si}_{1-x}\text{Ge}_x$ layer, additionally many dislocations form deep inside the Si substrate (several μm) [96]. Although a theoretical model of Matthews and Blakeslee [97] predicts somewhat higher values of the critical thickness, the results are still much smaller than those determined experimentally. Furthermore, an increase of the critical thickness with reduced growth temperature was found experimentally [24]. The observed discrepancy can be related to the point that the theoretical models are built for thermodynamical equilibrium, whereas all experimental growth techniques, excluding liquid phase epitaxy, are far away from thermodynamical equilibrium.

3. Principles of Analytical Techniques

In this chapter the underlying principles of various analytical techniques will be introduced. Some emphasis is put on x-ray diffraction and reflectivity as well as on the photoluminescence as the core experiments.

3.1. Secondary Ion Mass Spectroscopy

Secondary ion mass spectroscopy (SIMS) is a very powerful technique due to its high sensitivity to low atomic concentrations even down to the ppb (parts per billion) range [98]. The RTCVD samples were chemically characterised by SIMS to allow a comparison of the layer thicknesses to those obtained from x-ray reflectivity.

When an energetic beam of primary ions accelerated by a high voltage (500 to 5000 eV) strikes the surface of interest, a small fraction of the sputtered particles will be charged forming secondary ions. These secondary ions are then analysed with a quadrupole mass spectrometer and can be displayed as a function of time or equivalently converted as a function of depth below the surface. The SIMS technique can provide information on dopant chemical concentration and depth distribution through the thin films layers of extremely small impurity concentrations in Si, e.g., 10^{15} cm^{-3} (0.2 ppm) for In and 10^{10} cm^{-3} (0.02 ppm) for Sb, respectively. Since sputtered atoms are primarily removed from the outermost atomic layers of the surface, SIMS can provide a fairly good depth resolution. However, in practice, since the impinging beam mixes atoms in the lattice below the film surface by recoil collisions, the obtained value for the depth resolution is much bigger than a few atomic layers. The use of a low-energy of the primary ion beam can considerably improve the obtained depth resolution, since the penetration depth of the ions increases with the ion energy. However, at the same time, it also lowers the yields of analysed secondary ions. Depth resolution in the 2 to 5 nm range can be achieved routinely.

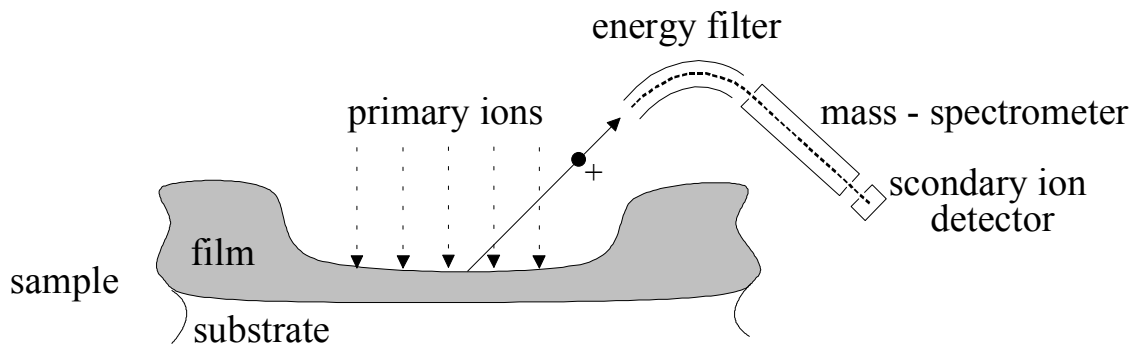


Figure 13: Schematics of the operating principle of secondary ion mass spectroscopy.

3.1 Secondary Ion Mass Spectroscopy

Both oxygen and cesium ion beams are used for SIMS measurements. The former is more effective for electropositive elements such as B, Al and Cr, and the latter for electronegative elements such as C, O and As.

The mass spectrometer resolves ions with a certain mass to charge ratio, m/e . In the depth profiling mode, the equipment is set to trace one or more values of m/e as a function of the sputtering time. By comparing the intensity signal obtained for a certain element with the intensity from a reference sample with pre-determined atomic concentration of this element, it is possible to obtain the atomic concentration versus the depth in the sample.

Errors in the absolute determination of atomic concentration are typically 10%. The dependence of the depth of the structure and the sputtering time is obtained via the sputtering rate, which is approximately proportional to the primary ion current for the same crystal matrix.

3.2. Photoluminescence Spectroscopy

In general many different ways can be followed to stimulate the luminescence of semiconductors. However, in all cases one obtains a non equilibrium state of electrons and holes created in the conduction or valence band, respectively. The adjacent recombination of electrons and holes may lead to the emission of a photon, which is described as a so-called radiative recombination. However, there also exist many non-radiative recombination mechanisms. Before discussing these undesired processes the radiative recombination shall be discussed first.

A very simple and powerful measurement technique is photoluminescence spectroscopy (PL). Here, carriers are excited by a pump beam with a photon energy higher than the bandgap of the structure. The carriers will thermalise to the bottom of the bands and recombine emitting light with the bandgap energy (see Figure 14). However, this means that not much information can be acquired about the optical properties for higher photon energies. For most device applications, however, the region closest to the bandgap is most important. At room temperature, the luminescence of silicon and silicon based semiconductors is rather weak. The reason for this is that most of the recombination of electron-hole pairs occurs non-radiatively. The dominant process is Shockley-Hall-Read recombination [99] where traps and impurities are involved. The quality of an epitaxial layer can be tested very easily by measuring the intensity of the spectrally integrated photoluminescence, as this is inversely proportional to the density of traps. To obtain more information, the emission is resolved spectrally.

3.2 Photoluminescence Spectroscopy

As the signal is very weak at room temperature, a laser is used as the excitation source together with a high sensitivity detector, such as a photomultiplier tube or an avalanche photodiode.

The previously high energetic electrons thermalise quickly via electron-phonon scattering to the band edges where they recombine with the holes. In the case of photoluminescence one can generally assume the detection of already thermalised electrons as the thermalisation process of most semiconductors is much faster (10 ps-100 fs) than the recombination process.

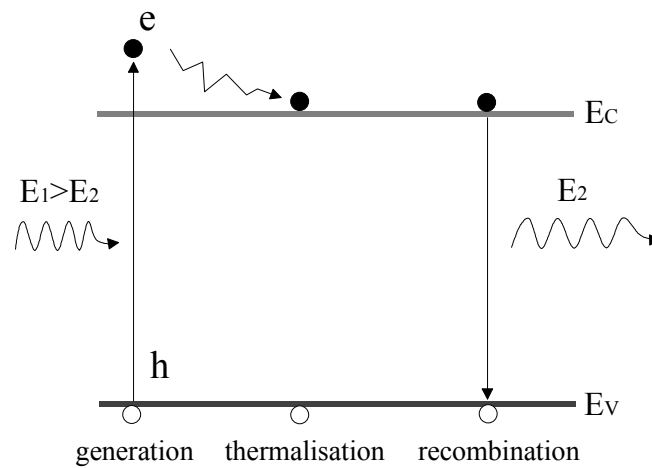


Figure 14: Schematic illustration of band-edge recombination.

Figure 14 schematically shows the process of carrier photo-creation, thermalisation and recombination. The spectrum of the emitted photons yields information about the bandgap. In principle, also other parameters, such as carrier temperature, can be extracted from the photoluminescence spectrum. Carrier transport and electric field effects can also be studied by photoluminescence. The idea is to have a quantum well to trap the carriers that are photogenerated over the structure. The more effective the transport and capture in the quantum well, the higher the luminescence signal. By varying the wavelength of the excitation source, one can vary the depth of the excitation and, hence, the transport distance. One can selectively generate carriers in the parts of the structure with lowest bandgap by using a suitable excitation wavelength, exciting resonantly a particular quantum well.

PL spectroscopy, as a very simple and fast technique, is mainly used for material characterisation in a broad variety of fields. The use of the as grown samples without any further treatment such as electrical contacting is its main advantage in contrast to electroluminescence spectroscopy.

3.2. Photoluminescence Spectroscopy

As a possible correlation between the structural and optical quality of Si/SiGe multiple quantum wells was one of the main issues of this work PL spectroscopy will be in the focus of this work.

As discussed in section 2.2 $\text{Si}_{1-x}\text{Ge}_x$ is an indirect semiconductor. Thus, the recombination of an electron-hole pair requires the emission (or absorption) of a phonon to fulfil the momentum conservation rule. In this respect the momentum k_{photon} of a photon can be neglected, as it is about three orders of magnitude smaller than the momentum difference Δk of electrons and holes

$$\frac{k_{\text{photon}}}{\Delta k} = \frac{E_G / \hbar \cdot c}{0.85 \cdot \pi / a} \approx 10^{-3}.$$

Phonon Assisted Transitions

The emission (or absorption) of a phonon offers one way to conserve the momentum during the recombination process of electrons and holes. Other possibilities such as scattering will be discussed later. Due to the rather low temperatures during the experiments ($T \leq 300$ K) one can neglect any phonon-absorption effects as the phonon energies are much higher ($k_B T = 25$ meV at room temperature in contrast to 58 meV for the TO phonon of Si). Ignoring excitonic effects, the energy of the emitted photon is reduced by the amount of the energy of the involved phonon, shifting the emission lines to lower energies. The energy transfer occurs as the emission or absorption of a phonon is an elastic scattering process, involving a partial energy transfer to the phonons, in contrast to inelastic transitions, which will be discussed in the case of no-phonon transition.

The probability of such a four body-effect (electron-hole-phonon-photon) is about 5-6 orders of magnitude less than a three-body effect in the case of a direct semiconductor [100]. Due to the simultaneous coupling to the electromagnetic field and to lattice vibrations the transition probability is calculated by using time dependent second-order perturbation theory (the first order matrix elements $|M|$ are zero) [101,102]. A set of selection rules is obtained which indicate that, in the case of Si, the participation of a longitudinal acoustical phonon (LA) is forbidden whereas that of a transversal optical (TO) phonon is the highest.

Transitions without Phonon Involvement (NP-Line)

In the case of interband transitions the k-conservation rule results from the exact periodicity of the crystal lattice. However, the Ge atoms in the $\text{Si}_{1-x}\text{Ge}_x$ alloy are statistically distributed, leading to some degree of disorder, which also effects the electronic properties due to the different potentials of the Si and Ge atoms. Thus, the k-conservation rule must not always be fulfilled and there is a non-zero probability, that transitions without a phonon involvement can occur. These are called no-phonon transitions (NP). In this case the required momentum is conserved through scattering of the carriers at the alloy fluctuation potentials inside the $\text{Si}_{1-x}\text{Ge}_x$ layer. Such a scattering process can also occur at impurities or dislocations. Despite excitonic effects, which will be discussed in the next section, the energy of the emitted photons corresponds to the band gap. As the momentum is transferred to the whole lattice there is no energy transfer. The probability of such an elastic scattering process is described by time independent second-order perturbation theory and it grows with the degree of the perturbation. Both transitions being second-order processes therefore also have comparable intensities.

Weber and Alonso [57] showed for unstrained, bulk $\text{Si}_{1-x}\text{Ge}_x$ alloys that the probability of the NP relative to the TO phonon assisted transition is proportional to $x(1-x)$, emphasising the origin due to alloy fluctuations. Other authors have proved the same dependence for strained $\text{Si}_{1-x}\text{Ge}_x$ layers with a concentration $0 \leq x \leq 0.25$ [54,56,103].

3.2.1. Exciton Recombination

To characterise the material properties without thermal broadening or quenching aspects, photoluminescence spectroscopy is mostly performed at cryogenic temperature. In this case one also observes a binding state of the electron-hole pair due to Coulomb attraction. These *excitons* can be well described in the atomic hydrogen model. As in the case of electron-hole pairs free or bound excitons can exist. Due to the relatively low excitonic binding energy of only a few meV (11 meV for Si) they are ionised by increasing the sample temperature or the carrier density resulting again in electron-hole pairs.

Excitons are electron-hole pairs that are bound to each other and may, in addition, be either free (FE) or bound to donors or acceptors (BE) or they can even be localised at microscopic alloy fluctuations within the SiGe layer (LE) or, as will be shown later in this work, at interfacial potential fluctuations (see Figure 15). When excitons decay radiatively, light is emitted.

3.2. Photoluminescence Spectroscopy

Excitonic luminescence is a good indicator of material quality, but unfortunately, in general, excitons have too short lifetimes at room temperature to be significant. However, work by a few groups [104] has shown that the confinement of the excitons in a quantum well can be used to tune the emission wavelength as well as to increase the excitonic lifetime.

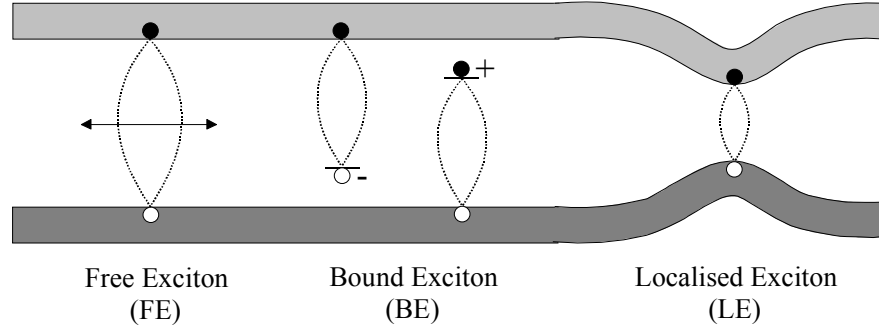


Figure 15: Schematic drawing of free, bound and localised excitons within a crystal lattice. The binding energy is pointed to by dotted lines in between the electrons and holes.

As the wavefunction of an exciton is extended over several lattice parameters, one can describe free excitons in analogy to the hydrogen atom. Such excitons are called Wannier-Mott excitons. In this model one assumes holes to be more spatially localised than electrons due to their much larger effective mass. The binding energy and the radius for the ground state are given by

$$E_{FE} = \frac{R_H}{\epsilon_r^2} \frac{m_{red}}{m_0}$$

$$a_{FE} = \epsilon_r \cdot \frac{m_0}{m_{red}} \cdot a_0$$

with

$$a_0 = \frac{4 \cdot \pi \cdot \epsilon_0 \cdot \hbar^2}{m_0 \cdot e^2} \approx 0.529 \text{ \AA} ,$$

$$\frac{1}{m_{red}} = \frac{1}{m_{e,eff}} + \frac{1}{m_{h,eff}} ,$$

$R_H = 13.6 \text{ eV}$ is the Rydberg constant ,

$a_0 = 0.529 \text{ \AA}$ = the radius of the hydrogen atom,

m_0 = the mass of the free electron,

$m_{e,eff}$ = the effective mass of the electron,

$m_{h,eff}$ = the effective mass of the hole and

ϵ_r = the dielectric constant of the semiconductor.

3.2. Photoluminescence Spectroscopy

Due to the very small confinement of electrons in the barrier layers it is assumed that most of the electron wavefunction leaks into the SiGe well layers. The degeneracy of the conduction band minima is lifted by uniaxial strain, resulting in a genuine heavy mass in the direction of compression ($m_l=0.92 m_0$) and a genuine light in-plane mass ($m_t=0.19 m_0$ perpendicular to the compression in the (100) direction [105]. There is no experimental data on the strain dependence of bulk electron masses available. Theoretical calculations from Rieger and Vogl [106] show only slight changes of the mass parameters due to strain and Ge content.

For the effective mass of holes, in contrast to the unstrained case, the mass of the heavy holes parallel to the layer is smaller than the one of the light hole (lh). It is also smaller than in the case of unstrained Si ($0.29m_0$). The effective masses for electrons and hole are shown in Figure 16.

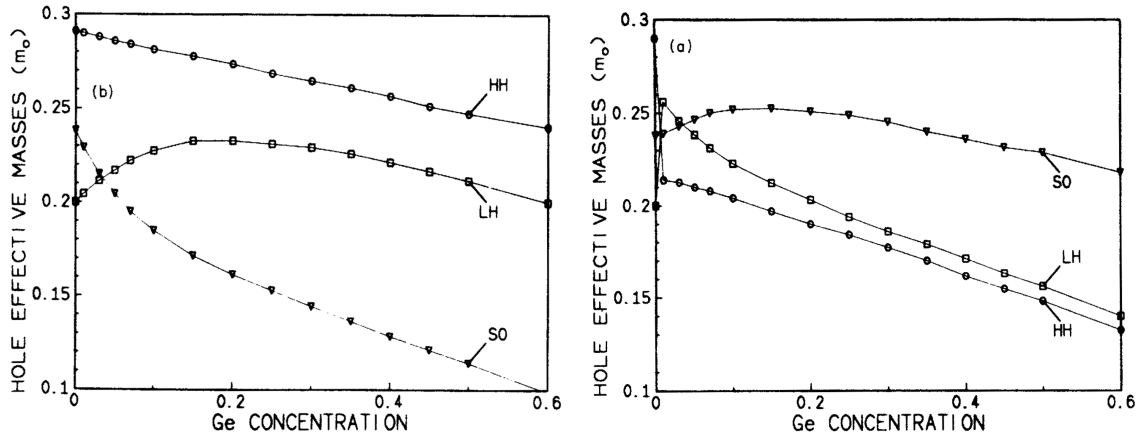


Figure 16: Calculated effective hole mass at the Γ point for strained $\text{Si}_{1-x}\text{Ge}_x$ as a function of x vertical (left) and parallel to the layer (right) [107].

Thus for strained $\text{Si}_{1-x}\text{Ge}_x$ layers on Si substrates the valence band is determined by the heavy hole (hh) band. For a Ge concentration of $x=0.23$ one obtains $m_{hh,eff} (hh) \cong 0.19 m_0$.

With $\frac{1}{m_{red}} = \frac{1}{m_{e,eff}} + \frac{1}{m_{hh,eff}} \cong \frac{1}{0.19} + \frac{1}{0.19} = 0.095 \frac{1}{m_0}$ and $\epsilon_r = 13.16$ one obtains a radius

of 73\AA for the free exciton in a strained SiGe. The value of 73\AA is in very good agreement with a previously reported free exciton Bohr radius of 40\AA in unstrained $\text{Si}_{1-x}\text{Ge}_x$ alloys with $x < 0.85$ [57].

3.2. Photoluminescence Spectroscopy

ϵ_r was calculated after Humlíček [108] taking into account a linear interpolation of the dielectric constant of $\text{Si}_{1-x}\text{Ge}_x$ alloys with various Ge concentrations. Additionally also the dependence of ϵ_r on the wavelength was taken to be linear in the range of 1.2 - 1.3 μm .

It must be noted that the use of the effective mass theory (H-atom approximation) is only valid, if $a_{\text{FE}} \gg$ unit cell diameter (compare to 2.2.1) for the ground state. In contrast to such Wannier-Mott excitons one also distinguishes Frenkel excitons, which are small in real space ($\sim 1 \text{ \AA}$) and tightly bound. Such excitons can no longer be treated in the simple effective mass approximation. However, in the case of e.g. Si, Ge or GaAs the Wannier-Mott approximation is very well suited.

Bound Excitons (BE)

Bound excitons (BE) are excitons that are bound to acceptors or donors. As discussed above a free exciton can be described in analogy to the H-atom. If an exciton is bound to a shallow donor or acceptor, the system can be described as an H_2 -atom. For Si and typical doping elements P, B, As, Al the Sb binding energies are about 1-6 meV. In the PL spectra of Si one typically observes a peak shifted by this amount. The binding energy is characteristic for different atoms, enabling the identification of the binding centers within the semiconductor. Figure 17 shows PL spectra of a RTCVD grown Si/SiGe multiple quantum well (MQW) sample, later referred to as n-i-p⁺ RTCVD sample, recorded at different laser excitation power densities. At low excitation power density only transverse optical phonon assisted bound excitonic recombination ($\text{Si}^{\text{TO}}_{\text{BE}}$) is observed. With increasing power density this peak first increases in intensity then saturates after all shallow acceptors are occupied and no further excitons can be bound. Additionally, at higher power densities one observes two further peaks, originating from transverse optical free excitons and from the electron-hole-droplet recombination, which will be discussed in section 3.2.2. In contrast to the bound exciton the free excitonic emission does not show saturation at these power levels. The energetic difference of about 5.2 meV between the bound and the free exciton corresponds well to the binding energy of the exciton to the shallow acceptor Sb., which is known to be present in our Si(100) substrates to about 10^{15} cm^{-3} . Due to the rather small binding energies of excitons they are not stable at elevated temperatures near room temperature. At present excitonic luminescence has the role of a diagnostic tool rather than being used for luminescent applications.

3.2. Photoluminescence Spectroscopy

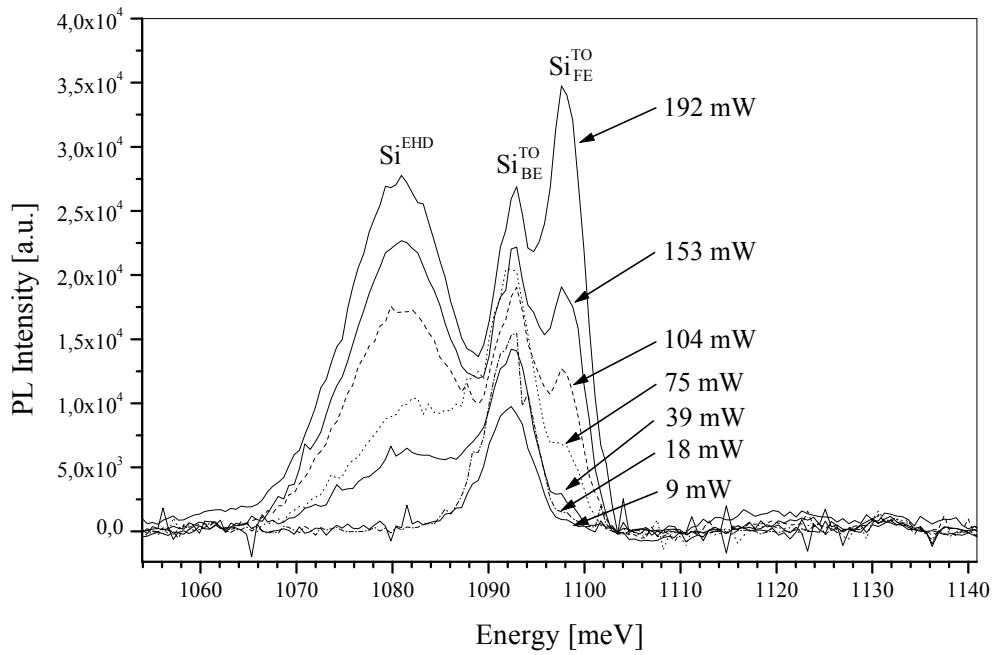


Figure 17: PL spectra of the n-i-p⁺ RTCVD sample recorded at various laser power densities showing the transition from a bound to a free exciton.

3.2.2. The Electron Hole Droplet Emission

At high laser excitation power density in Si and Ge one can observe the electron hole droplet (EHD) emission. As illustrated in Figure 18 the EHD is formed by a coexisting sea of photogenerated electrons and holes under high optical pumping. The combined potential and kinetic energies form a resulting dip as a function of carrier density and hence the EHD appears.

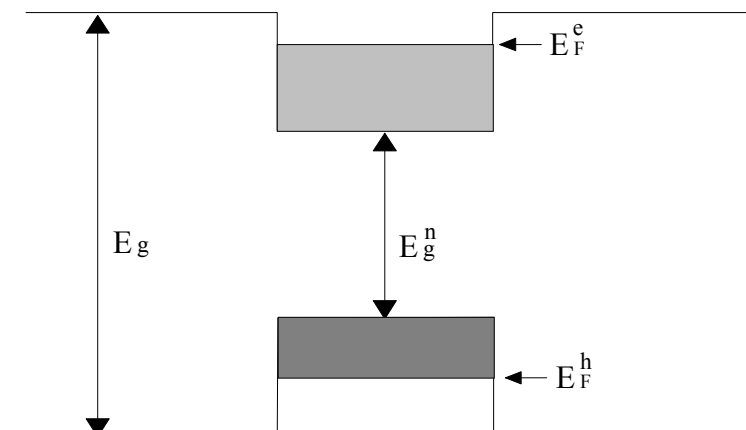


Figure 18: Self-induced potential sink in the bandstructure after formation of an EHD at low temperatures.

3.2. Photoluminescence Spectroscopy

The reason for this effect is a stronger renormalisation of the bandgap through the locally enhanced carrier density. Hereby, impurities are believed to act as nucleation centers [109]. The total energy will be negative if the energy reduction through the renormalisation process is greater than the energy increase by filling up the bands. Because both energy parts are given by different proportionalities one even obtains a minimum of the total energy serving as a potential sink for carriers.

In the case of a local fluctuation in the carrier density n , e.g. near the presence of a dopant, a potential is formed, trapping also other carriers. Thus, the density at this place is further increased resulting in a deeper potential sink.

The process of locally forming an EHD stops if the energetic minimum is reached. This is $n_e = n_h = 3.3 \cdot 10^{18} \text{ cm}^{-3}$ in the case of Si at 5 K [109,110]. For Ge a value of $2.4 \cdot 10^{17} \text{ cm}^{-3}$ was obtained at 1.08 K [111]. In both cases the experimental values correspond very good to the theoretical ones. The smaller value in the case of Ge is due to the smaller effective density of states, leading to a higher kinetic energy. Further capturing of carriers will thus not increase the density of the EHD but only its size. As the electron hole plasma in these droplets behave like a liquid, the EHD is also referred to as an electron hole liquid (EHL). Due to its constant carrier density the line shape and width of EHD luminescence does not change with increasing the excitation density. Only the intensity is increasing with the laser power.

The relative probabilities of the different phonon assisted transitions can be directly observed in the photoluminescence intensity (see high energy side of Figure 19 with a very intense TO emission of the Si substrate in comparison to the weak TA line). In the case of $\text{Si}_{1-x}\text{Ge}_x$ alloys there are various local phonon modes due to the presence of oscillations between Si-Si, SiGe and Ge-Ge atoms. In a systematic PL study of bulk $\text{Si}_{1-x}\text{Ge}_x$ crystals (unstrained) Weber and Alonso [57] have determined the energy and the relative emission probability of these modes in the recombination process. The results are shown in Table 1.

3.2. Photoluminescence Spectroscopy

	TO _{Si-Si}	TO _{Si-Ge}	TO _{Ge-Ge}	TA
$h \cdot \nu$ [meV] _{theo} [57]	58.0	49.0	34.5	18-7.5x
$h \cdot \nu$ [meV] _{RTCVD sample}	57	51	35	17
$h \cdot \nu$ [meV] _{MBE samples}	56	/	/	16
Probability	1-x ²	x(1-x)	x ²	≈0.1

Table 1: Energy and relative emission probability of different phonons in Si_{1-x}Ge_x after [57]. For comparison also experimental values determined in this work are shown for Si_{0.77}Ge_{0.23} (RTCVD sample) and Si_{0.75}Ge_{0.25} (MBE) MQWs. The relative transition probability, depending on the Ge concentration x, and is proportional to the PL intensity of the respective peak.

For Si_{1-x}Ge_x alloys with x ≤ 0.3 the probability of the TO_{Si-Si} phonon is the highest. However, the other modes are also detectable as weak peaks as shown in Figure 19. For a better resolution of the distinct modes one has to perform the PL measurement at very low temperatures such a 1-2 K.

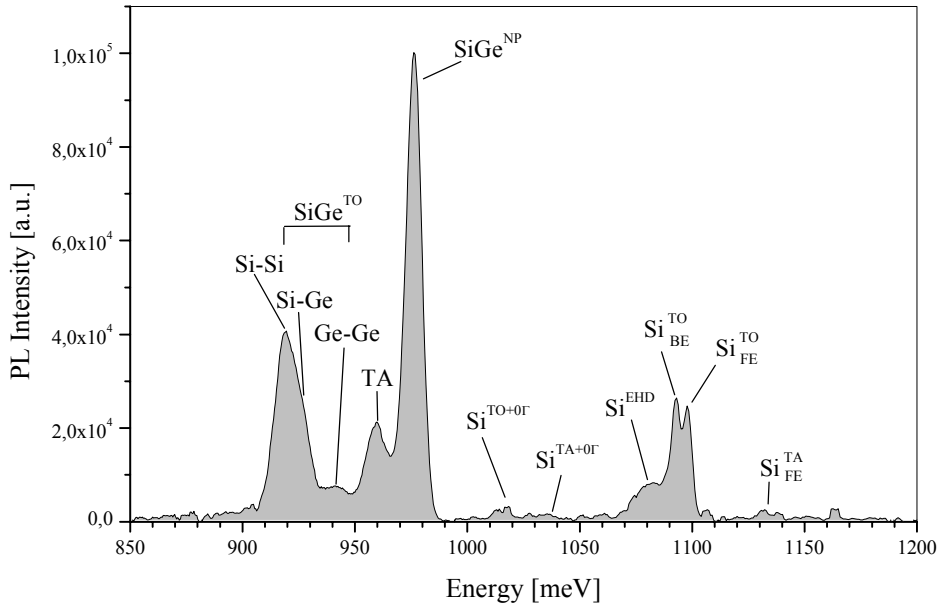


Figure 19: Low temperature PL spectrum of a Si/SiGe MQW structure recorded at 7K and an excitation power density of 320 mW/cm².

The PL spectrum of an MBE grown 15 period Si/Si_{0.77}Ge_{0.23} multiple quantum well (MQW) structure recorded at 7 K and an excitation power density of 320 mW/cm² is shown in Figure 19. The assignment of the detected lines has been well established in the literature [57]. The luminescence lines labeled SiGe^{NP} and SiGe^{TO} correspond to the SiGe no-phonon and the transverse optical phonon-assisted emission. The main contribution to

3.2. Photoluminescence Spectroscopy

the SiGe^{TO} emission results from the Si-Si vibration within the SiGe alloy. Si-Ge and Ge-Ge lines are only visible as a small shoulder or as a little bump, respectively. The peak at around 960 meV is due to Si-Ge transverse acoustical phonon-assisted emission (Si-Ge^{TA}). On the high energy side, the Si transverse acoustic phonon assisted free exciton emission line ($\text{Si}^{\text{TA}}_{\text{FE}}$) is observed. The strong emission at 1098 meV is due to the transverse optical phonon assisted free exciton recombination ($\text{Si}^{\text{TO}}_{\text{FE}}$). Bound Si transverse phonon assisted excitonic emission is also observed with an exciton binding energy of 5.4 meV referring to shallow acceptors (Sb).

At 1080 meV Si electron-hole droplet emission (Si^{EHD}) is visible. In between the Si EHD and the SiGe^{NP} lines Si two-TO and two-TA phonon emission is observed. These peaks are due to radiative recombination processes with the involvement of two phonons, one TO (or TA) and a second TO (or TA) of the Brillouin-Zone center with $k=0$. The very weak intensity is well explained due to the presence of a five-body process, which is even less probable than a four-body transition [101]. The integrated intensity of the SiGe related emission is higher than that of the Si (substrate plus cap) and with the proper confinement even remains up to room-temperature.

The influence of a biaxial strain on the phonon energies of $\text{Si}_{1-x}\text{Ge}_x$ alloys can be characterised theoretically as well as experimentally (PL, Raman Spectroscopy). It turns out that for alloys with $x \leq 0.3$ the change in the phonon energies is only very small (≈ 1 meV). Thus it shall no longer be of interest in this work [112].

3.2.3. T-Band Luminescence

Several authors reported a broad, intense luminescence band in thick, partly relaxed $\text{Si}_{1-x}\text{Ge}_x$ layers with a concentration of about 0.03-0.21 [103,113,114]. The maximum of this so-called T-band emission is about 100 meV below the excitonic bandgap of strained $\text{Si}_{1-x}\text{Ge}_x$, i.e. the exact position of the T-band depends on the Ge concentration. The rather large FWHM of the T-band (~ 30 -140 meV) increases linearly for small x with the Ge concentration. Houghton et al. [113] correlated the FWHM with inhomogeneities in the alloy concentration leading to Si or Ge clusters within the $\text{Si}_{1-x}\text{Ge}_x$ layer. Hartmann et al. [115] developed a lineshape model taking only statistical alloy fluctuations into account and could very well describe the peak shape of the T-band emission. Obviously, T-band excitons are formed through strong binding of a hole to a neutral center related to alloy

3.3. Electroluminescence Spectroscopy

fluctuations, which in turn weakly binds an electron. However, despite great efforts the exact nature of the isoelectronic T-band centres is still not understood in detail.

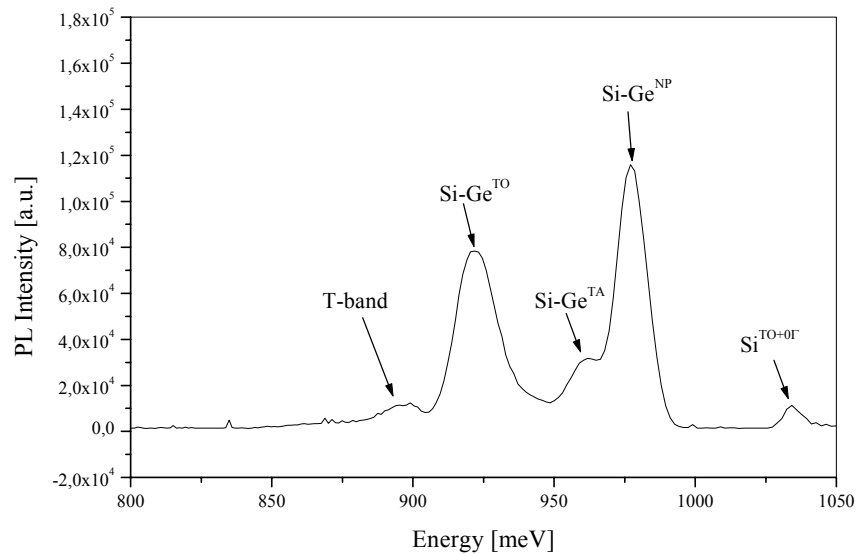


Figure 20: PL intensity of an as grown Si/SiGe MQW structure 6 months after the growth.

Interestingly high quantum efficiencies of the T-emission of about 31% [114] remained of any real technological relevance due to the fast thermal quenching at temperatures around 77 K. Several reasons for this high quantum efficiency were given. A localisation of the carriers at these potential fluctuations reduce the probability to reach non-radiative defect centers. Additionally, this localisation, similar to carriers in quantum dots, increase the wavefunction overlap in k-space, enabling nearly direct recombination.

3.3. Electroluminescence Spectroscopy

In the case of electroluminescence the carrier creation is achieved by current injection through the sample. For semiconductors mainly p-n, p-i-n junctions or Schottky contacts are used enabling a current injection into the active region. Light emitting diodes or lasers are the main application field of electroluminescence. Carriers injected electrically into an p-i-n diode preferably recombine in the intrinsic multiple quantum well region of the diode. Therefore both the PL and EL originate from the multiple quantum well and consequently appear at the same energy (see 5.4.7). Beside the pure characterisation of the samples also a Si/SiGe n^+i-p^+ diode was fabricated and tested in this work.

3.4. Raman Spectroscopy

3.4. Raman Spectroscopy

The usefulness of this technique to characterise semiconductor-crystals and –structures is well known [116,117]. With only minimal sample preparation, Raman spectroscopy is used to study films $<2000\text{\AA}$ with a lateral spatial resolution of $\approx 1\mu\text{m}$ if using micro Raman in multilayer systems [118]. In Raman spectroscopy a photon is scattered inelastically in a crystal. Incident (scattered) photons have energy $\hbar\omega_L$ ($\hbar\omega_S$), polarisation \hat{e}_L (\hat{e}_S) and wavevector \mathbf{k}_L (\mathbf{k}_S). In first order process one or several elementary excitations are created (Stokes-process) or annihilated (Antistokes-process). The conservation rules for a first order Raman process are given by

$$\omega_L - \omega_S = \pm\omega_J$$

$$\mathbf{k}_L - \mathbf{k}_S = \pm\mathbf{k}_J,$$

with $\hbar\omega_J$ and \mathbf{k}_J the energy and wavevector of the elementary excitations, here limited to a phonon, the +(-) signs refer to the stokes- (antistokes-) process. The absolute value of the phonon wavevector is given by

$$k_J = \sqrt{\mathbf{k}_L^2 + \mathbf{k}_S^2 - 2\mathbf{k}_L\mathbf{k}_S \cos\theta}$$

with θ being the angle between \mathbf{k}_L and \mathbf{k}_S . The smallest (largest) angle of \mathbf{k}_J is experimentally realised by $\theta \approx 0$ (180°) in forward (backscattering) direction. As the examined SiGe samples absorb strongly in the investigated spectral range, the Raman experiments were performed in the backscattering geometry, as shown in Figure 21.

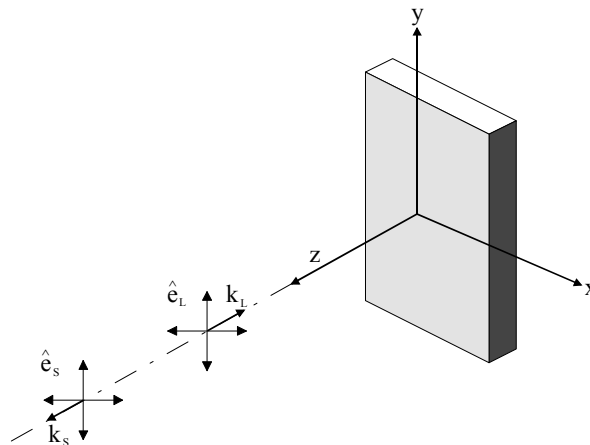


Figure 21: Schematic view of the backscattering geometry with $\theta \approx 180^\circ$.

A typical spectrum of $\text{Si}_{1-x}\text{Ge}_x$ multiple quantum wells are shown in Figure 22. The spectrum is characterised by four dominant peaks centered at 299 and 408, 432 and 520

3.4. Raman Spectroscopy

cm^{-1} . The prominent peak at 520 cm^{-1} is due to optical phonons of the Si substrate. The two lines at 299 and 408 cm^{-1} correspond to scattering from optical phonons involving Ge-Ge and Si-Ge stretching motions, respectively. The origin of these lines is well known and their frequencies were calculated in dependence of the Ge concentration within the “isodisplacement” model. The energies and relative intensities of the $\text{Si}_{1-x}\text{Ge}_x$ lines depend on the strain [119] and on the concentration x [120].

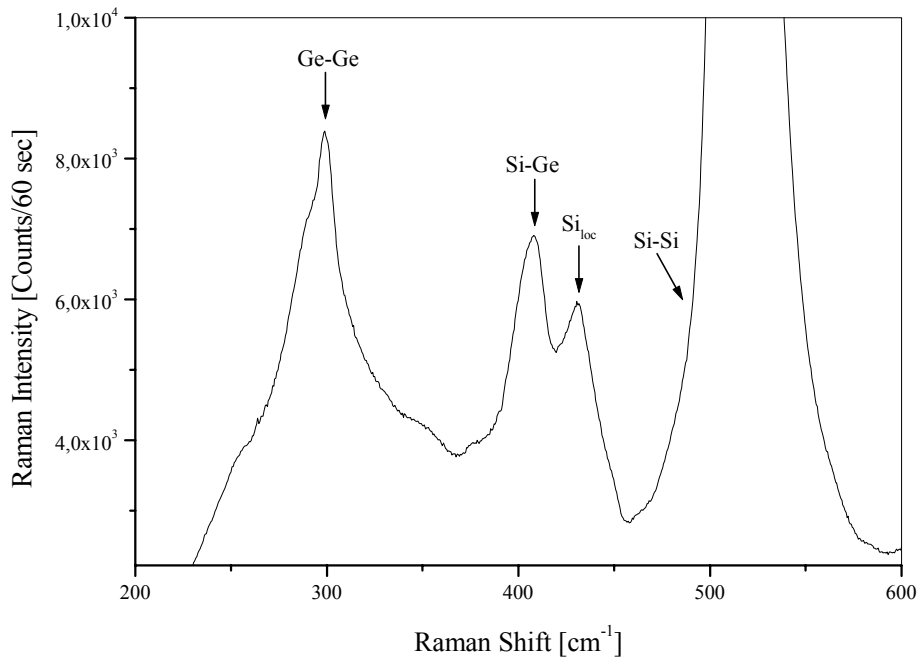


Figure 22: Raman spectrum of a $\text{Si}/\text{Si}_{0.77}\text{Ge}_{0.23}$ MQW structure recorded at room temperature and an excitation wavelength $\lambda=514.5\text{nm}$.

In these experiments due to the high penetration depth of the laser beam the Si-Si mode is only resolvable as a shoulder beside the substrate line. The additional feature at 432 cm^{-1} can be attributed to vibrations of Si atoms in specific local coordinations [121]. These vibrations occur through statistically adding Ge atoms to an initially pure Si crystal. The symmetry will thus be distorted locally corresponding to a localisation of the vibrations of the Si atoms in the neighbourhood of Ge atoms. Mainly because the much heavier Ge atoms hardly vibrate, this mode has a lower frequency than the major Si-Si mode.

The relative intensities of the Ge-Ge, Si-Ge and Si-Si modes strongly depends on the Ge-concentration x_{Ge} [120,121]. They can be linked to the number of the respective bonds in the SiGe alloy and can thus be used to determine the alloy composition [122].

3.5. X-ray Techniques

3.5.1. Refraction law for x-rays

In general a monochromatic electromagnetic wave propagating through a medium experiences a refraction index n given by [123,124]

$$n^2 = 1 + \frac{Ne^2}{\epsilon_0 m} \sum_j \frac{f_j}{\omega_j^2 - \omega^2 - i\omega\gamma_j}$$

with

N = number of atoms per unitvolume

$e = 1,602 \cdot 10^{-16}$ C

$m = 9.11 \cdot 10^{-31}$ kg

$\epsilon_0 = 8,85 \cdot 10^{-12}$ F/m

$\omega = k/c$

f_j = oscillator strength

ω_j = electronic resonance frequency

γ_j = phenomenological damping factor

The energy of x-rays with a wavelength $\lambda \approx 1\text{\AA}$ is approximately $hc/\lambda \approx 10$ keV and is thus, despite some stimulation of the inner shells, much higher than all electronic resonances $h\omega_j/2\pi$ of the medium. The average refraction index for x-rays with $\omega \gg \omega_j$ is given by

$$n=1 - \delta - i\beta$$

with

$$\delta = \lambda^2 \frac{Nr_e Z}{2\pi}$$

$$\beta = \frac{\lambda\mu}{4\pi}$$

and

r_e = classical electron radius ($\frac{e^2}{4\pi\epsilon_0 mc^2} = 2.814 \cdot 10^{-5}$ Å)

Z = nucleus charge number

μ = linear absorption coefficient.

3.5. X-ray Techniques

It is important to note that the real part of the refractive index n is always smaller than 1. The transition from vacuum to any medium is thus always a transition to an optically thinner medium. There is therefore always an angle α_c below which the x-rays are total reflected (external total reflection).

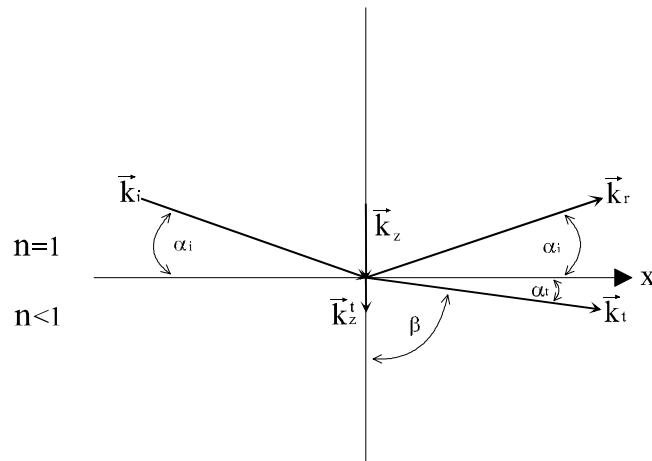


Figure 23: Diffraction geometry under grazing incidence: k_i , k_s and k_t are the wavevectors of the incident, the reflected and the transmitted wave.

The critical angle of total reflection can be derived from the Snell's refraction law:

$$n_1 \cos \alpha_1 = n_2 \cos \alpha_2$$

$$\cos \alpha_c = n$$

as $n_1 = 1$ and $n_2 = R_e(n)$.

As α_c is very small, the cosine term can be developed to

$$\cos \alpha_c \approx 1 - \frac{1}{2} \alpha_c^2 \approx 1 - \delta$$

with the critical angle

$$\alpha_c \cong \sqrt{2\delta} = \lambda \sqrt{\frac{Nr_e Z}{\pi}}$$

3.5. X-ray Techniques

3.5.2. Reflected and transmitted x-ray wavefields

In a dielectric medium with the dielectric constant ε the propagation of a monochromatic electric field $\vec{E}(\vec{r}, t) = \vec{E}(\vec{r}) \cdot e^{-i\omega \cdot t}$ is determined by the Maxwell equation

$$\nabla_x \nabla_x \vec{E}(\vec{r}) + k^2 \varepsilon(\vec{r}) \vec{E}(\vec{r}) = 0. \quad (1)$$

For calculating the refracted intensity in the DWBA (Distorted Wave Born Approximation) the dielectric function has to be divided into two parts [124-127]

$$\varepsilon(\vec{r}) = \bar{\varepsilon}(z) + \tilde{\varepsilon}(\vec{r}) = n^2(z) + \tilde{\varepsilon}(\vec{r})$$

with an average refractive index $n(z) = 1$ for $z < 0$, $n(z) = n$ for $z > 0$ and a spatial oscillating part $\tilde{\varepsilon}(\vec{r})$ diminishing for the outer space. Thus equation (1) can be transformed into

$$\nabla_x \nabla_x \vec{E}(\vec{r}, t) + k^2 n^2(z) \vec{E}(\vec{r}, t) = -\tilde{\varepsilon}(\vec{r}) \vec{E}(\vec{r}, t).$$

In the following only the homogenous equation will be considered accounting only for the specular reflectivity. For a x-ray wave with the wavevector \vec{k}_i impinging onto an interface between vacuum and matter the solution of the homogenous equation leads to a reflected beam with the wavevector \vec{k}_s and to a transmitted beam with the wavevector \vec{k}_t (see Figure 23). The amplitudes of these wave are given by the Fresnel equations [128]. For a linear to the incident plane polarised wave (σ -polarisation) the ratio of reflected to incident amplitude is given by

$$r_\sigma = \frac{E_r}{E_i} = \frac{k_i \sin \alpha_i - k_t \sin \alpha_t}{k_i \sin \alpha_i + k_t \sin \alpha_t}$$

and the ratio of transmitted to incident amplitude is given by

$$t_\sigma = \frac{E_t}{E_i} = \frac{2k_i \sin \alpha_i}{k_t \sin \alpha_t + k_i \sin \alpha_i}.$$

For a parallel to the incident plane polarised wave (π -polarisation) one obtains

3.5. X-ray Techniques

$$r_{\pi} = \frac{E_r}{E_i} = \frac{k_t \sin \alpha_i - k_i \sin \alpha_t}{k_i \sin \alpha_t + k_t \sin \alpha_i}$$

$$t_{\pi} = \frac{E_t}{E_i} = \frac{2k_t \sin \alpha_i}{k_i \sin \alpha_t + k_t \sin \alpha_i}.$$

As the reflected beam is not refracted the reflectivity is given by

$$R = |r|^2.$$

In the case of the transmittivity $\alpha_i \neq \alpha_t$ and one obtains

$$T = |t|^2 \frac{\sin \alpha_t k_t}{\sin \alpha_i k_i}.$$

The energy flux density is conserved. For R and T it follows

$$R+T=1.$$

For small incident angles like in the case of reflectivity one can simplify the term for the reflectivity by using the approximations $\sin \alpha \approx \alpha$ and $k_i \approx k_t$. Additionally the polarisation of the x-ray wave can thus be neglected. For the Fresnel reflectivity one obtains

$$R_F = |r|^2 = \left| \frac{\alpha_i - \sqrt{\alpha_i^2 - \alpha_c^2}}{\alpha_i + \sqrt{\alpha_i^2 - \alpha_c^2}} \right|^2.$$

Up to now only mathematically flat interfaces were considered in the reflectivity. In kinematical approximation the reflectivity of an electron density profile can be described by the so-called ‘‘Masterformula’’ [129]

$$R(Q_z) = R_F \left| \int g'(z) e^{iQ_z z} dz \right|^2 \quad (2)$$

with R_F as the Fresnel reflectivity of a bulk material, $g'(z)$ as the electron density gradient normalized to the bulk electron density and Q_z as the momentum transfer vertical to the

3.5. X-ray Techniques

surface. The Fresnel reflectivity is thus modified by the absolute square of the Fourier-transformed electron density gradient at the surface.

The most striking disadvantage of this simple kinematical theory is the loss of information in the near order below the critical angle of total reflection for more than one interface, as the transmitted and reflected amplitude ratios at the inner hidden interfaces are not taken into account. Additionally only the absorption of the substrate is accounted for in the Fresnel reflectivity. However, in real systems the absorption of the films may not be neglected.

The kinematic nature of the Master-formula is expressed through the fact, that it is only valid far away from the edge of total reflection and for neglectable absorption of the films. A more realistic picture of the interface is obtained by considering a Gaussian-like density gradient profile. The parameter σ in the density gradient

$$g'(z) = \frac{1}{\sqrt{2\pi}\sigma} e^{-\frac{z^2}{2\sigma^2}} \quad (3)$$

indicates microscopic Gaussian fluctuations at the interface.

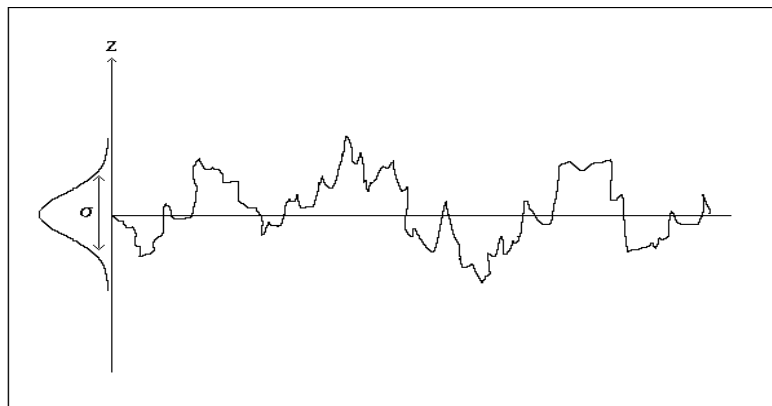


Figure 24: Gaussian like fluctuations of an interface with the projection onto the z-axis.

The Fourier transform of a Gaussian function is again a Gaussian, thus by inserting equation (3) in (2) one obtains

$$R(Q_z) = R_F e^{-Q_z^2 \sigma^2}.$$

Through a Debye-waller-like term the roughness σ leads to a steeper decrease of the Fresnel reflectivity. By plotting $\ln[R(Q_z)/R_F]$ against Q_z^2 one obtains a straight line with the slope σ^2 . The above described limitations of the Master formula are taken into account in a more general treatment by Névoit and Croce [130] and will be described in the following.

3.5.3. Parrat-Formalism

To judge quantitatively the reflectivity near the total reflection edge, it is necessary to take into account multiscattering effects [131]. Here the reflection and transmittance coefficients are calculated at each interface (see Figure 25).

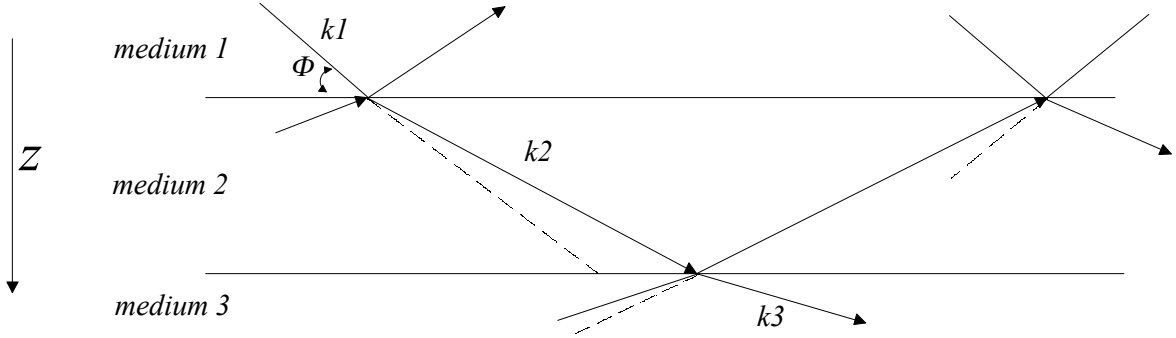


Figure 25: Reflected and refracted beams in a homogeneous medium.

As the angle Φ between incident and reflected beam under grating incident conditions is very small, one obtains

$$k_{2,x}^2 + k_{2,z}^2 = k_2^2 = n_2^2(k_{1,x}^2/\cos^2\phi) = k_{1,x}^2(1-2\delta_2-2i\beta_2+\phi^2).$$

For simplicity one can take

$$f_2^2 = \phi^2 - 2\delta_2 - 2i\beta_2, \quad f_1 = \phi, \quad n_2 = 1 - \delta_2 - i\beta_2 \text{ and } n_1 = 1 \text{ (vacuum).}$$

From the continuity of the tangential components of the electric field $k_{2,x} = k_{1,x}$ follows. For small angles Φ one has the approximation $k_{1,x} \approx k_1$. Thus one obtains $k_{2,z} \approx k_1(\phi^2 - 2\delta_2 - 2i\beta_2)^{1/2} = f_2$. The Fresnel reflection coefficient can be expressed by

$$F_{1,2} = \frac{E_1^R}{E_1} = \frac{\sin \Phi - n_2 \sin \Phi_2}{\sin \Phi + n_2 \sin \Phi_2} = \frac{f_1 - f_2}{f_1 + f_2} = \frac{\Phi - f_2}{\Phi + f_2}.$$

Due to the approximation in the last term this expression is valid for both polarisation components. From the continuity of the tangential components of the electric field of a n-layer system one obtains for the interface between the nth and the (n-1)th layer

$$a_{n-1}E_{n-1} + \frac{1}{a_{n-1}}E_{n-1}^R = \frac{1}{a_n}E_n + a_nE_n^R \quad (4)$$

and from the continuity of the tangential components of the magnetic field ($\vec{H} \propto \vec{k} \times \vec{E}$) it follows

$$\left(a_{n-1}E_{n-1} - \frac{1}{a_{n-1}}E_{n-1}^R \right) f_{n-1}k_1 = \left(\frac{1}{a_n}E_n - a_nE_n^R \right) f_nk_1. \quad (5)$$

3.5. X-ray Techniques

As the tangential components are accounted for in the middle of the respective medium, one obtains

$$a_n = e^{-ik_1 f_n \frac{d_n}{2}} = e^{-i \frac{\pi}{\lambda} f_n d_n}$$

as the amplitude factors a_n .

A simultaneous solution of the equations (4) and (5) can be achieved by dividing the sum through the difference of both equations. The resulting reflection coefficients R are derived from the simple Fresnel coefficients F by using the recursive formula

$$R_{n-1,n} = \left(\frac{R_{n,n+1} + F_{n-1,n}}{R_{n,n+1} F_{n-1,n} + 1} \right) \cdot e^{\left(-\frac{4\pi i}{\lambda} f_n d_n \right)}$$

where

$$F_{n-1,n} = \frac{f_{n-1} - f_n}{f_{n-1} + f_n}.$$

f_n is the product of the refractive index times the angle of incidence in the n^{th} layer, d_n is the thickness of the n^{th} layer. To solve the recursive equation one starts with a semi-infinite substrate as the n^{th} layer, where $R_{n,n+1}=0$. The intensity ratio of the reflected to the incident beam is given by the square modulus of $R_{0,1}$. Fluctuations of the interface position may be taken into account via a Debye-Waller-like damping factor for the reflected intensity. Assuming gaussian like height fluctuations at the interfaces, Névot and Croce [130] have derived

$$F_{n-1,n} = \frac{f_{n-1} - f_n}{f_{n-1} + f_n} e^{-8\pi^2 k_{n-1} k_n \sigma_n^2}$$

for the Fresnel reflectivity. The striking difference to the already for the Fresnel reflectivity mentioned roughness is that now the k -vector is accounted for at both adjacent media of the interface.

In contrast to other experimental techniques such as transmission electron microscopy x-ray reflectivity has the great advantage to be a non-destructive method. Another important property of this technique is that its efficiency does not depend on the crystalline quality. X-ray reflection primarily does not depend on periodic arrangements of atoms but is mainly sensitive to changes of the average electron density across surfaces and interfaces. X-ray reflectivity thus give information on submonolayer interfacial roughness [132] with an accuracy of about $\pm 10\%$ and it will be used in this work to compare the interfacial roughness between the different samples.

3.5. X-ray Techniques

3.5.4. X-ray Diffraction

High resolution x-ray diffraction is a non-destructive method that has been used in this work to characterise and quantify the Ge concentration and clustering within the SiGe films. The principle of this technique is based on the elastic scattering of an x-ray beam by the sample and collection of the scattered beams by a detector. The direction of the scattered beam can provide information on the crystal structure and the interplanar distances by the use of Bragg's law

$$2 \cdot d \cdot \sin \theta = n \cdot \lambda$$

where θ is the angle between the x-ray beam and the set of coherently scattering planes and d is the distance between the planes. A relationship between the Bragg's law and the reciprocal space can be obtained by using the Ewald sphere. The Ewald sphere is a sphere with the incident x-ray wave vector \mathbf{k}_{inc} as radius vector and placed in such a way that \mathbf{k}_{inc} points to the origin of the reciprocal space (see Figure 26). Diffraction will occur if the Ewald sphere intersects a second reciprocal lattice point (at \mathbf{G}). If the diffracted wave vector is \mathbf{k}_{diff} then the relationship $\mathbf{k}_{\text{diff}} = \mathbf{k}_{\text{inc}} + \mathbf{G}$ is obtained.

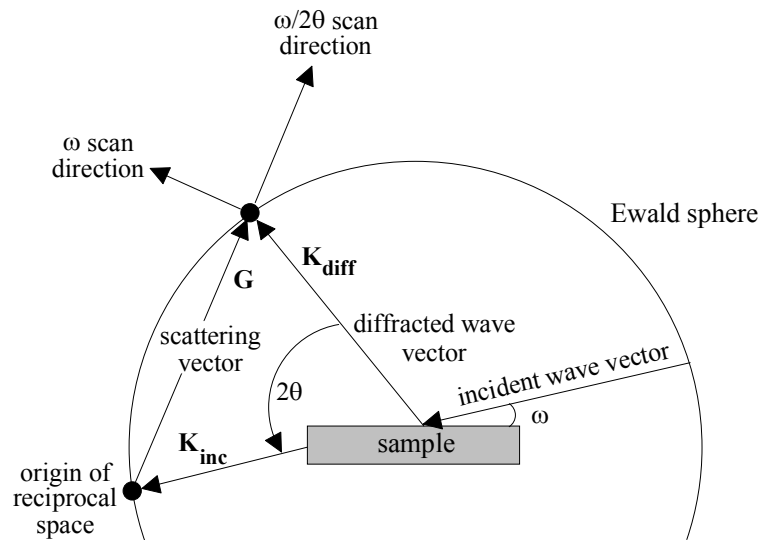


Figure 26: View of the scattering geometry used, showing the two perpendicular scan direction.

Diffraction data were obtained using the same setup as for the reflection experiments. Scanning the angle ω with fixed 2θ (rocking curve) probes different orientations of planes with a given plane separation, giving information about the crystalline quality in the form of the width of the diffracted peak.

3.5. X-ray Techniques

3.5.5. X-ray Topography

The aim of x-ray topography is to image the distribution and nature of imperfections within a crystal such as dislocation lines, stacking faults, precipitates, long range strains, twin boundaries and so on. The contrast on the topographs arises from the difference between the intensity diffracted by perfect and imperfect areas and the propagation properties of x-rays in slightly distorted crystals. Thus, in principle the position of defects in the crystal and their strain tensor can be determined.

A crude characterisation of the defects, such as their positions, is very easy and was also applied in this work. A careful interpretation leading to the value of the strain tensor around the defects is more difficult and requires the application of dynamic theory of diffraction in perfect and imperfect crystals. Topographic methods can be divided in two main groups:

- reflection methods: Incident and diffracted x-rays enter and leave the crystal surface at the same surface.
- Transmission methods: X-rays enter at a crystal surface and diffracted rays leave at the opposite surface.

As the topographs presented in this work were recorded in the reflection mode, the schematic in Figure 27 shall describe this technique a little further.

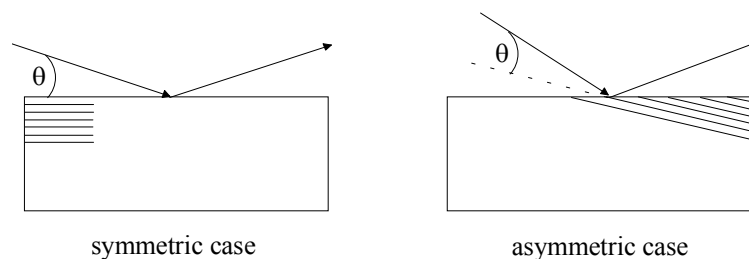


Figure 27: Reflection case of x-ray topography.

Each diffraction spot produced contains information on the whole crystal within that spot. By use of a fine pixel size detector, such as photographic emulsion, that information can be seen. Different parts of the crystal can contribute to the reflection at slightly different orientations over the reflection range.

Topographs in this work were obtained by using a perfect Si (100) oriented monochromator using the 422 asymmetric reflection for the $\text{CuK}\alpha$ line with a grazing incidence angle of 8.7 degrees and a Bragg angle of 44 degrees. The grazing incidence geometry with the same reflection was used for the sample crystal, thus obtaining a dispersion free setting.

3.6. Scanning Electron Microscopy

3.6. Scanning Electron Microscopy

The Scanning Electron Microscope (SEM) is a microscope that uses electrons rather than light to form an image. There are many advantages in using an SEM instead of a light microscope.

The SEM has a large depth of focus, which allows a large amount of the sample to be in focus at one time. The SEM also produces images of high resolution since the de Broglie wavelength of electrons is of the order of Angströms compared to the wavelength of visible light (~500 nm) which limits the resolution to ~200 nm in the case of optical microscopy. All SEM micrographs were obtained with a Philips SFEG 30 with a resolution of ~10 nm. Preparation of the samples is relatively easy since most SEMs only require the sample to be conductive. The combination of higher magnification, larger depth of focus, greater resolution, and ease of sample observation makes the SEM one of the most heavily used instruments in research areas today.

The Electron Source

Conventional electron guns extract thermoelectrons from the surface of metals, oxides or borides when they are heated to a high temperature. Field emission guns, like the Philips SFEG 30 used in this work, are based on field emission from sharp-pointed metal tips (curvature radius about 100 nm) when a very high voltage is applied to the surface. A strong electric field of about 10^7 V/cm is usually created at the cathode tip and electrons are emitted by tunnel effect.

Electrons are then accelerated by a voltage (commonly in the range 1-30 keV) and directed down to the center of an electron optical column, consisting of condenser lenses, stigmator lenses and an objective lense. These lenses cause a fine electron beam to be focused onto the sample surface. Scanning coils placed before the final lense cause the electron beam to be scanned across the specimen surface in the form of a square raster.

Electron Beam Specimen Interaction

The penetration of the primary electrons into the sample provokes the widening of the spot and a progressive loss of energy in deeper zones of the specimen. This defines a volume range of interaction between electrons and matter. The depth of the volume strongly depends on the type of substrate and on the beam energy. Typical values are 1 μm for a 20 keV beam on a specimen with a density of about 5 g cm^{-3} .

3.6. Scanning Electron Microscopy

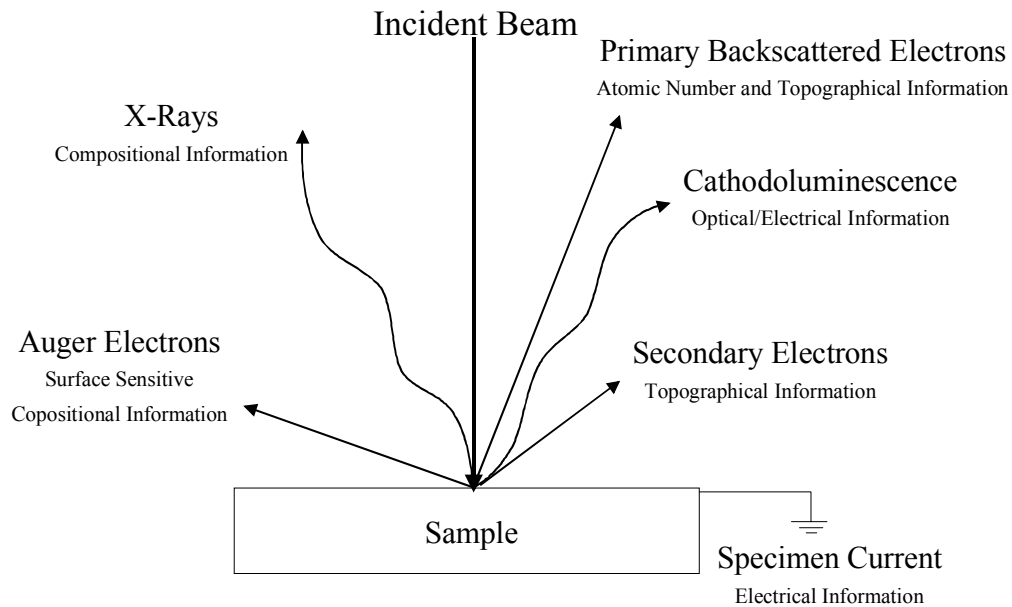


Figure 28: Electron specimen interactions: when the electron beam strikes the sample, both electrons and photons are emitted.

While all these signals are present in the SEM, not all of them are detected and used for information. The signals most commonly used are the secondary electrons, the back-scattered electrons and X-rays.

Using a Vacuum

When a SEM is used, the column must always be at a vacuum. There are many reasons for this. If the sample is in a gas filled environment, an electron beam cannot be generated or maintained because of a high instability in the beam. Gases could react with the electron source, causing it to burn out, or cause electrons in the beam to ionize, which produces random discharges and leads to instability in the beam. The transmission of the beam through the electron optic column would also be hindered by the presence of other molecules. Those other molecules, which could come from the sample or the microscope itself, could form compounds and condense on the sample. This would lower the contrast and obscure detail in the image.

Using the secondary electron detector produces a clear and focused topographical image of the sample. The backscattered electron detector produces an image that is useful when determining the make-up of the sample. Each element in the sample appears as a different shade, from almost white to black.

Depending on the acceleration voltage the primary electrons penetrate up to several micrometers into the sample. If a high material contrast is desired, high electron energies are chosen. In this case beside secondary electrons also elastically backscattered primary

3.6. Scanning Electron Microscopy

electrons are detected. As the latter ones originate from a high depth, the resolution is rather low. For topography imaging secondary electrons are used. These have low energies and can therefore leave the sample only from a near surface area (some nanometers). With this method structures of only a few nanometers can be mapped.

Secondary Electrons and Detection

Secondary electrons are specimen electrons that obtain energy by inelastic collisions with beam electrons. They are defined as electrons emitted from the specimen with energy less than 50 eV. Secondary electrons are predominantly produced by the interactions between energetic beam electrons and weakly bonded conduction-band electrons in metals or the valence electrons of insulators and semiconductors. There is a great difference between the amount of energy contained by beam electrons compared to the specimen electrons and because of this, only a small amount of kinetic energy can be transferred to the secondary electrons. An electron detector is used with the SEM to convert the radiation of interest into an electrical signal for manipulation and display by signal processing electronics.

Elastic Scattering of Primary Electrons

As the name implies, elastic scattering results in little ($<1\text{eV}$) or no change in energy of the scattered electron, although there is a change in momentum. Since momentum, $p=mv$, and m doesn't change, the direction of the velocity vector must change. The angle of scattering can range from 0-180 degrees, with a typical value being about 5 degrees.

Elastic scattering occurs between the negative electron and the positive nucleus. This is essentially Rutherford scattering. Sometimes the angle is such that the electron comes back out of the sample. These are backscattered electrons.

Inelastic Scattering

During inelastic scattering, energy is transferred to the electrons surrounding the atoms and the kinetic energy of the energetic electron involved decreases. A single inelastic event can transfer a various amount of energy from the beam electron ranging from a fraction to many keVs. The main processes include phonon excitation, plasmon excitation, secondary electron excitation, continuum X-ray generation, and ionization of inner shells. In all processes of inelastic scattering, energy is lost, though different processes lose energy at varying rates.

3.7. High Resolution Transmission Electron Microscopy

Specimen Preparation

There are two basic types of SEM's. The regular SEM requires a conductive sample. An environmental SEM can be used to examine a non-conductive sample without coating it with a conductive material. Three requirements for preparing samples for a regular SEM are:

- 1) Remove all water, solvents, or other materials that could vaporize while in the vacuum.
- 2) Firmly mount all the samples.
- 3) Non-metallic samples, such as oxides should be coated so they are electrically conductive. Metallic and highly conductive samples such as the indium-tin-oxide films can be placed directly into the SEM.

3.7. High Resolution Transmission Electron Microscopy

Medium and high-resolution cross-sectional transmission electron microscopy (HRTEM) was used by Dr. S. Christiansen at the University of Erlangen to perform microstructural characterisation of some of the structures studied in this work. As the author himself was not involved in these studies in the following only a very brief explanation of TEM is given. The technique essentially utilises the interaction of a 120 keV (medium resolution) or 300 keV (high resolution) electron beam with the crystal structure of the sample.

Sample Preparation

To allow transmission of the electrons through the structure, the samples need to be thinned to a thickness of $\approx 5\text{-}500$ nm [133,134]. In the pre-analysis sample preparation for cross-sectional microscopy, one or more samples are stacked together face-to-face. A thin slice of 0.5 mm perpendicular to the interface is then cut from the stack. The slice is mechanically polished to a thickness of ≈ 100 μm . They are then polished mechanically using diamond paste with decreasing size (3 μm , 1 μm , 0.25 μm) and finally chemomechanically polished. To mechanically stabilise the sample during further preparation and in the TEM specimen holder a copper-ring is glued onto the polished samples. The sample backside is essentially prepared following the same procedure resulting in a thickness < 1 μm . As a last preparation step, short term ion milling (< 30 min) with 3 keV Ar^+ ions is performed from the substrate backside. During ion beam etching the sample is cooled by liquid nitrogen, to prevent structural changes due to heating. Accelerating voltage and local current of the ion beam of about 0.5 mA are selected according to experience and lead to a smooth surface.

3.7. High Resolution Transmission Electron Microscopy

Microscope Equipment

Transmission electron microscopy has been performed with a Philips EM 400 (120 kV) and Philips CM 300UT (300 kV) for structural investigations down to an atomic scale, the latter one with a point-to-point resolution of 0.165 nm at 300 keV.

The scattering of the electron beam gives rise to Bragg diffraction beams emerging from the sample at an angle 1-2° from the transmitted direct beam in addition to the low-angle inelastic scattering [135]. A set of lenses and apertures is used in the microscope in order to focus and magnify the image or diffraction pattern of a certain illuminated area of the sample. The bright-field image is produced by placing an aperture in the objective lens (the lenses situated immediately below the specimen position) to remove Bragg reflections and allowing only the transmitted beam to be projected on the microscope screen [133,135]. On the other hand, dark-field images can be formed by displacing the aperture to receive one diffracted beam or by tilting the illumination so that the required beam passes down the axis of the objective lens. The choice of a particular imaging mode depends on the nature of the studied structure and microstructure of interest. The diffraction mode can be used to provide information about the reciprocal lattice symmetry, helping in the identification of the crystalline character of the material, besides identification of phases and ordering effects [135].

In this work the bright-field image was used as an overall identification of the structural contrasts evident from the material.

4. Experimental Setup

4. Experimental Setup

In this chapter the experimental set-ups of the different characterisation techniques used in this work are described.

4.1. X-Ray Diffraction and Reflectivity

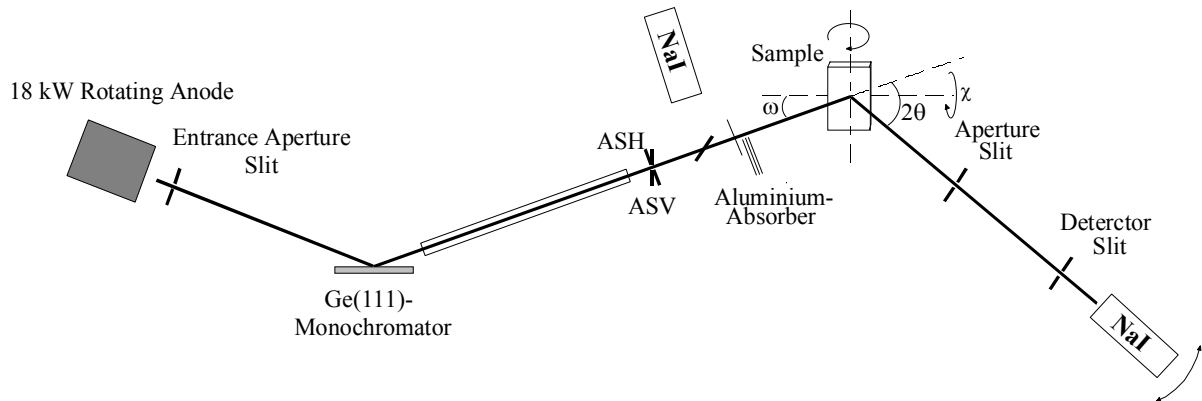


Figure 29: Experimental setup used for the reflectivity and diffraction measurements.

Figure 29 schematically depicts the experimental set-up of the x-ray experiments used at the LS Prof. H. Dosch of the Institute of Materials Science with the Help of Dr. A. Rühm. The “white x-ray beam” of the Cu rotating anode hits a Ge(111) monochromator, which is set to the Bragg angle of the characteristic $\text{Cu}_{K\alpha}$ -doublet.

Via the entrance aperture slit it is possible to reduce the beam diameter so that only a well defined area of the monochromator is illuminated (to avoid edge effects).

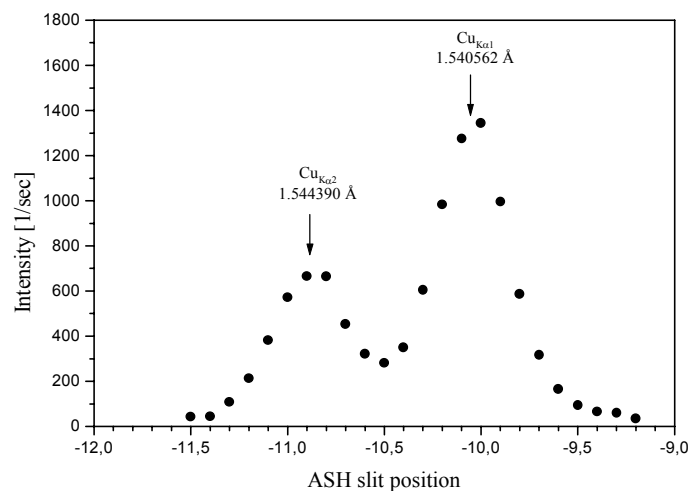


Figure 30: Aperture scan through the x-ray beam cross-section.

The monochromator reflects two sharp peaks $\text{Cu}_{K\alpha 1}$ and $\text{Cu}_{K\alpha 2}$, which can be well separated. Before the horizontal aperture slit ASH the x-ray beam cross-section has the

4.1. X-Ray Diffraction and Reflectivity

form given in Figure 30, clearly showing the good separation of the two lines. With the horizontal aperture slit (ASH) one can select the factor of two stronger $\text{Cu}_{K\alpha 1}$ line reducing further the beam divergence. In this experiment a line focus was chosen to obtain higher intensity. The beam height can be modified with the vertical aperture slit ASV so that only the sample is illuminated. All horizontal slits were set to 0.4 mm resulting in a 2θ resolution of 0.05° (FWHM).

To correct for intensity variations of the source caused e.g. by vacuum or voltage fluctuations, a second NaI scintillation detector was used as a monitoring counter of partially diffracted intensity through a Capton foil. At each measuring point the intensity was integrated to a certain constant monitor rate. Fluctuations of the primary beam intensity thus were corrected by different integration times.

With a remote controlled Aluminium absorber system the beam intensity could be controlled to protect the detector. To reduce air diffraction and absorption the beam was directed through evacuated tubes. The sample was mounted on a triple axis diffractometer enabling three degrees of freedom for the sample rotation.

4.1.1. Sample Alignment

For x-ray reflectivity experiments an accurate sample alignment is essential. At the beginning of the experiments the rotation centre of the diffractometer was checked. By scanning the sample in the beam it was then ensured that the beam hits the central point of the sample. This procedure revealed a homogeneously reflecting sample over the whole sample area pointing to a very flat sample with no bending. At the end the sample was aligned parallel to the primary beam. Finally due to the very small horizontal aperture slit it was checked at several reflection angles that the reflected beam is not cut by one of the used slits. As the maximum of the reflected beam was always passing through the slits this indicated a good alignment of the system and the sample.

4.1.2. Illumination Correction

Figure 31 shows the influence of the limited sample size on the reflected x-ray intensity under grazing incidence. In the theoretical derivation of the x-ray reflectivity an infinite sample size was assumed. In the experimental case the limited sample size must be taken into account as this strongly affects the reflected intensity. Instead of a plateau at small

angles the limited sample dimension leads to an increasing reflected intensity till the edge of total reflection.

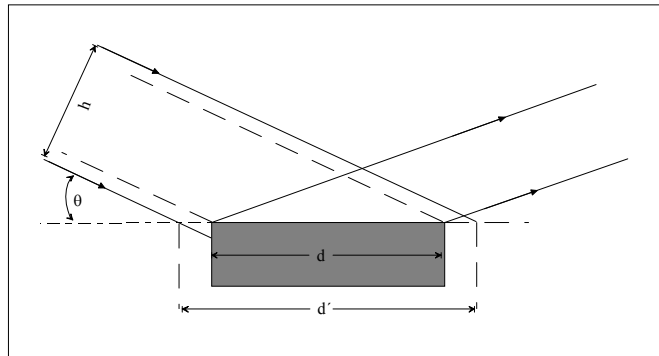


Figure 31: Influence of the limited sample dimension on reflectivity measurements.

The sample reflects only a part of the incident beam since the sample is not completely immersed in the incident beam, especially not for very small angles, the ideal Fresnel reflectivity is reduced by the ratio d/d' , where d is the sample width and

$$d' = \frac{d}{\sin \theta}$$

is the projection of the beam onto the sample area.

The illuminated area of the sample and thus the measured reflected intensity is increasing with increasing angle θ between the incident beam and the sample until the sample is completely illuminated in the beam at an angle $\theta^* = h/d$ with h being the height of the beam. In the fitting procedure of the experimental data the theoretical curve must be corrected by a factor

$$A = \frac{d}{h} \sin \theta.$$

The beam height was set to 3 mm. With a sample size of 4.5 mm one thus has to perform this correction up to an angle of $\theta = 0.67^\circ$.

4.2. Photo- and Electroluminescence

The PL experiments were performed at the University of Glasgow (while the labs in Wuppertal were refurbished) and at the University of Wuppertal. As setting up a PL system in Wuppertal was part of this PhD work, it shall be described in more detail in the following. The main difference between the set-ups in Wuppertal and Glasgow was the use of a 1 m single-grating spectrometer in Glasgow in contrast to a double grating

4.2. Photo- and Electroluminescence

spectrometer with a focal length of 0.22 m in Wuppertal. In addition, the set-up in Glasgow consisted of a helium flow cryostat operating at a temperature range between 4.2 – 320 K whereas the closed cycle cryostat in Wuppertal could cool the samples down to 14 K.

The reciprocal angular dispersion is given by

$$\frac{d\lambda}{dl} = \frac{1}{f} \frac{d\lambda}{d\theta}$$

with f = focal length

$$\frac{d\theta}{d\lambda} = \frac{n}{d \cdot \cos\theta} = \text{the angular dispersion of a monochromator,}$$

$dl = 1.5 \text{ mm} = \text{width of the entrance and exit slit,}$

$n = 2 = \text{the diffraction order}$

and $d = 600 \text{ lines/mm} = \text{spatial period of the grating ruling.}$

With $\cos\theta \rightarrow 1$ one therefore obtains a spectral angular dispersion of 5 \AA for the spectrometer in Glasgow and 7 \AA for the spectrometer in Wuppertal.

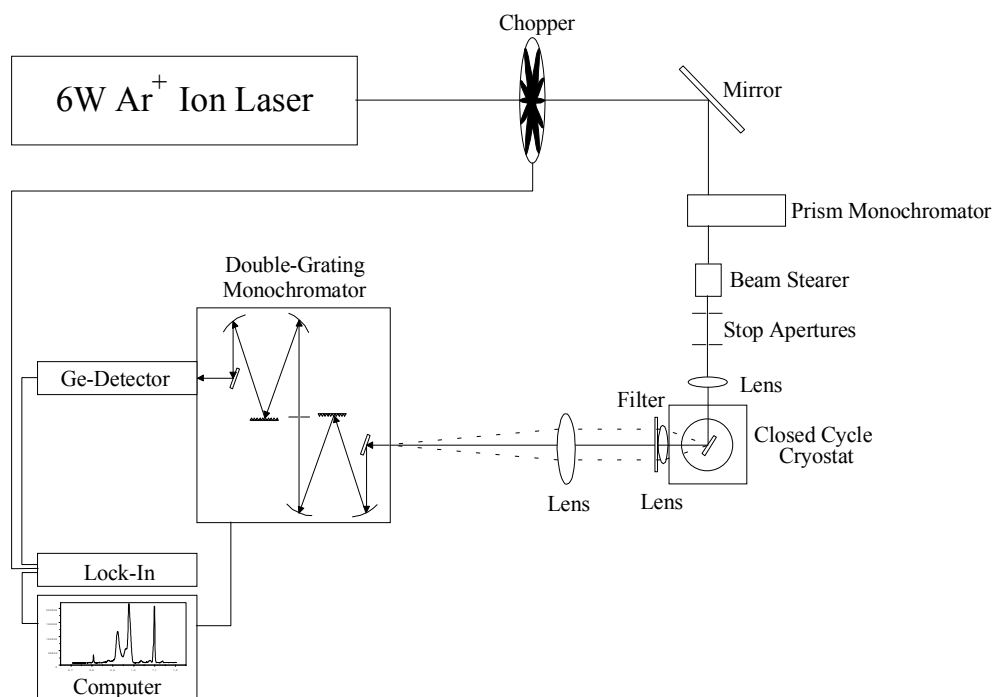


Figure 32: Schematic drawing of the luminescence setup.

Laser

When the luminescence of the sample is particularly weak, a laser source must be used for pumping excitation. In these experiments the excitation came from a 6 W Argon (Ar⁺) ion laser (Spectra Physics stabilite 2017) which was operated at a wavelength of 514.5 nm. This excitation light was modulated at a frequency of 590 Hz using a mechanical chopper.

4.2. Photo- and Electroluminescence

Prism Monochromator

To filter plasma lines out of the excitation laser beam of plasma lines which are inevitably produced in a plasma source, a Spectrolab Laserspec III prism monochromator consisting of three small prisms was used. Using the aperture 10 of the laser, a transmission of about 65% was measured for the prism monochromator.

Closed Cycle Cryostat

An Oxford Instruments closed cycle cryostat mainly consists of an Edwards CS2/9 cooling head and a water cooled compressor (Edwards Cryodrive 1.5) which compresses He gas to 16.5 bar. The He gas is transferred through a pair of flexible He lines to a shutter unit inside the cold head where it expands and is pumped back to the compressor. The expansion at the cooling head leads to a cooling of the head down to about 10 K. An ITC controller (Oxford 503) measures the temperature of the cooling head (and of the sample) and adjusts the gas flow (and thus the temperature) so that the pre-set cooling head temperature is stabilised. The temperature stability obtained by the ITC controller is ± 0.5 K.

Double-Grating Monochromator

To detect the light a SPEX double monochromator was used. As a part of the set-up a Testpoint program was written driving the monochromator and reading out a lock-in.

The monochromator allows only the selected wavelength of light to pass through it. As a double spectrometer it minimises spectral contamination due to stray light by a factor four in comparison to an identical single spectrometer [57]. The incoming light is directed by a 45° mirror to a collimating mirror, which focuses the light on the first grating. Here the light is dispersed onto a second collimating mirror. Since the grating spreads the light according to wavelength, only a narrow band of light can pass through a quadratic pinhole to the second section of the monochromator. Again the light is dispersed and further purified before the selected wavelength is directed through an exit slit onto the Ge-detector. To vary the wavelength of light passing the SPEX 1680, both gratings are rotated simultaneously in the same direction. This additive-dispersion coupling is responsible for the high wavelength resolution. Using two gratings with a ruling of 600gr/mm a resolution of 7 Å was obtained setting identical entrance and exit slits of 1.5 mm.

It is not necessary to take into account the spectral response of the PL system as the same setup was used for all measurements without any changes. During the PL experiments only the samples were changed inside the cryostat.

4.2. Photo- and Electroluminescence

Ge-Detector

To collect the light at the exit slit of the spectrometer a North Coast EO-817L Ge detector was used, consisting of a LN₂ cooled p⁺-i-n⁺ photodiode. For IR detectors the cooling is essential to avoid thermally generated electron-hole pairs in the detector material. The Northcoast Ge detectors are sensitive in a spectral range between 0.8 and 1.7 μm.

4.3. Raman Spectroscopy.

4.3. Raman Spectroscopy

Figure 33 shows the schematic of the setup used for the Micro-Raman experiments. The entrance optics of the Dilor modular XY800 spectrometer focuses the laser beam on the sample, reduces stray light and collects the scattered light. With the setup one can choose between a Macro- and Micro-Raman mode. However, in this work all experiments were performed in the micro-Raman mode using an Olympus BX40 microscope to focus the laser beam to a spot diameter of about 3 μm (with the x100 objective). For the 25mW power level used in these experiments this produced a power density on the sample in the 2kWcm^{-2} range. The power was measured after the microscope objective at a distance of about 20 mm from the sample surface. The samples were measured at room temperature in air environment.

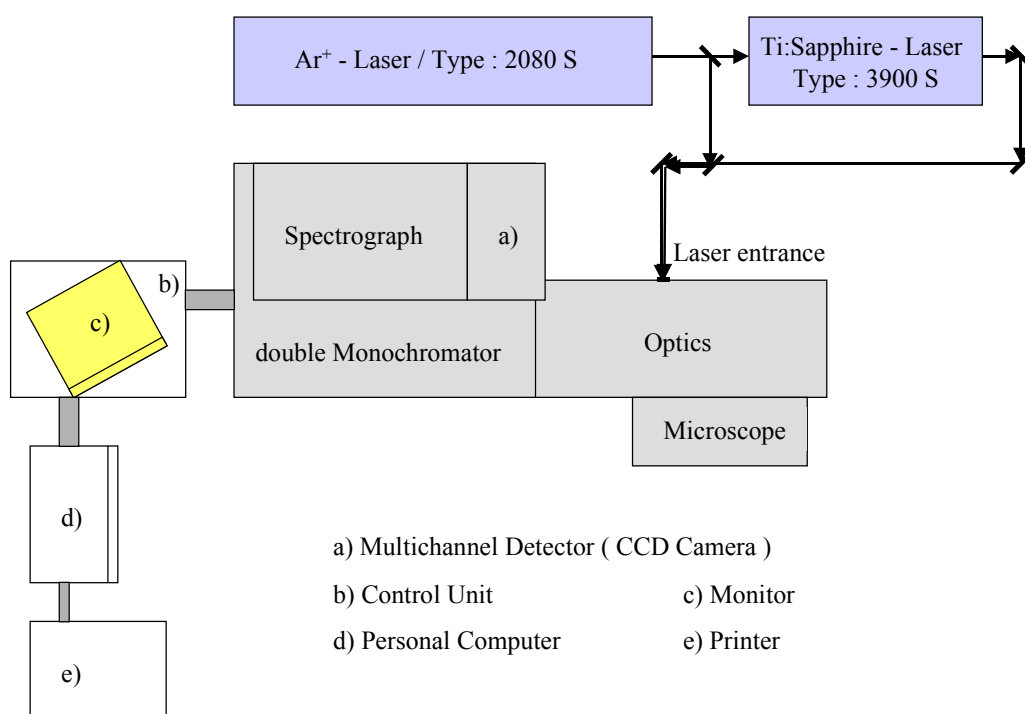


Figure 33: Schematics of the Micro-Raman set-up using an XY800 triple axis spectrometer (top view).

The Dilor modular XY Raman spectrometer system is essentially composed of a double monochromator and a spectrograph. In this experiment the double monochromator was used in the subtractive mode to provide a wide detection range to the spectrograph and to increase the signal. The path of the beam through the double monochromator is shown in Figure 34.

4.3. Raman Spectroscopy.

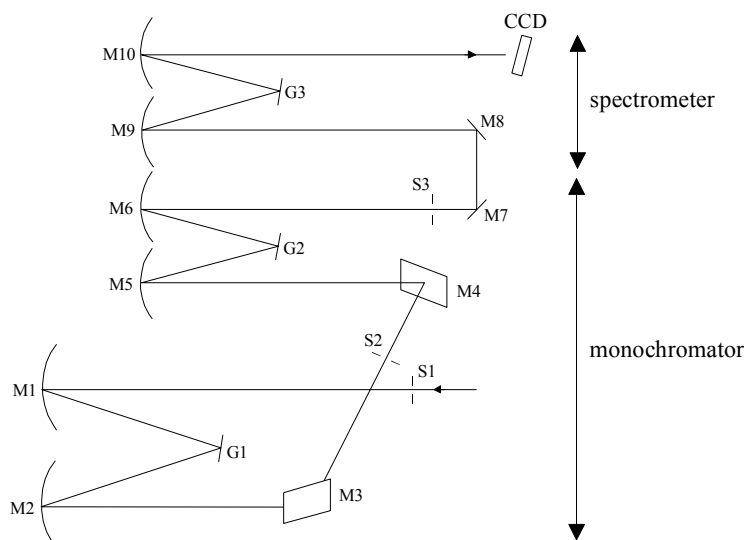


Figure 34: Optical path inside the double monochromator in the case of the subtractive mode (as used for all experiments).

Two plane holographic gratings with 1200 groves/mm are used as a pre-filter for the monochromator. The spectrograph contains a 1200 groves/mm grating allowing a spectral coverage of 31000 to 11000 cm^{-1} (322.5 to 909.0 nm). In the subtractive mode slits S1 and S3 are determining the resolution and have to be set to the same value. S2 reduces the stray light. The resolution was determined experimentally by measuring the laser line at different slit widths. As the laser line is much smaller than the slit widths used in this experiments, this technique is valid to approximately determine the upper limit of the resolution.

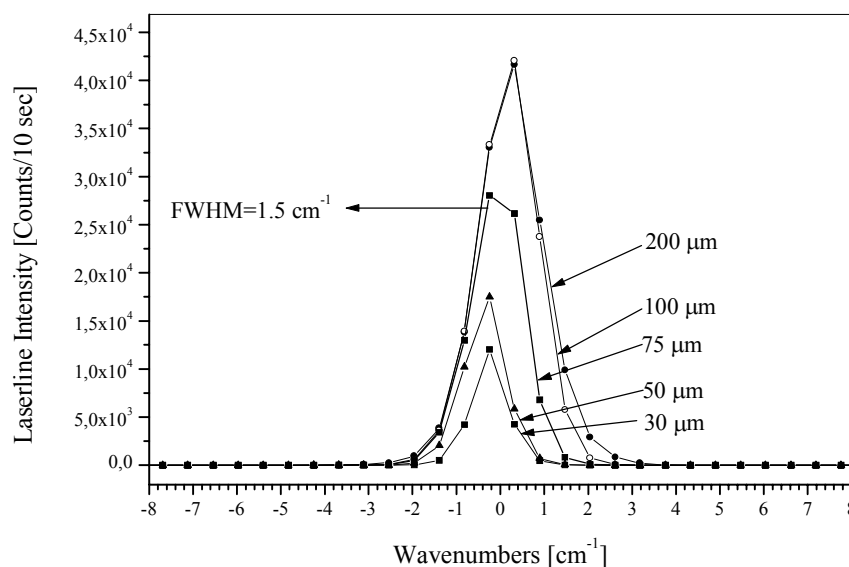


Figure 35: Widths of the 514.5 nm laser line recorded at different slit sizes in the subtractive mode. Raman spectra were recorded at a slit width of 75 μm , resulting in a resolution better than 1.5 cm^{-1} .

4.3. Raman Spectroscopy.

All Raman experiments were performed in the subtractive mode with a slit width of 75 μm resulting in a resolution $\leq 1.5 \text{ cm}^{-1}$. In the additive mode the resolution would be 0.6 cm^{-1} using a slit width of 75 μm . However, the intensity was too small to detect any signal from the SiGe samples.

A LN_2 cooled SpectrumONE CCD (Charged Coupled Device) was used as a detector. The vertical extent of the detector was large enough to capture all of the Raman scattered light from the illuminated sample.

4.4. High Vacuum-Thermal Evaporator for ITO Deposition

As the luminescence of the Si/SiGe MQW samples is emitted through from the surface, it is essential to have a very weakly light absorbing electrical top contact. In many cases grid- or ring-contacts are used to inject the current, while the light can still pass through between the contacts. However, this leads to an inhomogeneous current distribution and to a still non-negligible absorption by the metallic layers.

Ideally one would therefore favour an electrical contact that is optically transparent. One of the material systems commonly used i.e. for heterojunction solar cells [136] is the ternary alloy Indium-Tin-Oxide (ITO). By modifying the growth parameters of the ITO films, it is possible to tune the optical and electrical properties in a wide range.

Basically, ITO is an In_2O_3 alloy highly doped with Sn leading to an excessive number of electrons of about 10^{21} cm^{-3} . The high electron density strongly depends on the Sn concentration. The best ratio of In:Sn was found to be 90:10 [137,138].

Such films can have a transparency of about 90% in the visible light range while still showing a sheet resistance as low as $10^{-4} \Omega\text{cm}$. The high electron density causes plasma oscillations with a characteristic wavelength in the infra red [139], resulting in a high reflectance of about 90%. The lower limit of transparency is 345 nm, which corresponds to the direct bandgap of ITO of 3.6 eV. The upper limit lies in the IR and is caused by plasma oscillations due to the high electron density. For a detailed analysis of ITO films, the reader is referred to the extensive literature and especially also to reference [140].

Various techniques such as sputtering from a metal alloy target of In:Sn [141], reactive DC sputtering from an oxide target [138], reactive r.f. sputtering from oxide targets [142], spray pyrolysis [139], chemical vapour deposition [143], electron beam evaporation [144] or thermal evaporation of metallic alloys [145] were reported to deposit thin ITO films.

In the case of sputtered films, or in the case of thermal evaporation of an alloy, one is restricted to a certain fixed In/Sn ratio. Additionally, the different vapour pressures for In and Sn present a problem. Thus, even if one starts from an ideal 90:10 alloy of In/Sn, the Sn concentration in the films will be significantly lower.

Therefore, as a major part of this work a high vacuum chamber with two distinct effusion cells for In and Sn as well as an electron-beam evaporator (not shown in Figure 36) was designed and set-up in co-operation with the company "MBE-Komponenten". The schematic drawing of the system is shown in Figure 36.

4.4. High Vacuum-Thermal Evaporator for ITO Deposition

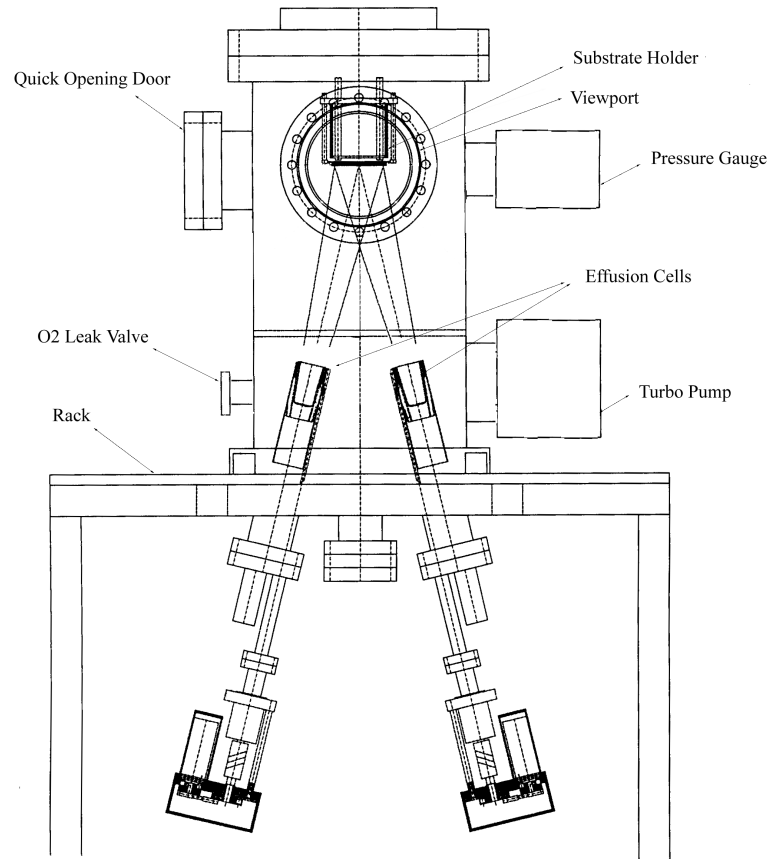


Figure 36: Schematic drawing of the high vacuum chamber for ITO deposition. In and Sn are evaporated from two different effusion cells at the bottom of the chamber. The oxygen bottle, connected at the O₂ leak valve, is not shown.

In this way one can easily modify the In/Sn concentration ratio to optimise the condition for high conductivity and high transparency. This is essential to offer the possibility to vary the wavelength region with the highest optical transparency. Detailed studies to investigate the phase diagram are currently in progress.

In the following chapter a detailed description of the system is given.

4.4.1. Pumping System

An oil free running diaphragm pump (Vacuubrand MZ 2T) was used as a pre – vacuum pump for a turbo molecular pump. With a pumping capacity of 2.1 m³/h, an end pressure of less than 9 mbar is achieved which is good enough as a pre vacuum for the turbo molecular drag pump (Pfeiffer TMU 065).

At a rotation speed of 90000 min⁻¹ the volume flow rate for N₂ is 56 l/s. The base pressure of the system is $\leq 8 \cdot 10^{-8}$ mbar.

4.4. High Vacuum-Thermal Evaporator for ITO Deposition

4.4.2. Substrate Heater and Sample Holder

To work near the optimum conditions it is essential to control the substrate temperature. Substrate heating in vacuum is, as in our case, often done by electromagnetic radiation. Thus, one achieves a repeatable temperature setting without contaminating the substrates or applying mechanical strain in our case. The heater can be operated at temperatures up to 750 °C. The main problem is, that there exists no suitable technique for the measurement of low temperatures (<500 °C). Commercially available radiation pyrometers determine the shape of the emission curve of a black body emitter through measuring at two wavelengths (mostly at 2.0 μm and 2.6 μm) and from this calculate the temperature. However, due to the weak emission at low temperatures this does not work at less than 400 °C. In this work the temperature of the heater was used as a relative temperature resulting in an error of about 50 °C. For later applications a thermocouple can be installed right beside the substrate and the temperature coupling can be realised with an ultrahigh vacuum ceramic glue that can also be used at high temperatures.

4.4.3. Pressure Measurement

A single gauge controller (Balzers TPG 251 A) controls a compact full range gauge (Balzers PKR 251) consisting of a Pirani and a cold cathode gauge system. The pressure range is from $5 \cdot 10^{-9}$ to $1 \cdot 10^3$ mbar.

The Pirani gauge consists of a wire filament with a high temperature coefficient which is heated by a constant current. In the low vacuum range ($> 10^{-4}$ mbar) the thermal conductivity of gases is pressure dependent. Thus, the supplied heat power is a value for the pressure inside the chamber.

The cold cathode gauge employs the principle of gas ionisation at a cold cathode. A magnetic field inside a discharge area forces electrons on a helix course on their way from the cathode to the anode. Thus even at low pressures one achieves a high enough amount of ionising collisions. Keeping anode current and magnetic field constant, the discharge current is related to the pressure in the chamber for a specific reference gas mixture. The great advantage of a cold cathode is its ruggedness against reactive gases such a fluorine or oxygen.

4.4. High Vacuum-Thermal Evaporator for ITO Deposition

4.4.4. Oxygen Supply

The oxygen required during the ITO growth was supplied via an all metal leak valve (Vacuum Generators, MD series). This allows a very accurate control of the oxygen flow into the vacuum system from an external oxygen cylinder (99.999% purity). Leak valves use the same principle of sealing as do other all-metal valves. A softer metal pad (in this case copper) is pressed against a harder metal seat. The knife edge of a leak valve has a truncated profile which allows the passage of gas to be carefully controlled as the sealing force is released. The relative movement between knife edge and sealing pad is accurately controlled.

With the all-metal valve the oxygen partial pressure inside the chamber can be continuously controlled between 10^{-3} and 10^{-11} mbar. The leakage rate is $<10^{-11}$ mbar ls^{-1} .

4.4.5. Evaporation Rates and Quartz Monitor

To control the In:Sn ratio, it is essential to determine the evaporation rate of each metal. The rate was measured in a conventional manner using a quartz crystal monitor. Figure 37 shows the measured rates against the temperature of the effusion cells.

For both metals an exponential dependence was found. The exponential fits to the data are also shown in Figure 37. Due to the higher vapour pressure of In the rates are much higher than compared to Sn. The exponential rates are as following:

$$\text{In: } r[\text{\AA} / \text{s}] = 0.035 \cdot e^{\frac{T[\text{C}^{\circ}] - 633.885}{56.109}}$$

$$\text{Sn: } r[\text{\AA} / \text{s}] = 0.003 \cdot e^{\frac{T[\text{C}^{\circ}] - 633.820}{50.655}}$$

4.4. High Vacuum-Thermal Evaporator for ITO Deposition

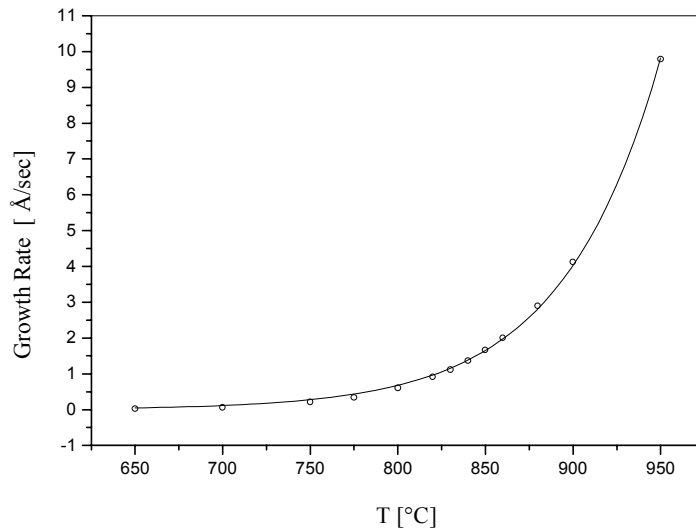


Figure 37: Growth rates for indium.

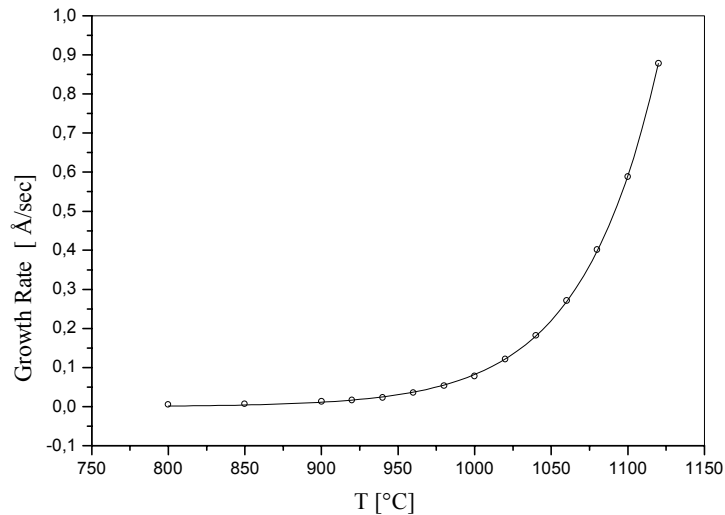


Figure 38: Growth rates for tin.

4.4.6. Tooling Factor

To measure the thickness of the deposited layers a quartz crystal monitor was used, which can derive the thickness of a layer from the deposited mass of the material. However, to correct for the geometrical displacement of the quartz monitor from the substrate, the tooling factor of the equipment had to be determined first. However, both metals In and Sn and also any alloy did not properly wet neither the Si nor the glass substrates.

Therefore, a thin Cr layer was evaporated by the e-flux evaporator installed in the same chamber and at the same height as the effusion cells. Figure 39 shows a height profile along the edge of a Cr layer deposited through a metallic mask. The profile was recorded

4.4. High Vacuum-Thermal Evaporator for ITO Deposition

using a Surface Profiler Dectac3ST from Veeco. Whereas the quartz monitor indicates a thickness of 254 Å the measured thickness was about 294 Å, resulting in a tooling factor of 1.55. Thus, all the indicated values of the quartz monitor have to be corrected by this factor.

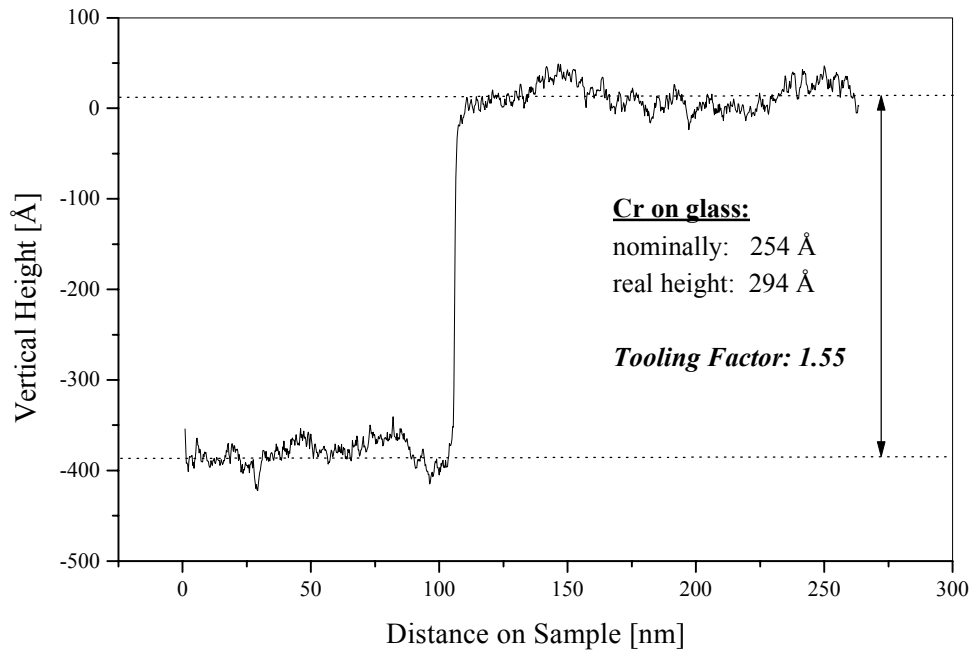


Figure 39: Height profile of a Cr layer on a glass substrate. The ratio of real height to nominal height is used to calculate the Tooling factor of the quartz monitor.

4.4.7. Electrical Characterisation:

The resistivity of lateral electrical transport in films deposited by thermal evaporation was measured by the four-point-probe technique. Isolation between the film and the substrate was provided by depositing the film on glass substrates.

A four-point-probe resistivity measurement is usually carried out by passing a small constant current I through the outer two of 4 parallel probes contacting the material under study.

The voltage drop V is measured between the two inner probes, as schematically shown in Figure 40. If the sheet was an infinite conducting plane, the resistivity would be

$$\rho = \frac{V}{I} \frac{\pi}{\ln 2} [146,147].$$

4.4. High Vacuum-Thermal Evaporator for ITO Deposition

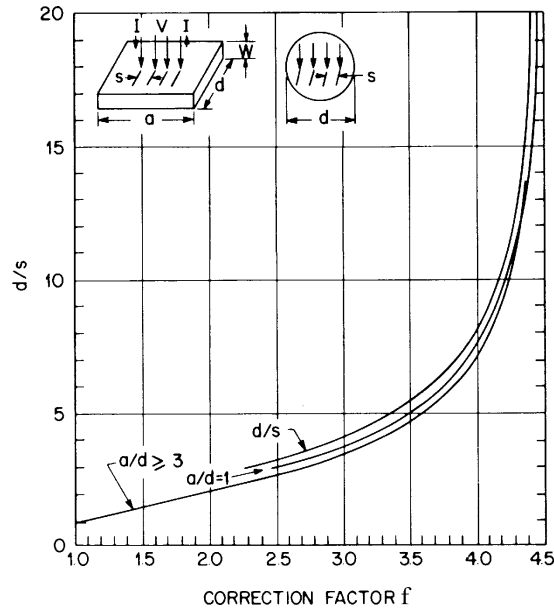


Figure 40: Correction factor and basic set-up for resistivity measurement by the four-point-probe technique (after [147]).

For a sheet corresponding to an epilayer of thickness W and lateral dimensions $a \cdot d$, voltage gradients will arise normal to the surface. In this case, the sheet resistance becomes [146,147]

$$\rho = \frac{V}{I} \cdot W \cdot f ,$$

with the introduction of a correction factor f which depends on the ratio of the probe spacing s and the sheet lateral dimension d perpendicular to the probe line. f is given in Figure 40 for a rectangular sheet layer of dimensions $a \cdot d$ and a circular sheet layer of diameter d [146,147]. f depends essentially on the ratio d/s and approaches the value $\pi/\ln 2 \approx 4.5$ for samples with dimensions much larger than the probe spacing. Resistivity measurements by this technique can be reproduced to $\pm 2\%$ if appropriate current levels and probe pressures are chosen [148]. Our measurements are performed with a home-made equipment. The applied pressure is fixed and given by the spring constant of the springs inside the probes and by the mechanical set-up of a tripod probe holder.

5. Results and Discussion

5.1. MBE Samples

Two of the samples examined in the present work (L6 and I17) were grown in a Vacuum Generators V-80 solid source MBE reactor. Prior to the growth the undoped CZ Si(001) wafers were cleaned using the RCA process (see 5.4.3.1).

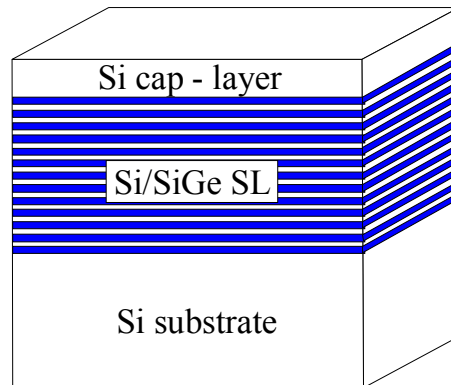


Figure 41: Schematic structure of the two samples grown by MBE. The active region consists of a 15 period Si/Si_{0.75}Ge_{0.25}/Si multiple quantum well layer.

Figure 41 schematically shows the structure of the two samples. To eliminate the influence of remaining contamination at the interface between the (100) Choichalski (CZ) n-Si substrate (Sb doped to $\rho \approx 6 \Omega\text{cm}$) and the epilayer as well as point defects on the surface, an 80 nm undoped Si buffer layer was grown. On top of this buffer the actual heterostructure consisting of a 15 period nominally undoped Si/Si_{1-x}Ge_x/Si multiple quantum well was grown. The thickness of the SiGe layers was chosen very thin (3.0nm) to achieve a sufficient confinement of the carriers. Such a thin Si_{0.75}Ge_{0.25} layer is fully strained without the formation of misfit dislocations. During the growth of the multiple quantum well $\frac{1}{2}$ ML Sb was used as a surfactant to keep the SiGe layers flat. The Si barrier layers prohibits the spreading of the hole wavefunction (3.1 nm). The final layer was a 42 nm B-doped ($5 \cdot 10^{18}$) Si cap deposited to saturate SiGe dangling bonds which would otherwise lead to a strong non-radiative recombination. Additionally, as mentioned in section 2.2.5 the MQW structure can be kept fully strained with the assistance of the cap layer.

5.1. MBE Samples

The growth parameters were the same for both samples. Only the MQW was grown at 600 °C, in the case of the sample L6, and at 650 °C, in the case of the sample I17. Two different temperatures were chosen to examine to role of the growth temperature on the structural properties of Si/SiGe heterostructures. It was expected that a lower growth temperature would lead to flater interfaces and to a stronger statistical distribution of the Ge atoms within the alloy and thus to a smaller degree of Ge clustering.

5.1.1. Emission Spectrum

5.1.1.1. Temperature Dependence

Figure 42 shows the temperature dependence of the PL of sample I17 (left) and L6 (right). At higher temperatures only band-to-band ($\text{Si}^{\text{TO}}_{\text{B-B}}$) recombination is visible in the case of sample I17.

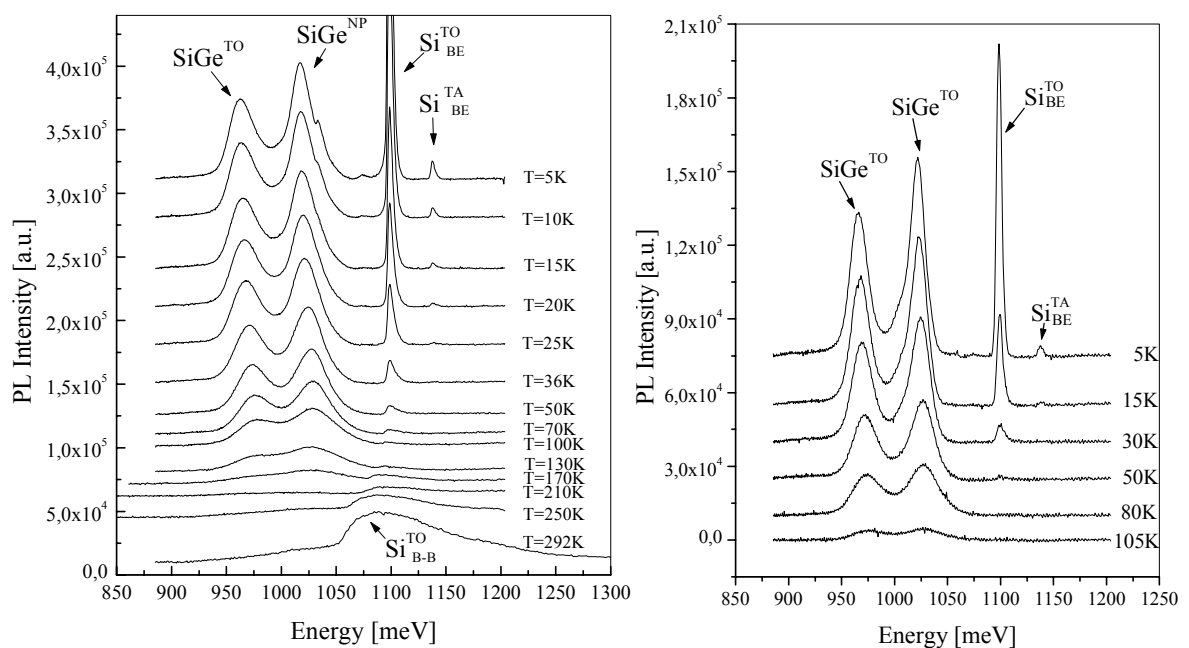


Figure 42: Temperature dependent PL spectra of sample I17 (left) and of sample L6 (right) obtained at an excitation power density of 480 W/cm².

An increase in the quenching temperature from 105 to 210 K and a SiGe intensity increase by a factor of two was consistently observed in repeated measurements on sample I17 grown at 650 °C compared to sample L6 grown at 600 °C. These results point to an increased number of point defects (possibly vacancies and vacancy-oxygen complexes) within the Si barrier layers, that have been identified as effective non-radiative competing channels by optically detected magnetic resonance [149]. However, although great care

5.1. MBE Samples

was taken to have the same laser spot size, power density and illumination angle for both samples, it must be noted, that the factor of two in PL intensity is within the possible uncertainty in emission intensity in two separate experiments. Nevertheless, as it was observed in repeated measurements, at least the trend to a higher intensity in the case of sample I17 is given.

The temperature dependent data were fitted with a function of the form [150]

$$I = \frac{I_0}{1 + a \cdot e^{-\frac{E_1}{kT}} + b \cdot e^{-\frac{E_2}{kT}}},$$

where E_1 and E_2 are the activation energies, k is the Boltzman constant and T is the sample temperature.

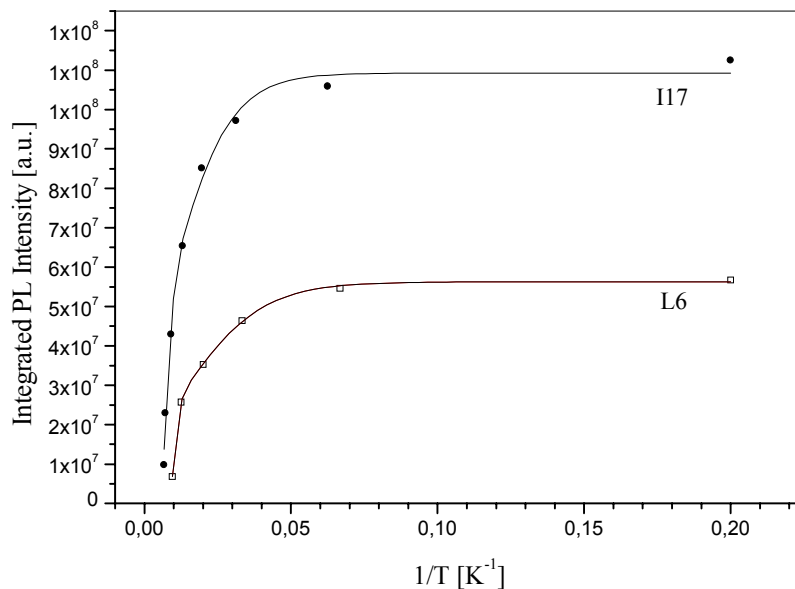


Figure 43: Arrhenius plot of the two MBE grown samples I17 and L6, indicating both a higher luminescence intensity and a higher quenching temperature for the sample I17, which was grown at a higher temperature.

E_1 is found to be ~105 meV for I17 and L6. E_1 reflects the valence band offset in Si/SiGe and agrees well with estimates for 25 % Ge in the MBE samples. E_2 is found to be 13 and 7 meV for the samples I17 and L6, respectively. This activation energy is responsible for the early but slow temperature quenching due to non-radiative carrier recombination. The smaller E_2 the higher the non-radiative defect concentration, leading to a stronger bending of the Arrhenius curve. The parameters 'a' and 'b' determine the exact shape of the curve. The higher the value of parameter 'a' the more the quenching edge is shifted to higher values of $1/T$. This parameter does not influence the slope of the curve. The parameter 'b'

5.1. MBE Samples

is responsible for the curvature of the quenching edge, the higher 'b' the tighter the curvature. From the fitting we obtain a parameter 'a' of 8726 and 24955 for the samples I17 and L6, respectively, with an uncertainty of 10%. The parameter 'b' turns out to be 1.1 and 1.9, also with an uncertainty of 10%.

The factor of two in the PL intensity of the MBE samples when increasing the growth temperature from 600 to 650 °C does not seem to be caused by the Ge clustering as reported in [10]. Instead, the PL increase seems to originate from a smaller concentration of non-radiative traps. Our data, as well as that of Miyao et al. [10], are consistent with this interpretation, since the increased PL yield at growth temperatures above 600 °C may easily be explained by a reduction of point defects during growth. Point defects are generally produced during Sb-assisted MBE growth, since Sb decreases the surface diffusion length of Si.

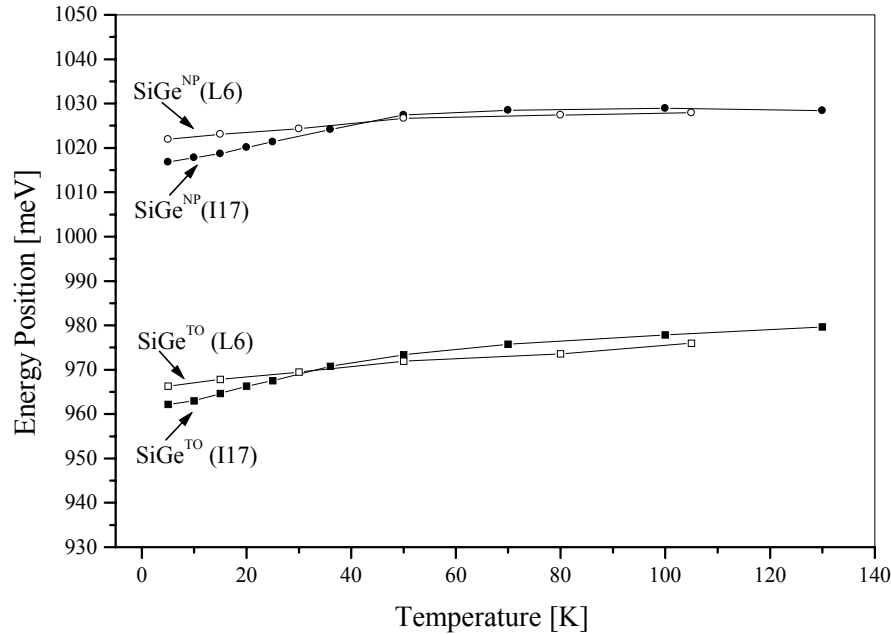


Figure 44: Energy position of the SiGe^{NP} and SiGe^{TO} lines as a function of the sample temperature. At higher temperatures the two lines were not resolved.

Figure 44 shows the energies of the SiGe^{NP} and SiGe^{TO} lines for the samples I17 and L6. As the SiGe layers are strained in these samples both, the no-phonon and the transverse optical phonon assisted transitions, are slightly shifted to higher energies with increasing sample temperature. In unstrained SiGe alloys the fundamental bandgap decreases with temperature leading to a shift to lower energies with increasing temperature [151].

5.1. MBE Samples

5.1.1.2. Power Dependence

To identify the PL peaks in more detail, additionally power dependent spectra were recorded.

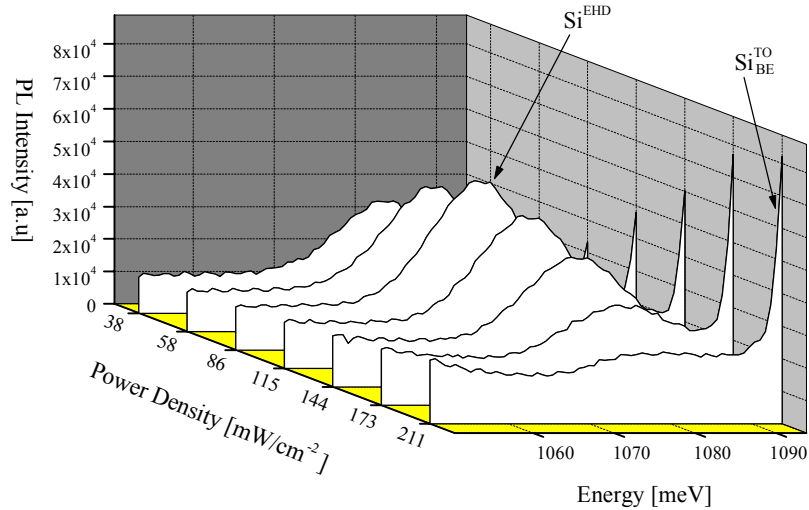


Figure 45: PL Spectra of sample an MBE grown sample (I17) recorded at 4.2K at different laser excitation power densities.

Figure 45 shows EHD emission of an MBE grown Si/SiGe multiple quantum well sample at 4.2 K and at different excitation power densities. At low and medium excitation densities of up to about 86 mW/cm^2 the EHD intensity increases as discussed above. At further increase of the laser power density the EHD emission decreases strongly and vanishes at high power densities of more than about 200 mW/cm^2 nearly completely.

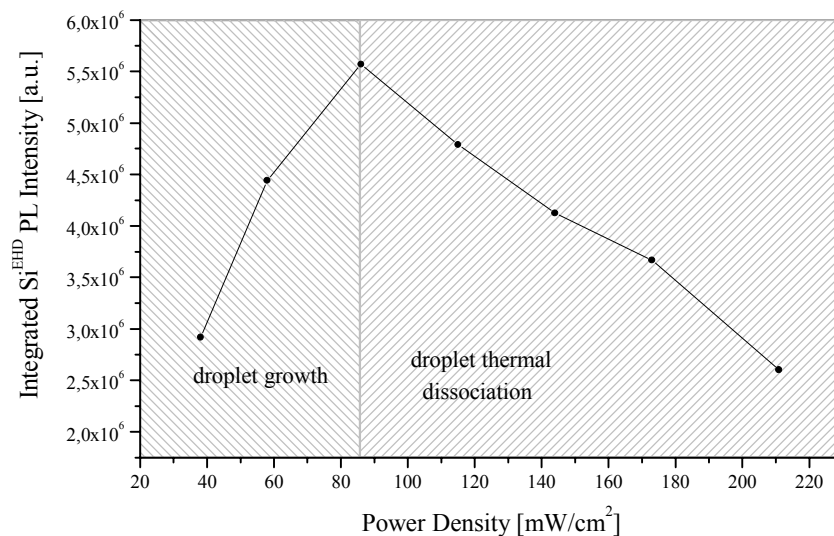


Figure 46: Integrated Si^{EHD} PL Intensity showing an increase of the intensity with laser excitation power density before the electron hole droplet dissociates as the sample heats up with further increase in power density.

5.1. MBE Samples

This is because the sample is heated up at higher power densities leading to a dissociation of the droplet and thus to a decrease in its intensity. Figure 46 clearly shows the dissociation of the droplet.

Figure 47 exemplarily shows the development of the PL signal with excitation power for sample I17.

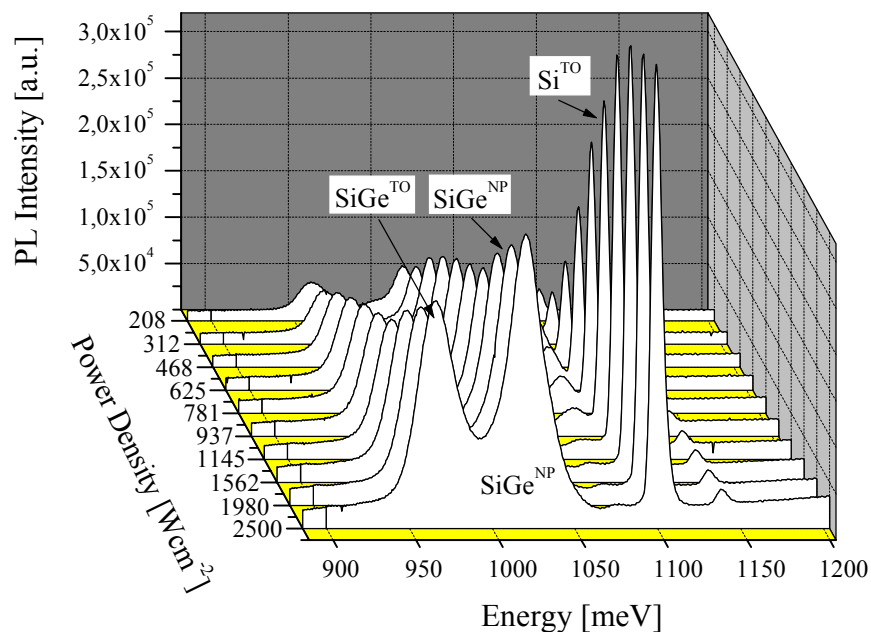


Figure 47: Power dependence of PL spectra of sample I17 at 4.2 K. The intensities are not normalised.

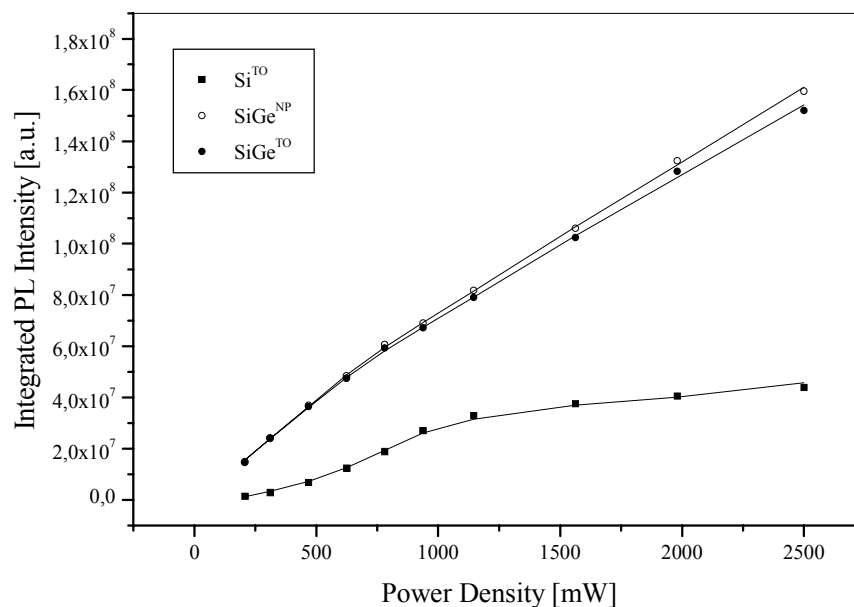


Figure 48: Integrated 4.2 K PL intensity of spectra shown in Figure 47, indicating a clear saturation of the Si^{TO} peak in contrast to the two SiGe lines.

5.1. MBE Samples

Figure 48 depicts the integrated PL intensity for various luminescence peaks. In contrast to the two SiGe lines, the Si^{TO} emission shows a clear saturation, indicating that the excitons are bound, probably to a donor. From the binding energy of about 5.2 meV (the energy difference between the free and the bound exciton) one can conclude that the saturation results from saturating the Sb donors. This is also underlined by the structural knowledge about the substrate which is indeed Sb-doped.

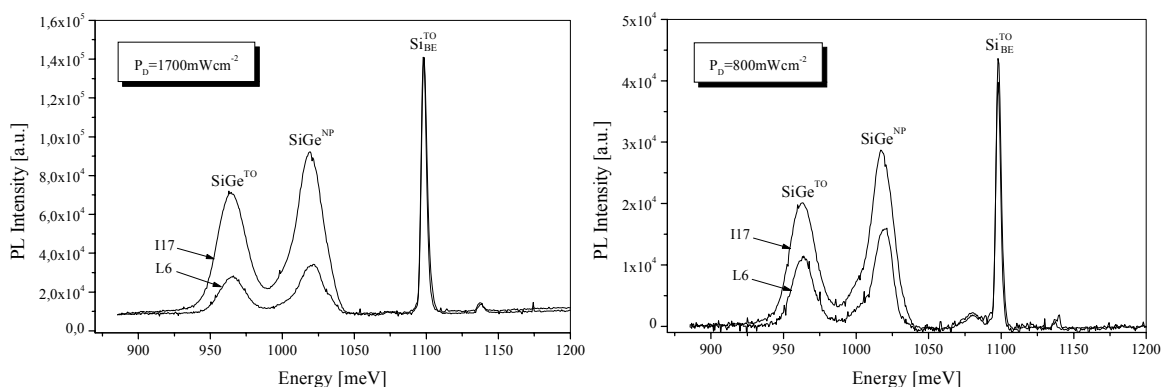


Figure 49: PL intensity of both MBE samples recorded at 1700 mWcm^{-2} (left) and 800 mWcm^{-2} (right).

Figure 49 compares the PL intensity of the MBE sample I17 and L6 at two different excitation power densities. A factor of two in the PL intensity difference between the two samples is observed.

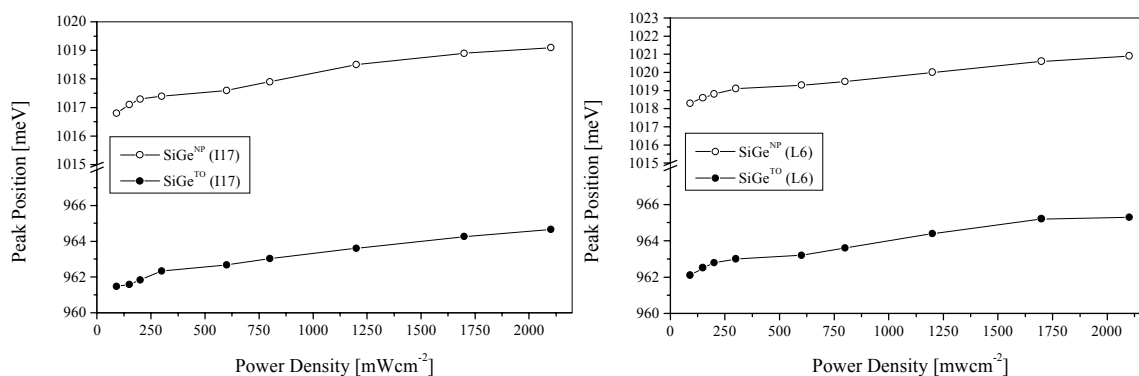


Figure 50: Shift of PL peak energies for sample I17 (left) and L6 (right) at higher excitation power densities.

Both MBE samples show only a slight shift of the SiGe peak positions to higher energies with excitation power densities.

5.1. MBE Samples

5.1.2. Phonon Spectrum

Raman spectra were recorded to back-up the results concerning the identical Ge composition between the two MBE samples from photoluminescence and x-ray analysis. Figure 51 shows the micro Raman spectra of both MBE samples recorded at room temperature at an excitation power of 23 mW. The laser spot size was about 2-3 μm in diameter, the x100 objective of the microscope was used.

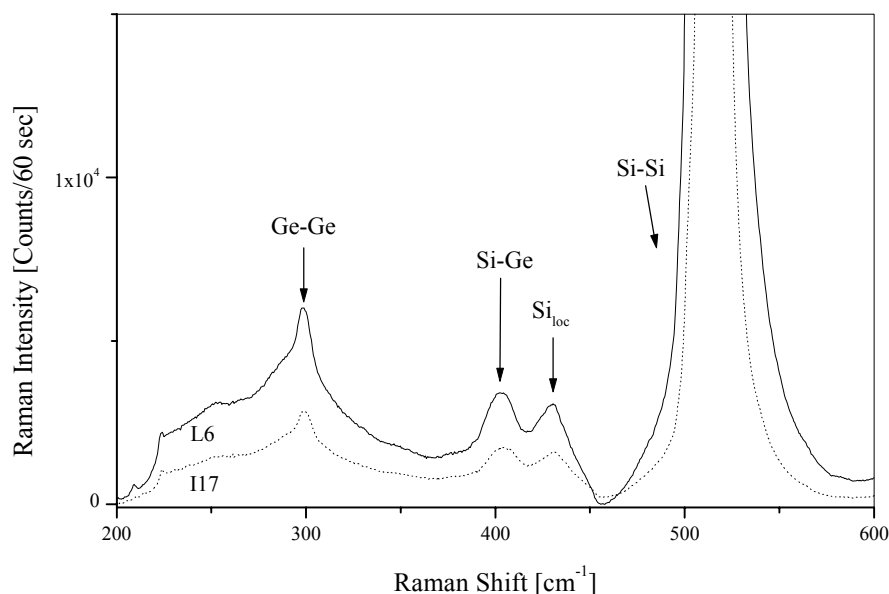


Figure 51: Raman spectra of the two MBE samples recorded with the 514.5 nm line of an Ar^+ ion laser. Raman frequencies resulting from Ge-Ge, Si-Ge and Si-Si modes are indicated. The spectral resolution was 1.5 cm^{-1} .

The absolute intensities of these spectra are not comparable as large discrepancies in the scattered signal can occur due to slight changes in the microscope focus. However, clearly there is no shift of the lines observable between the two samples, within the spectral resolution of these spectra, indicating the same Ge concentration in both samples in accordance to the PL and x-ray data.

5.1.3. Structural Properties

In order to check the relevance of the MQW structure, we characterised the interface and layer quality by x-ray diffraction and reflectivity. To determine the electron density profile at the interfaces the Parratt formalism [131], which takes into account multiple reflections at all the interfaces, was used. Fluctuations of the interface position were taken into

5.1. MBE Samples

account via a Debye-Waller-like damping factor for the reflected intensity [131],[130,152]. The silicon cap was assumed to be covered by a SiO₂ layer.

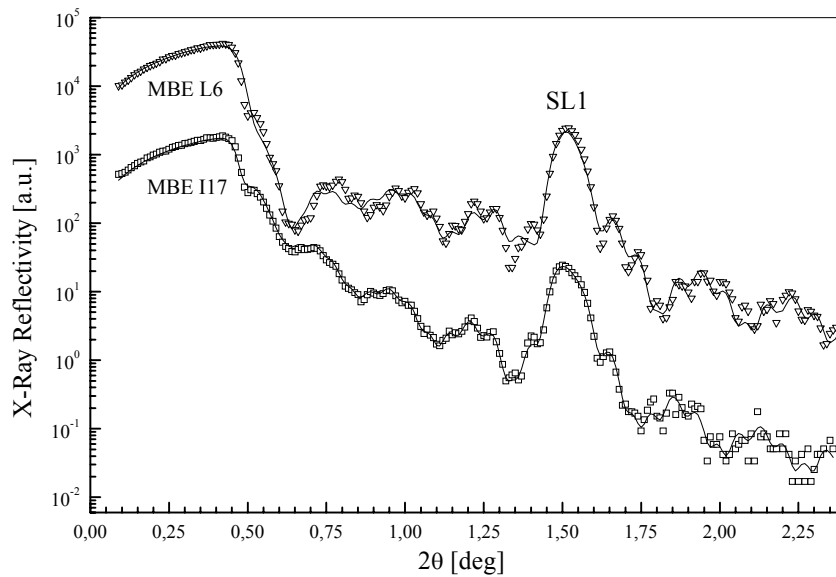


Figure 52 : Fits to the x-ray reflectivity data for both MBE samples.

Sample	d_{SiOx} [Å]	δ_{SiOx} [10^{-5}]	σ_{SiOx} [Å]	$d_{\text{Si-Cap}}$ [Å]	$\delta_{\text{Si-Cap}}$ [10^{-5}]	$\sigma_{\text{Si-Cap}}$ [Å]	d_{SiGe} [Å]	δ_{SiGe} [10^{-5}]	σ_{SiGe} [Å]	d_{Si} [Å]	δ_{Si} [10^{-5}]	σ_{Si} [Å]
L6	83.3	1.07	7.3	233.2	1.65	20.9	29.7	1.93	7.8	31.5	1.59	4.1
I17	23.4	1.01	9.4	307.4	1.52	13.4	30.2	1.86	14.1	31.1	1.60	6.9

Table 2: Values of the different parameter obtained from the fitting to the reflectivity curves of samples L6 and I17.

The data could be fitted very well assuming that all SiGe layers, as well as all Si barriers, are characterised by the same layer thickness, roughness and index of refraction. Thus, the number of free fitting parameters was kept to a minimum.

As the fitting parameters are partly cross-correlated and as the fitting function does not have a closed form, the errors in the parameters are approximated from the width of the χ^2 curves, as indicated for the SiGe well thickness and SiGe well electron density of sample I17 in Figure 53. For the other parameters and for sample L6 similar curves were obtained. For all layer thicknesses d , all electron densities δ and all roughnesses ρ the following uniform errors were determined as a 10% change in the χ^2 :

$$\Delta d = 2 \text{ \AA}, \Delta \delta = 0.1 \cdot 10^{-5}, \Delta \rho = 0.2 \text{ \AA}.$$

5.1. MBE Samples

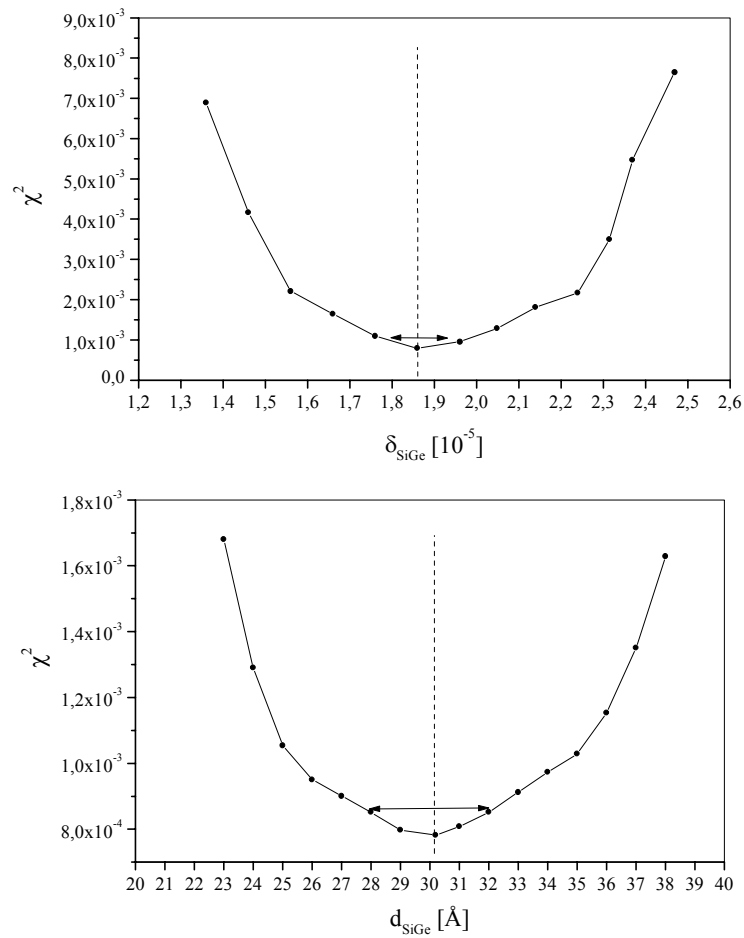


Figure 53: Variation of χ^2 with a change of the SiGe electron density δ (top) and the SiGe quantum well thickness d (bottom).

Table 2 summarises the obtained values for the different parameters from the fitting.

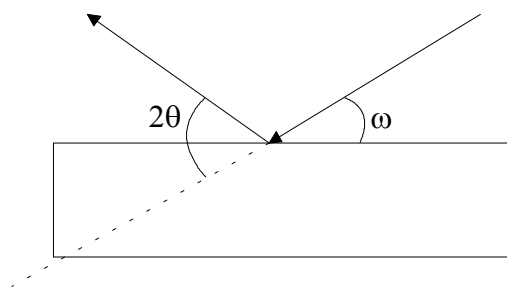


Figure 54: Schematic illustration of the symmetric Bragg reflections SL0 and Si(004) as shown in Figure 55.

Figure 54 schematically shows the symmetric Bragg reflections leading to the SL0 and Si(004) diffraction observed in x-ray diffraction.

With

$$2 \cdot d \cdot \sin \theta = n \cdot \lambda$$

5.1. MBE Samples

one obtains $2\theta = 1.44236^\circ$ for sample L6 and $2\theta = 1.44000^\circ$ for sample I17, where d is the period length of the multiple quantum well structure (L6: $d=61.2 \text{ \AA}$, I17: $d=61.3 \text{ \AA}$).

The reflectivity data and their fitting curves are shown in Figure 52. For both MBE samples the roughness of the SiGe/Si interfaces is found to be about twice that of the Si/SiGe interfaces. The formation of rather rough SiGe surfaces can be attributed to the minimisation of the total elastic energy [75]. For sample I17 grown at 650°C our data reveal a pronounced increase of the roughness of both interface types by about a factor of two compared to sample L6. Whereas sample L6 has a Si/SiGe interface roughness of 4.1 \AA and a SiGe/Si roughness of 7.8 \AA , the corresponding results for sample I17 were 6.9 \AA for the Si/SiGe and 14.1 \AA for the SiGe/Si interfaces, with an error of about 10%, respectively.

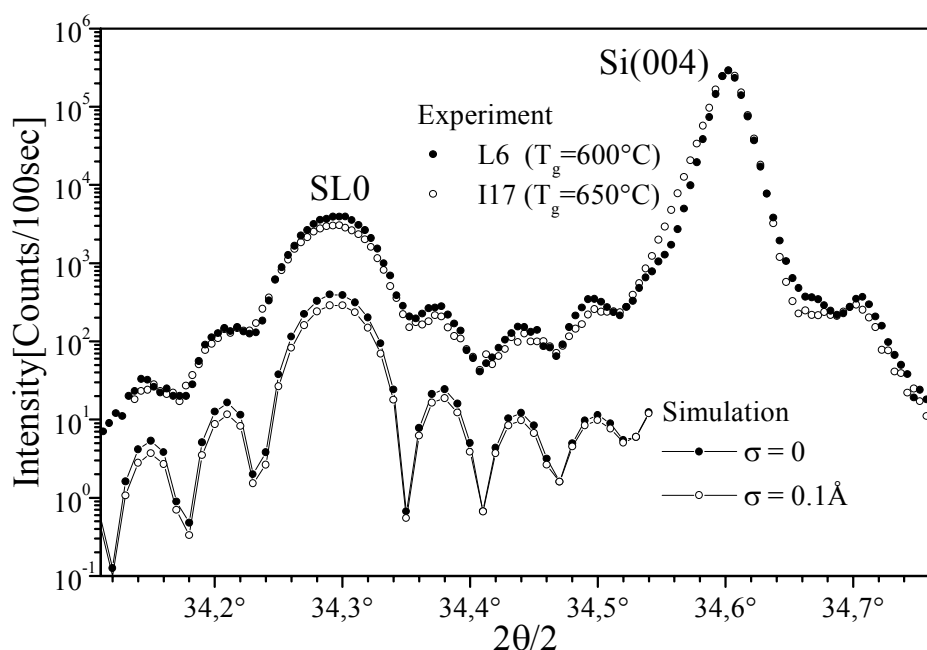


Figure 55: X-ray superlattice diffraction at higher angles. The Bragg reflection from the substrate is also seen. Note that the data from the RTCVD sample and the fitting-curves are shifted along the intensity axis for convenience.

Fluctuations of the atoms in the SiGe layers of sample L6 lead to a pronounced damping of the SL0 reflection by 25% compared to sample I17.

For the Si (001) substrate with a lattice constant $a=5.43105 \text{ \AA}$ one obtains $\omega = 34.56428^\circ$ and $2\theta = 69.12856^\circ$ as theoretical values.

The superlattice reflections of sample I17 obtained in the conventional θ - 2θ geometry at higher angles are damped by 25% as compared to sample L6.

5.1. MBE Samples

However, simulations revealed, that the SL0 peak is not influenced by interface roughness. To consider the influence of the crystalline quality, diffraction data were simulated taking into account static atomic displacements around ideal lattice positions in the SiGe layers via a Debye-Waller factor $e^{-\langle u^2 \rangle q^2}$. q is the momentum transfer $k_f - k_i$, with k_i being the initial and k_f the final wave vector. Based on a simple diffraction law a formalism has been developed to take into account this effect mathematically to simulate the superlattice reflections.

The diffracted intensity I is given by

$$I(\theta, N, \sigma, dwf, fold) = \sum_{m=-fold}^{m=+fold} \left(|F(\theta + m \cdot resolution, N, \sigma, dwf)|^2 \right)$$

with

θ = the angle of diffraction

N = number of multilayer

σ = the interface roughness

dwf = Debye-Waller factor

$fold$ = starting and finishing angle for gaussian like folding function

m = integration parameter

$resolution$ = the experimental resolution in $q = 0.002$.

The structure factor F is given by

$$F(\theta, N, \sigma, dwf) = \sum_{n=0}^{N-1} f(q(\theta), n, \sigma, dwf) + f_{Si} \cdot P_{Si} + f_{SiGe} \cdot P_{SiGe}$$

with

$$f(q(\theta), n, \sigma, dwf) = [f_1 + f_2 + f_3 + e^{i \cdot q \cdot a_{SiGe} \cdot 22} \cdot (f_4 + f_5 + f_6)] \cdot e^{i \cdot n \cdot (22 \cdot a_{Si} + 22 \cdot a_{SiGe}) \cdot q},$$

$f_{Si} = 14$ = form factor (=the sum of all electrons of the species),

$$P_{Si} = \frac{1 - e^{-i \cdot d_{buf} \cdot a_{Si} \cdot q(\theta)}}{1 - e^{-i \cdot a_{Si} \cdot q(\theta)}} \cdot e^{-i \cdot a_{Si} \cdot q(\theta)},$$

$$P_{SiGe} = \frac{e^{-i \cdot (N \cdot (d_{Si} \cdot a_{Si} + d_{SiGe} \cdot a_{SiGe})) \cdot q(\theta)}}{1 - e^{-i \cdot a_{Si} \cdot q(\theta)}},$$

d_{buf} = number of Si monolayers in the Si buffer layer (= 309)

d_{Si} = number of Si monolayers in the barrier layers (= 22),

d_{SiGe} = number of SiGe monolayers in the quantum well layers (= 22),

5.1. MBE Samples

$$f_1 = f(\sigma) \cdot \left(\sum_{m=0}^{\sigma-1} e^{i a_{\text{SiGe}} \cdot q \cdot m} \right),$$

$$f_2 = dwf \cdot f_{\text{SiGe}} \cdot \left(\sum_{m=\sigma}^{21-\sigma} e^{i a_{\text{SiGe}} \cdot q \cdot m} \right),$$

$$f_3 = f(\sigma) \cdot \left(\sum_{m=21-(\sigma-1)}^{21} e^{i a_{\text{SiGe}} \cdot q \cdot m} \right),$$

$$f_4 = f(\sigma) \cdot \left(\sum_{m=0}^{\sigma-1} e^{i a_{\text{Si}} \cdot q \cdot m} \right),$$

$$f_5 = f_{\text{Si}} \cdot \left(\sum_{m=\sigma}^{21-\sigma} e^{i a_{\text{Si}} \cdot q \cdot m} \right),$$

$$f_6 = f(\sigma) \cdot \left(\sum_{m=21-(\sigma-1)}^{21} e^{i a_{\text{Si}} \cdot q \cdot m} \right).$$

The differences in the diffraction data obtained from the MBE samples grown at 600 °C and 650 °C, can be reproduced assuming an increase of the mean-square displacement $\sqrt{\langle u^2 \rangle}$ of 0.1 Å, which is about 7% of the SiGe lattice parameter.

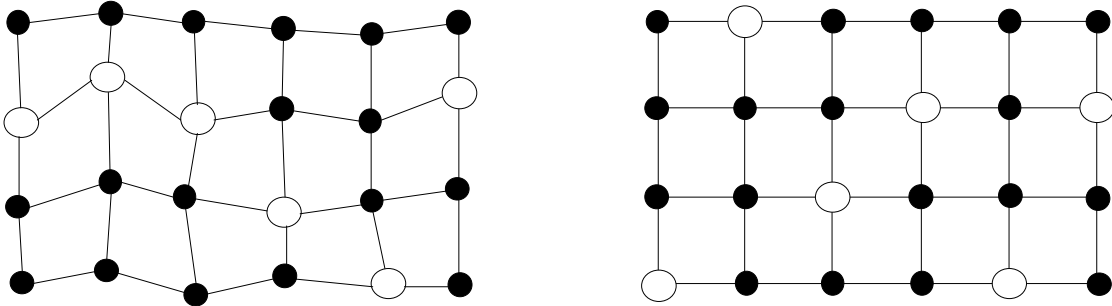


Figure 56: Schematic model of atomic displacements expected in the case of a higher growth temperature (left). For simplicity the resulting structure grown at lower temperature is drawn as an ideal lattice (right).

The static displacements within the SiGe layers are apparently caused by Ge concentration fluctuations, which are expected to be more pronounced at higher growth temperature. However, neither the inhomogeneities nor the increased interface roughness seem to act as localisation centres for excitons, since the ratio of NP to TO replicas is 1.5 for both samples. Moreover, no strong blue-shift of the NP peak position is detectable over the investigated excitation power range. If the k -conservation rule for exciton recombination were broken due to interface roughness and/or inhomogeneities an increase in the NP-line intensity would be expected.

5.2. RTCVD Samples

Two of the wafers used in this thesis were grown by rapid thermal CVD (RTCVD) in the Epsilon One reactor of Advanced Semiconductor Materials (ASM). Both wafers had the same structure and growth parameters and only differed in the doping level of the substrate. In the following they are called n-i-p⁺ and n⁺-i-p⁺ RTCVD samples. On an 80 nm undoped Si buffer grown at 700 °C on Si(001) a 15 period Si/Si_{0.77}Ge_{0.23} (4.1 nm/3.9 nm) quantum well structure was deposited at 625 °C. After an additional 10 nm Si top layer grown at 625 °C a cap layer of 30 nm n⁺-Si (P doped) was grown at 700°C. The gases used were electronic grade, the hydrogen was supplied from a liquid source entering the reactor via a Nanochem purifier. The depositions were carried out at atmospheric pressure. For both samples the Si and SiGe layers were grown from SiCl₂H₂ and GeH₄ in a H₂ on a Czochralski (100) n-substrate (Sb-doped, 20-30 Ωcm) in the case of the n-i-p⁺ and on Czochralski (100) n⁺-substrate (Sb-doped, .006 -.010 Ωcm). The use of SiCl₂H₂ as a process gas has the advantage that at adequate growth conditions a selective growth is possible without addition of HCl. In contrast to SiCl₄ Si Cl₂H₂ is in gasform at room temperature, enabling an easy storage and supply to the reactor. A deposition using SiCl₄ or SiCl₃H as a process gas is only possible at higher growth temperatures due to the higher stability of SiCl₄ and SiCl₃H₂ molecules. In comparison with SiH₄ the epitaxy using SiCl₂H₂ enables the deposition of pure layers at low temperatures (less C- and O-contamination in the epitaxial layer) [153]. Furthermore SiCl₂H₂ is less toxic than SiH₄ [153].

Prior to growth the wafers were subjected to a 3 min H₂ bake at 1190°C to remove the native oxide. The Si layers were grown using 20 slm H₂ and 20 sccm SiH₂Cl₂, the SiGe layers were grown by adding 0.2 scm GeH₄ to the gas flow, respectively.

We distinguish three types of samples:

- (1) as grown Si/SiGe MQW.
- (2) different chips of the same sample as is (1) but annealed at temperatures between 200 and 500°C for 10 min in an Ar atmosphere in contact with steel.
- (3) different chips of the same sample as is (1) but annealed in ultra high vacuum at temperatures up to 750 °C avoiding contact to a metal.

For these three sample types we performed structural and luminescence characterisation. To confirm certain results we additionally kept one chip of sample (1) for six months at room temperature and repeated the photoluminescence characterisation.

5.2. RTCVD Samples

5.2.1. Emission Spectrum

5.2.1.1. Temperature Dependence

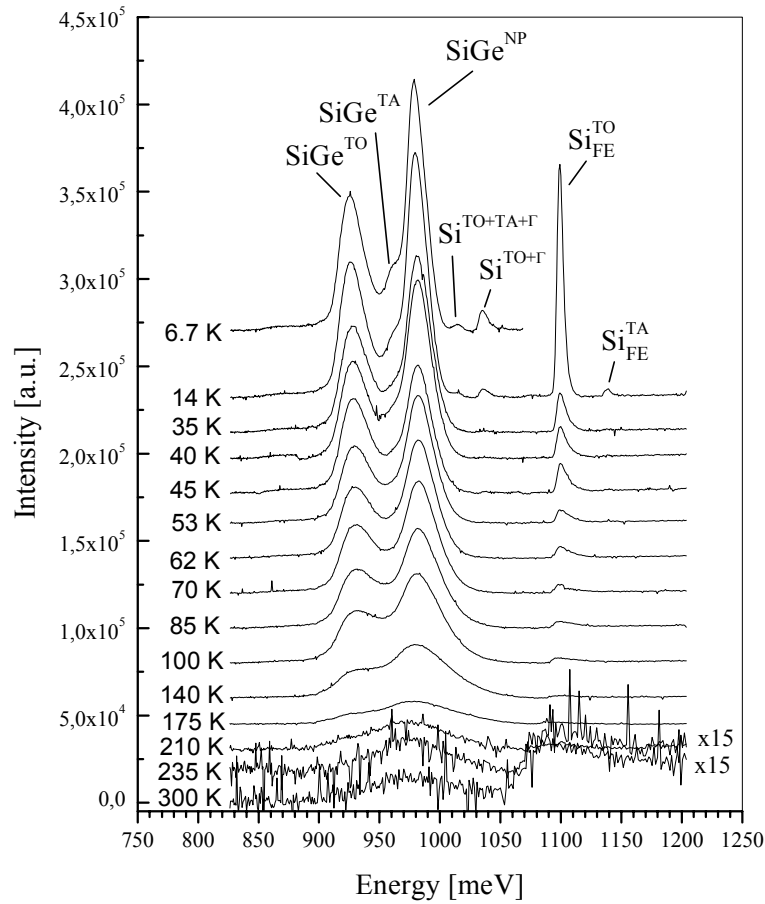


Figure 57: Temperature dependent PL spectra of the “RTCVD” sample showing luminescence up to room temperature.

Figure 57 shows temperature dependent PL spectra obtained from the RTCVD sample at an excitation power density of 2122 mW/cm^2 . In the 6.7 K luminescence spectrum (uppermost spectrum in Fig. 2) the lines labelled SiGe^{NP} and SiGe^{TO} correspond to the SiGe no-phonon and the transverse optical phonon-assisted emission, respectively. Between these two lines the transverse acoustic phonon-assisted emission is observed (SiGe^{TA}). At 1035 and 1015 meV, multiple phonon-assisted emissions ($\text{Si}^{\text{TO}+\Gamma}$ and $\text{Si}^{\text{TO}+\text{TA}+\Gamma}$) from the Si substrate are also observed. The strong emission at 1099 meV is due to the transverse optical phonon-assisted free exciton recombination ($\text{Si}^{\text{TO}}_{\text{FE}}$) from the Si substrate. On the high energy side, the Si transverse acoustic phonon-assisted free exciton emission line ($\text{Si}^{\text{TA}}_{\text{FE}}$) is observed. The SiGe luminescence can be detected up to room temperature, although at room temperature the emission spectrum is dominated by free

5.2. RTCVD Samples

carrier band-to-band (B-B) transitions in Si. The intensity of the B-B band centred at ~ 1099 meV increases with temperature. This effect, also observed in the MBE samples [22], can be explained by a transition from excitonic to free carrier recombination. The data in Figure 58 to show the temperature quenching of the RTCVD sample, is shown in an Arrhenius plot with a resulting activation energy $E_1=118$ eV.

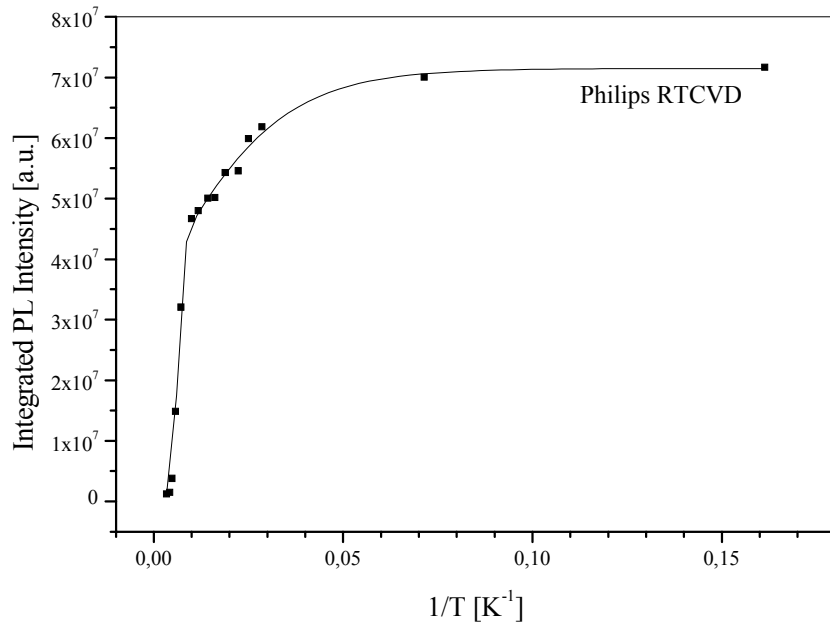


Figure 58: Arrhenius plot of the RTCVD sample.

As will be shown later in section 5.2.2.2 the quantum wells were at the very limit of maximum strain. Annealing the sample moderately at only 200 °C for 10 min already leads to an enhancement of dislocation lines (D1-D4) in the PL spectrum. It seems as if strong lateral undulations of either the Ge concentration or the strain field had formed at the SiGe/Si interfaces during the annealing. These potential fluctuations could lead to an effective localisation of excitons at the SiGe/Si interface. However, as the measured specular x-ray reflectivity (discussed in section 3.5) is only sensitive to the projection of the electron density onto the growth direction, we can only judge on the average roughness, but not on the lateral length scale of the potential fluctuations. The obtained Si and SiGe layer thicknesses for all samples are in very good agreement with the nominal values, showing deviations of only ± 0.1 nm.

5.2. RTCVD Samples

5.2.1.2. Power Dependence

Figure 59 shows the power dependence of the PL spectrum recorded at 6 K under an excitation power varying between between 150 and 2120 mWcm^{-2} . The clear blue-shift of the SiGe^{NP} line as well as the asymmetric line broadening can be attributed to exciton localisation at the strong potential fluctuations of the SiGe/Si interfaces [154,155]. Note that the intrinsic Si bulk recombination energy does not shift with power.

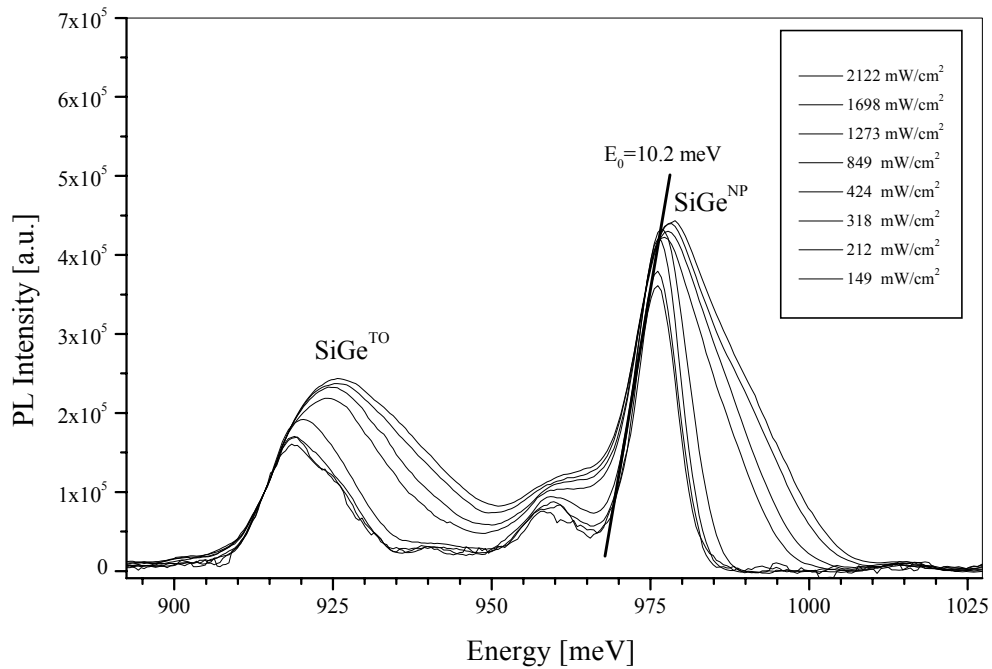


Figure 59: Power dependent PL spectra of the RTCVD sample recorded at 6 K. Spectra are normalised to the low energy tail of the SiGe^{NP} line.

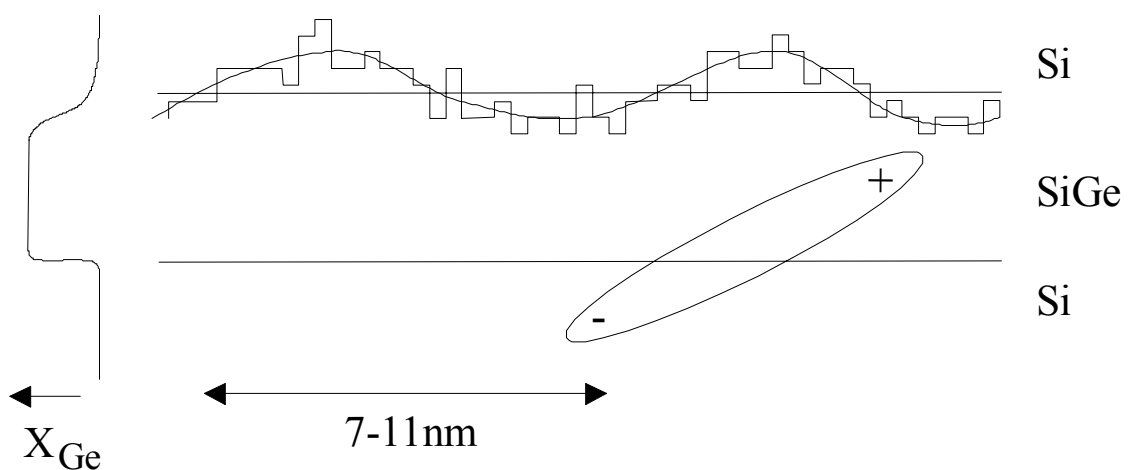


Figure 60: Lateral undulation of the valence band along the SiGe/Si interface leading to an effective localisation of excitons.

5.2. RTCVD Samples

The origin of the blue-shift is expected to be due localisation of excitons at SiGe interface potential fluctuations due to strong interdiffusion.

This is because the substrate temperature was increased to 700 °C to grow the 40 nm cap layer. At higher laser excitation density more excitons are generated so that all localised states get saturated and additional excitons recombine without this localisation effect. This is why the energy shift is higher for the RTCVD sample than for the MBE sample.

The low energy tail is found to decrease exponentially following an $\exp(E/E_0)$ expression, with a slope $E_0=10.2 \pm 1.0$ meV. Beside the blue-shift, the asymmetric line shape, the saturation of the integrated SiGe intensity with excitation power density and the relative sharp high-energy edge at lower excitation power, as shown in Figure 59 are attributed to the localised exciton model [104,156].

Figure 61 shows the spectral energies of the SiGe^{NP} and SiGe^{TO} lines against the excitation power density. With increasing power the SiGe^{NP} line shifts by about 2-3 meV in the excitation range used and the SiGe^{TO} line shifts by about 8-9 meV to higher energies.

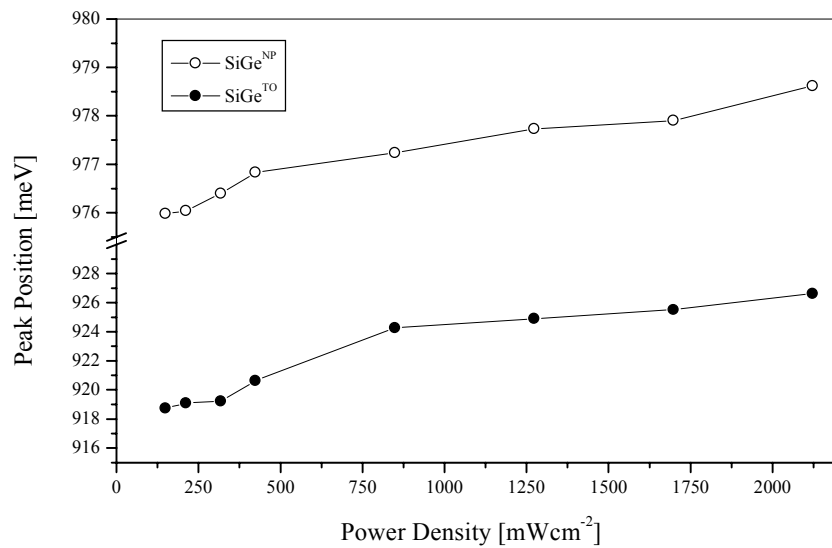


Figure 61: Shift of SiGe emission lines (NP and TO replicas) as a function of laser power at 6K. Note, that the energy axis is broken and that the scales are different.

5.2. RTCVD Samples

5.2.1.3. RTCVD Samples annealed in Metallic Contamination Conditions

The required activation energy for the formation of misfit dislocations can be reduced significantly by the presence of defects within the layer. Dislocations in silicon show characteristic photoluminescence, observed by Drozdov et al. [157]. It is composed of 4 lines denoted D1, D2, D3 and D4. The energetic position of these peaks are summarised from the work of several authors in Table 3.

	Pure Si (Drozdov et al.)	Pure Si (Sauer et al.)	Si/SiGe (Lee and Choi)	Si/SiGe MQW (this work)
D1 [meV]	812	807	800	808
D2 [meV]	875	839	870	878
D3 [meV]	934	874	920	/
D4 [meV]	1000	997	994	/

Table 3: Energetic position of the four different D-lines recorded for pure Si [157,158], for a thin SiGe layer on Si [159] and for a SiGe/Si MQW structure examined in this work.

This suggests that dislocations accompany some deep levels which act as radiative recombination centers. Various characteristics of this luminescence such as the dependence of the luminescence intensity on the sample temperature [160], the dependence of the spectrum on the dominant type of dislocations [161], thermal stability of the defect giving rise to luminescence [162] or the effect of uniaxial stress on the peak energy [158] have been studied so far.

Suezawa and Sumino confirmed in a high temperature experiment that dislocations themselves are active as recombination centres [160,162,163]. They concluded that dangling bonds at the dislocation core are not responsible for the recombination process but rather that reconstructed bonds or severe distortion at the dislocation core contribute to the radiative recombination processes. They also suggested that D1 and D2 lines originate from geometrical kinks at dislocations.

Sauer et al. [161] suggested rather straight dislocations lying parallel to the $\langle 110 \rangle$ direction by deformation at a low temperature under high stress. Besides D1-D4 they discovered D12, D5 and D6 lines. They studied the thermal stability of these lines and the dependence of their energy positions on the uniaxial stress. They concluded that the defects giving rise to D3, D4, D5 and D6 lines are closely related to each other, whereas those giving rise to the D1 and D2 lines might be deformation-induced point defects in the

5.2. RTCVD Samples

vicinity of dislocations. They later concluded that the D3, D4 and D5 lines originate from the radiative recombination at the dissociated glide deformations [158].

There have been a few studies on the correlation of the photoluminescence spectrum with the dislocation configuration or type of dislocation. Weronek et al. [164] concluded that D3 was a TO phonon replica of D4 and that D1 was an 0^F phonon replica of D2. Higgs et al. [165] obtained cathodoluminescence images of slip lines in a plastically deformed specimen and found that the D3 and D4 lines were strong along slip lines, whereas the D1 and D2 lines were predominant in the regions between the slip lines. They attributed the D1 and D2 lines to impurities incorporated at the dislocation core. Higgs and Lightowlers reported that the D line luminescence is correlated with the metallic impurities [166,167]. They introduced dislocations into a silicon crystal under contamination-free conditions, and then contaminated the specimens with Cu, Ni and Fe at different levels of contamination. They investigated the luminescence in such specimens and found that only low-level contamination of such impurities enhances D1 and D2 luminescence significantly in the same way. They concluded that metallic impurities in the strain field of dislocations were the cause of D1 and D2 luminescence.

However, it is still under debate whether a metallic decoration is indeed needed for radiative recombination at misfit dislocations. Therefore different chips of the same Si/SiGe multiple quantum well wafer were annealed with and without a metallic contamination to bring some further inside into this point.

In this work we have observed D-line luminescence in PL experiments of highly strained Si/SiGe MQW samples, which have been moderately annealed at temperatures between 200 and 500 °C.

5.2. RTCVD Samples

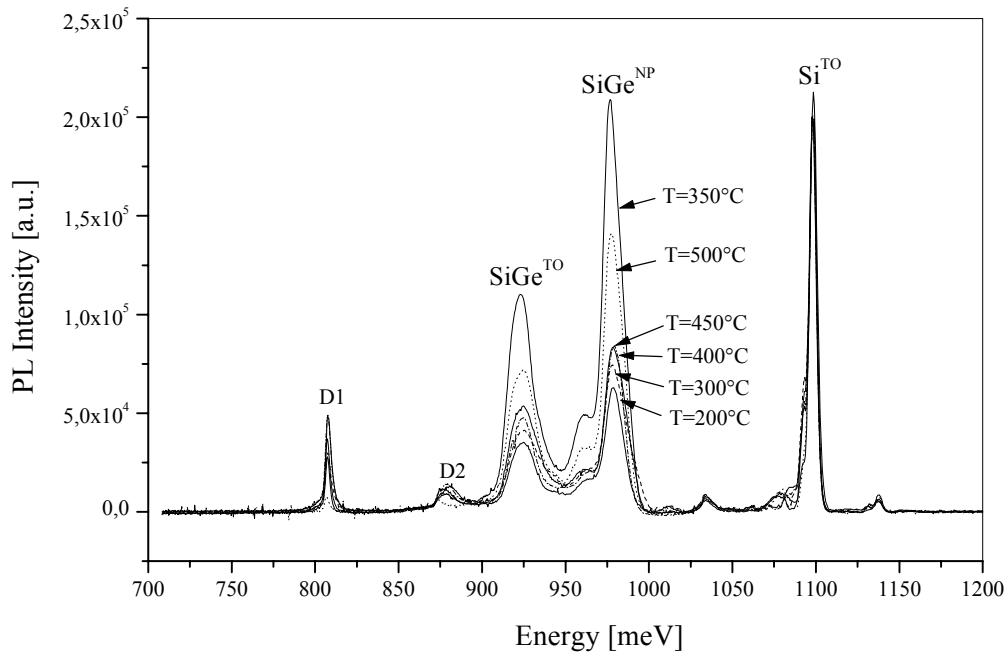


Figure 62: PL spectra of the n-i-p⁺ RTCVD samples annealed at various temperatures with the surface in direct contact to the metallic strip annealer.

The annealing was performed in a home-made strip annealer in an Ar atmosphere. Inside the strip annealer the samples were placed on a metal strip made of stainless steel. All samples were annealed for 10 min under the same conditions. The sample annealed at 200 °C shows strong D line emission. This is quite astonishing as the samples themselves were grown at 625 °C.

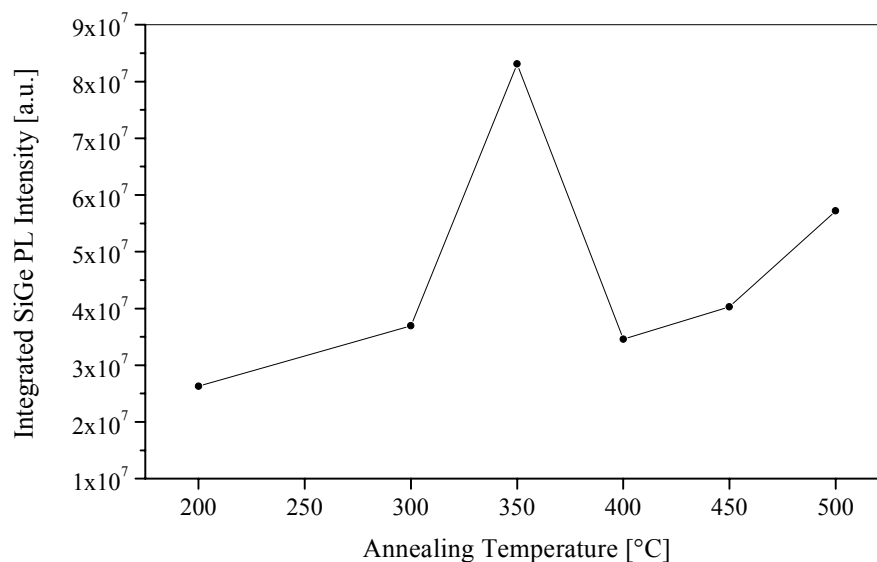


Figure 63: Integrated SiGe^{NP} PL intensity as a function of annealing temperature.

Figure 63 shows the competing process between different radiative channels present inside the samples. We attribute the emergence of these emission lines, usually interpreted as dis-

5.2. RTCVD Samples

location lines, to the presence of strong Ge-concentration fluctuations after annealing. This interpretation is supported by the fact, that no misfit dislocation related emission was visible in the as-grown samples. The D-lines were seen to quench strongly after annealing at higher temperatures, supporting this explanation (see Figure 68). The strain incorporated within the MQW structure is sufficiently large for the sample to show a certain degree of relaxation in the form of T-band emission [113,114] over a period of six months at room temperature (see Figure 64 right).

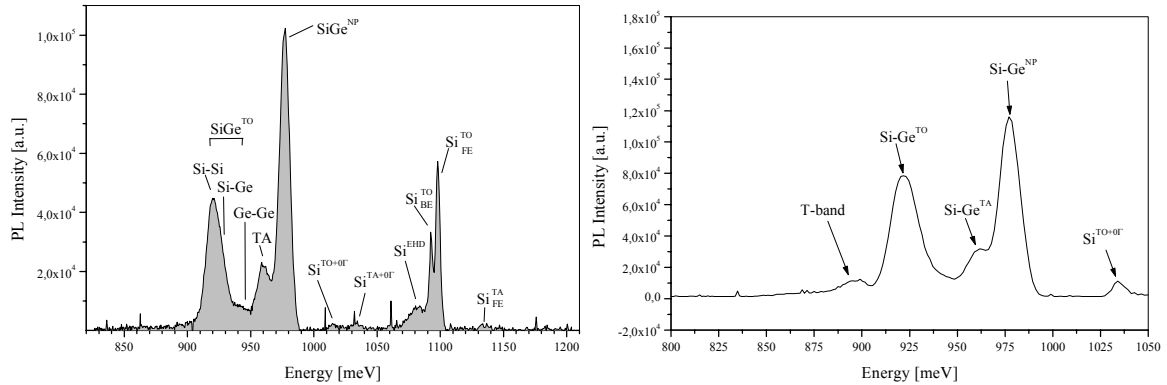


Figure 64: PL spectrum of the as-grown sample recorded at 6K only a few days after growth (left) and six months later recorded at 19K.

In contrast to the PL of the as-grown sample, the spectrum recorded six months later exhibits a bump on the low energy side of the SiGe^{TO} peak, corresponding approximately to the T-band line. This observation indicates that the sample is in a highly metastable state. Thus, an annealing temperature of only 200°C could already lead to the formation of misfit dislocations. To estimate the dependence of radiative transitions at misfit dislocations on a metallic decoration, we have also performed annealing experiments keeping the sample in a contamination-free high vacuum environment. In this case no D1 emission was detected, although the annealing temperature was varied over a wider range. We believe that Fe atoms in the strain field of the dislocations are responsible for the D1 emission, as also reported by Higgs and Lightowlers [67,166,167]. As shown in Figure 62 PL spectra of samples annealed at six different temperatures in contact with stainless steel shortly after the growth of the wafer show clearly D1 and D2 luminescence bands.

5.2. RTCVD Samples

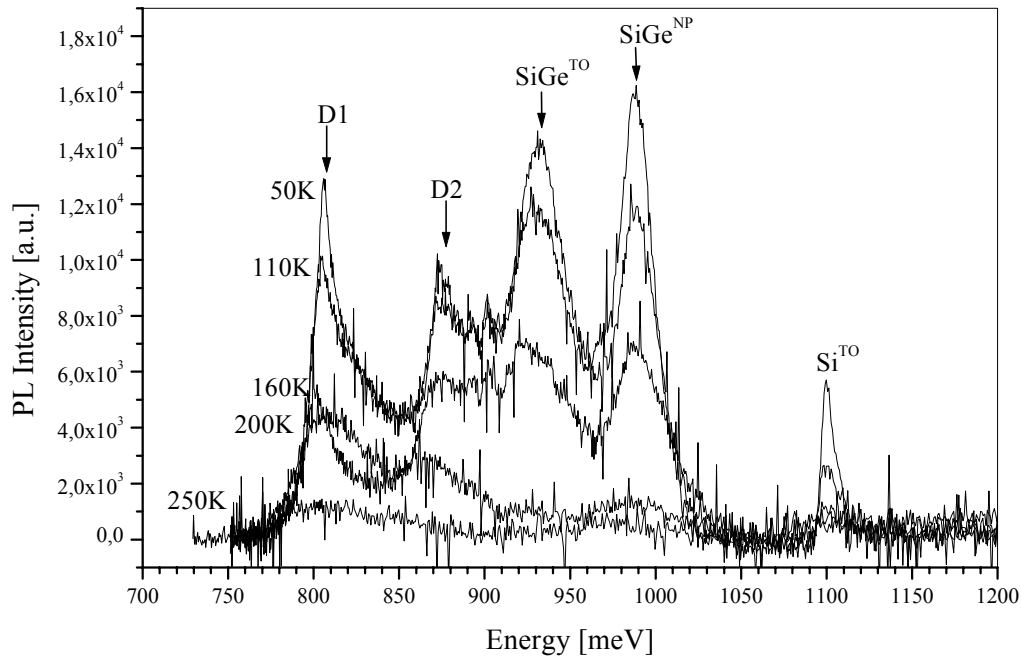


Figure 65: Temperature dependence of the PL spectrum of the p-i-n⁺ RTCVD sample annealed for 15 min at 200°C in direct contact to a metallic strip annealer. For convenience only spectra recorded in the temperature range between 50 and 250 K is shown. No luminescence was detectable at room temperature.

As indicated in Figure 63 the SiGe related intensity strongly depends on the annealing temperature. The highest integrated intensity is observed for an annealing temperature of 350°C. However, this is still lower than the SiGe emission of the as-grown sample. We attribute this effect to competing recombination channels present in the annealed samples, one via the dislocations and the other in the SiGe wells. The higher the dislocation intensity the lower the quantum well recombination and vice versa. After the sample is annealed at 350°C obviously the bandedge luminescence wins over the dislocation related process. Moreover, a drastic modification of the structural properties of the annealed samples with the annealing temperature is clearly visible in x-ray topographs (see 5.2.2.3).

5.2. RTCVD Samples

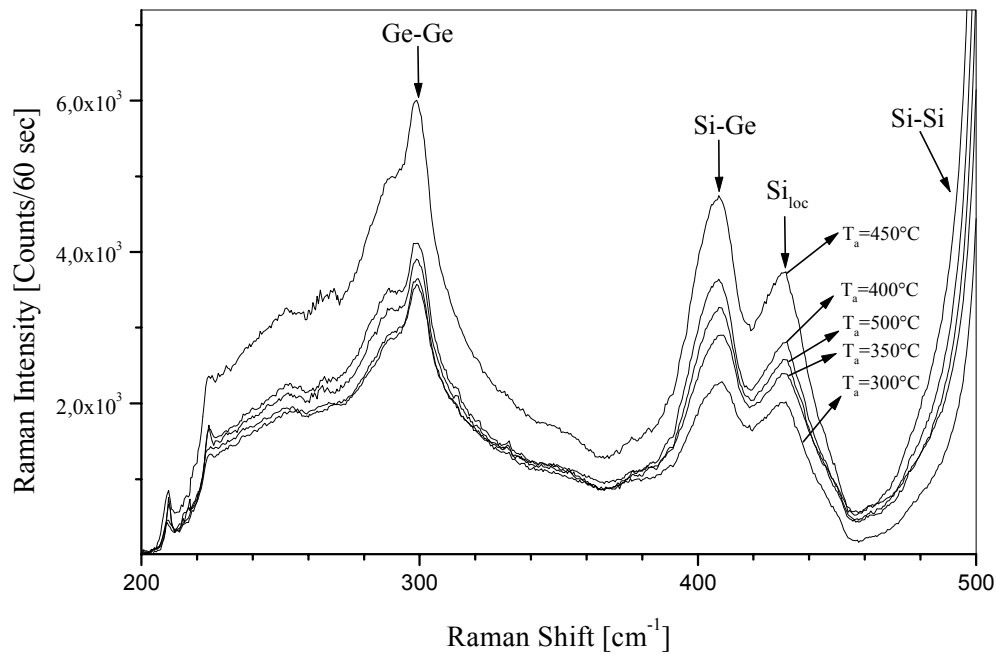


Figure 66: Raman spectra of the six n-i-p⁺ samples annealed under a metallic contamination. The spectra are recorded with the 514.5 nm line of an Ar⁺ ion laser. Raman frequencies resulting from Ge-Ge, Si-Ge and Si-Si modes are indicated.

Figure 66 shows the Raman spectra of the six n-i-p⁺ samples annealed under a metallic contamination. The spectra are recorded with the 514.5 nm line of an Ar⁺ ion laser. Raman frequencies resulting from Ge-Ge, Si-Ge and Si-Si modes are indicated. As in the case of the MBE samples, changes in the absolute Raman intensity are not significant. As the lines do not shift, one can neglect significant changes in the Ge concentration between the differently high annealed samples.

However, in the case of interdiffusion at these annealing temperatures one would expect a modification of the relative intensities between the different peak. Even if interdiffusion would occur on a relative small volume, the very small laser spot of about 2 μm would resolve such Ge concentration changes.

Figure 67 shows the integrated intensity ratios $I_{\text{Si-loc}}/I_{\text{Si-Ge}}$ and $I_{\text{Ge-Ge}}/I_{\text{Si-Ge}}$ and $I_{\text{Si-loc}}/I_{\text{Ge-Ge}}$ for the different annealing temperatures. These ratios were chosen as they represent all possible permutation for these spectra. The higher the intensity of the Si-Si, Si-Ge and Ge-Ge peaks, the more next neighbours of the certain type exist. Thus, an increase of $I_{\text{Ge-Ge}}/I_{\text{Si-Ge}}$ would indicate more Ge next neighbours than Si ones, indicating the formation of Ge clusters.

5.2. RTCVD Samples

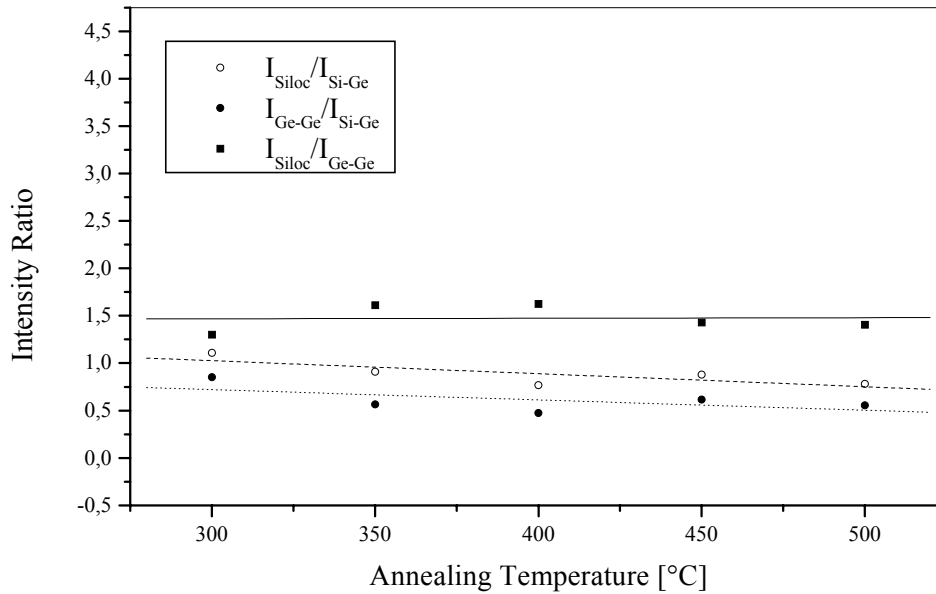


Figure 67: The integrated intensity ratios $I_{\text{Siloc}}/I_{\text{Si-Ge}}$ and $I_{\text{Ge-Ge}}/I_{\text{Si-Ge}}$ and $I_{\text{Siloc}}/I_{\text{Ge-Ge}}$ recorded at different annealing temperatures of the RTCVD sample.

All ratios can be regarded as constant and can be fitted linearly, indicating no interdiffusion or segregation at these annealing temperatures and for annealing times of about 15 min. The small deviations are within the experimental error. The linear fits in Figure 67 only indicate a trend of the data and have no further physical meaning.

5.2.1.4. RTCVD Samples annealed without Contamination

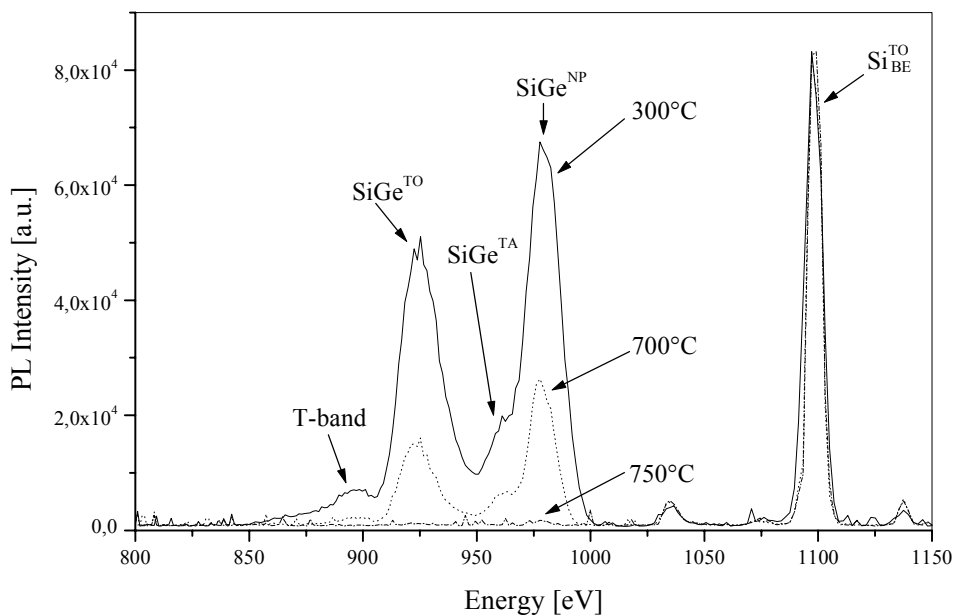


Figure 68: PL spectra of the p-i-n⁺ RTCVD samples annealed in vacuum at 300 °C, 700 °C and 750 °C, respectively.

5.2. RTCVD Samples

Figure 68 shows PL spectra of the RTCVD samples annealed in a high vacuum at 300 °C, 700 °C and 750 °C, that is avoiding metallic contamination. All samples were treated in the same manner, i.e., they were kept at the annealing temperature for 15 min. However, due to the vacuum environment the cooling process to about 250 °C takes about 4 min, whereas it takes about 45 min down to room temperature.

Clearly the intensity of the SiGe bands is damped with increasing annealing temperature. At 750 °C nearly all the SiGe related emission has vanished, indicating strong interdiffusion and lattice relaxation and thus the incorporation of non-radiative defects. No shift of the luminescence lines is detected. Thus, one can conclude, that interdiffusion only takes place at the interfaces, whereas towards the centre of the quantum well layers the Ge concentration still remains the same. Thus, excitons can still diffuse to the low energy areas in the centre of the quantum well layers and recombine there. This is consistent with the observations from micro Raman spectroscopy.

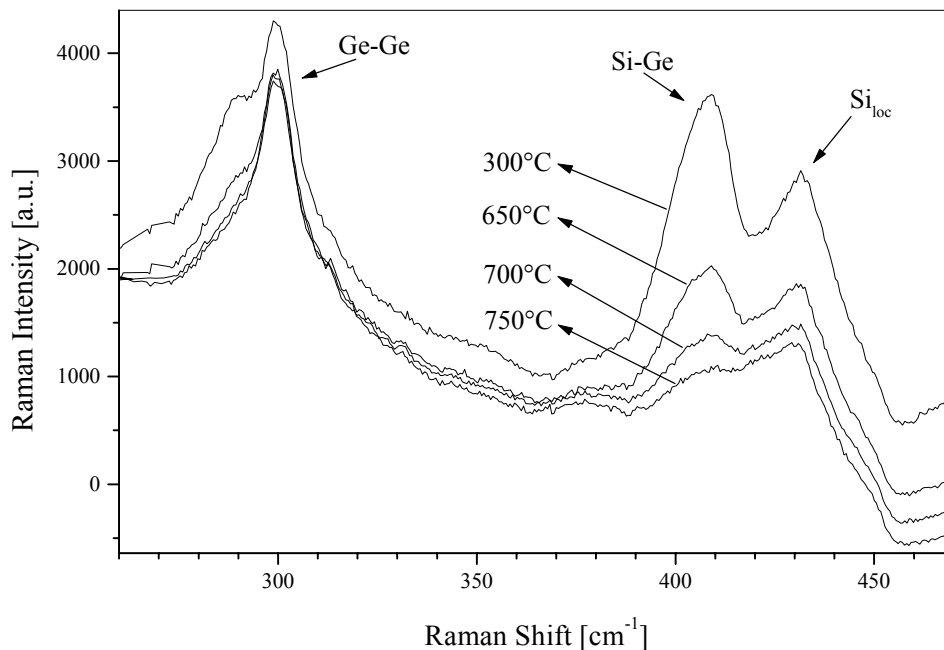


Figure 69: Raman spectra of the RTCVD samples recorded with the 514.5 nm line of an Ar⁺ ion laser. Raman frequencies resulting from Ge-Ge, Si-Ge and Si_{loc} modes are indicated.

To compare the intensity ratios of the different modes, all spectra were corrected for the background signal by subtracting a straight line.

5.2. RTCVD Samples

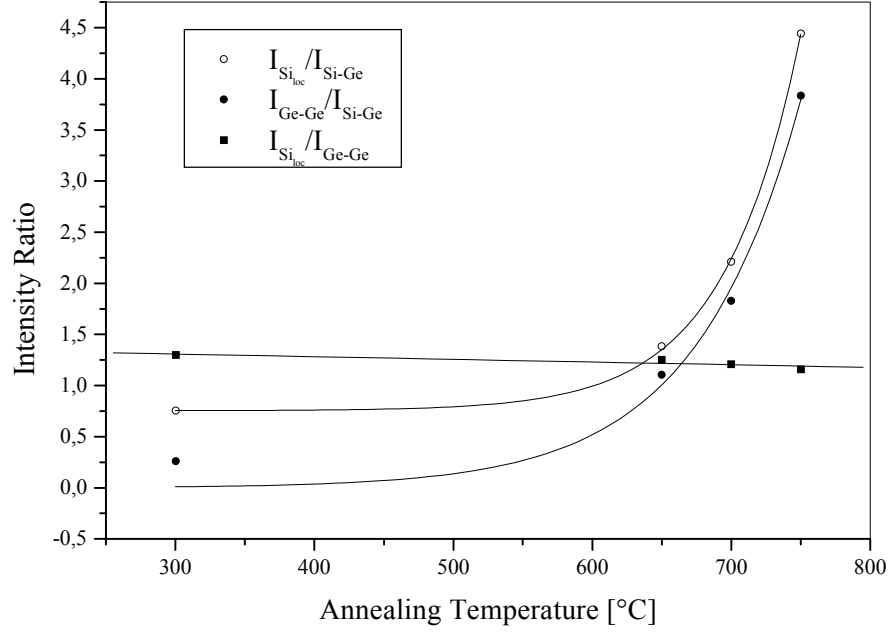


Figure 70: The integrated intensity ratios I_{Si-loc}/I_{Si-Ge} and I_{Ge-Ge}/I_{Si-Ge} and I_{Si-loc}/I_{Ge-Ge} recorded at different annealing temperatures of the RTCVD sample. Both ratios can be well fitted to an exponential growth function.

Both intensity ratios can be well fitted to an exponential growth term, as given by

$$\frac{I_{Si-loc}}{I_{Si-Ge}} = 0.75 + 0.01 \cdot e^{\frac{T}{54.94}} \quad \text{and}$$

$$\frac{I_{Ge-Ge}}{I_{Si-Ge}} = 0.12 + 0.01 \cdot e^{\frac{T}{75.35}}.$$

From the increasing ratio of the $Si_{loc}/Si-Ge$ vibrations with increasing annealing temperature one can conclude that the amount of $Si-Ge$ bonds is decreasing exponentially with the annealing temperature. The exponential dependency hints to an interdiffusion process, which can be described by an error-function like dependence. However, the ratio of the $Ge-Ge/Si-Ge$ vibrations is also increasing with increasing annealing temperature. This can only be explained accounting for a lateral rather than vertical interdiffusion across the interface. Thus, it would appear that Ge tends to form lateral clusters. The same phenomenon was also observed from the x-ray diffraction studies on the two samples grown by MBE at different growth temperatures.

The ratio of the $Si_{loc}/Ge-Ge$ vibrations is expected to be constant in this model. The slight decrease with the annealing is within the experimental error.

5.2. RTCVD Samples

5.2.2. Structural Characterisation

5.2.2.1. SIMS

For the RTCVD grown sample SIMS depth profiles were recorded at the Philips Research Laboratories in Eindhoven to check the doping profiles as well as the layer thickness. SIMS is a very powerful technique due to its high sensitivity to low atomic concentrations. By comparing the signal intensity obtained from a certain material with the equivalent intensity of a reference sample with a known atomic concentration of this element, it is possible to obtain a plot of the atomic concentration versus the depth in the sample. The spectrum was recorded with a sputtering rate of 1.980 nm/min. The B-doping profile agrees well with the target value. The thickness of the Si barriers as well as the SiGe quantum wells correspond to the x-ray data.

Figure 71 shows the SIMS profile of the sample. The upper curve is the Ge concentration (not calibrated), the lower one is the Boron (B) concentration. One can see easily the multiple quantum well structure as the Ge concentration varies periodically from 36 to 160 nm, with a periodicity of 8,4 nm. These values correspond coarsely to the targeted growth rates as described in section 5.2. Moreover, the Boron concentration is high in the Si cap layer, which is intentionally p-doped with Boron (B).

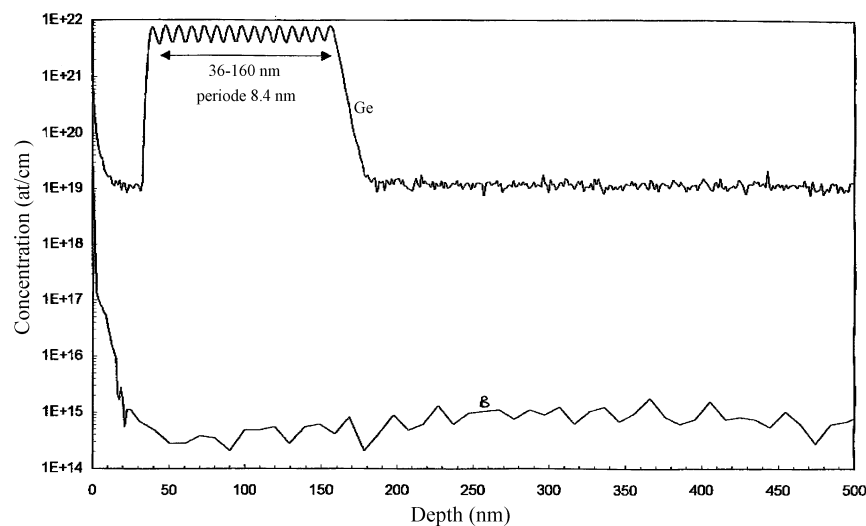


Figure 71: SIMS profile of the n-i-p⁺ RTCVD sample.

5.2. RTCVD Samples

5.2.2.2. X-Ray Reflectivity and Diffraction

Figure 72 shows an x-ray reflectivity scan of the as grown n-i-p⁺ RTCVD sample (open circles in the upper part). The scan was recorded over 18 hours up to about 6.6°, clearly showing 5 superlattice reflections. In the scan also the fitting of the curve is included. As already discussed in section 3.5.3 the fitting was performed using the Parratt formalism. In the fitting of the data the silicon cap was assumed to include a 0.5 nm thick SiO₂ layer. The x-ray data could be fitted very well, assuming that all SiGe layers, as well as all Si barriers, are characterised by the same layer thickness, roughness and index of refraction, thus keeping the number of free fitting parameters to a minimum. The reflectivity and diffraction data are shown in Figure 72 and 73. From the fit to the reflectivity data, the Si barrier roughness was determined to be 0.38 nm, whereas the SiGe surface roughness was found to be 1.9 nm. We attribute the high SiGe roughness to a strong strain-induced Ge segregation, since the quantum wells accommodate maximum strain.

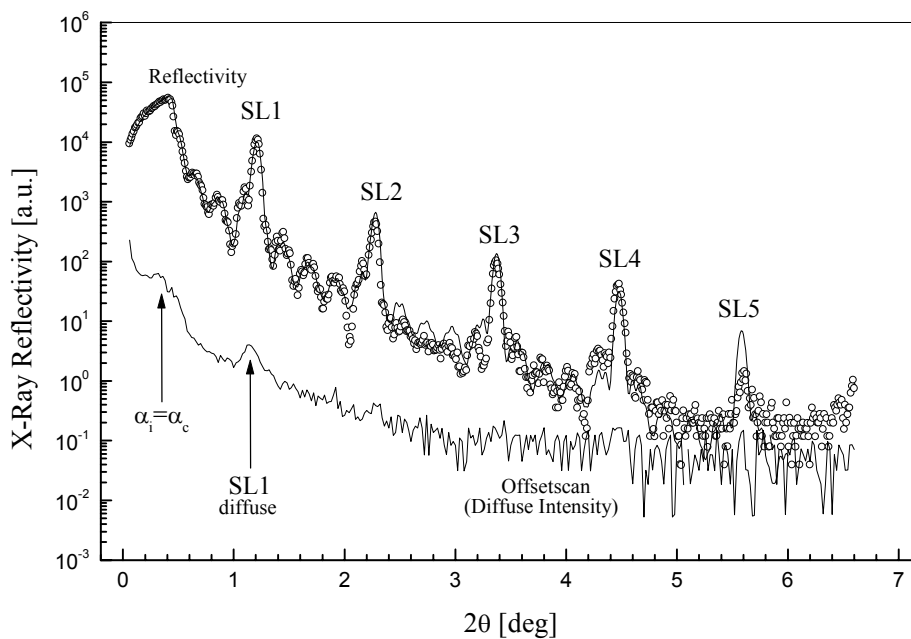


Figure 72: X-ray reflectivity scan including the fit to the data. The lower trace is an offsetscan.

The bottom curve in Figure 72 shows an offsetscan recorded at grazing incident angles. This scan is basically a θ - 2θ scan, only that one adds an offset to the θ value. The offset has to be chosen high enough to avoid detection of the reflected beam. In this case an offset of 0.15° was chosen. By doing this, diffuse reflected intensity around the reflected beam can be recorded. Before fitting the reflectivity curve, this diffuse intensity must be subtracted from the reflected beam. At small incident angles one can clearly distinguish

5.2. RTCVD Samples

two bumps in the offset scan. The bump at smaller angles appears, when the incident angle or the reflected angle are equal to the critical angle α_c for total external reflection. This is a pure optical phenomena and is related to the maximum of the transmission function at this angle.

The second peak, referred to as SL1 diffuse, indicates a correlated roughness within the multiple quantum wells. Similar to superlattice reflections in the normal reflectivity mode, also the diffusive reflected intensity from the different layers can interfere if the roughness from layer to layer is correlated. Weak peaks at the positions of the 2nd, 3rd and 4th diffuse superlattice reflection indicate that this correlation is very strong, backing-up the assumptions in the fitting formalism that all the Si and SiGe layer have comparable roughness.

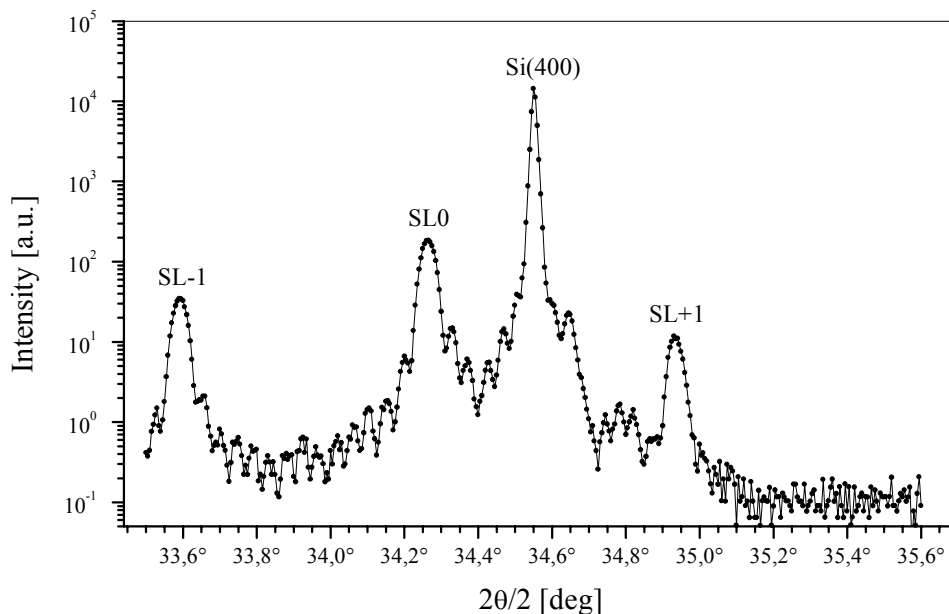


Figure 73: X-ray superlattice diffraction at higher angles also shows Bragg reflection from the substrate.

5.2.2.3.X-Ray Topography

Figure 74 shows the x-ray topograph of the as-grown n-i-p⁺ RTCVD sample. Topographs were obtained by using a “nearly” perfect Si (100) oriented monochromator using the (422) asymmetric reflection for the CuK α line with a grazing incidence angle of 8.7 degrees and a Bragg angle of 44 degrees. To obtain a dispersion-free setup the grazing incidence geometry with the same reflection was used for the sample crystal.

5.2. RTCVD Samples

The different darkening of the x-ray topograph depends on the different local beam intensity. In the upper part of the topograph a visible striation contrast is probably connected to the corrugation of the SiGe/Si interfaces, as determined by X-ray reflectivity. Figure 75 show topography images of the samples studied, annealed at 200 (left) and 500 °C (right), where Ge concentration undulations are visible with a lateral separation of 8-10 μm and 20-30 μm , respectively. Due to experimental reasons the sample annealed at 500 °C had to be rotated by 90 ° during the recording of the topograph. For all three samples the clearly visible striations are oriented only along the [011] direction. It could not be evaluated if some deviation of the surface orientation from the (100) plane is present. In that case the miscut angle could give rise to some preferential strain release or surface roughening. However, the wafers are nominally (001) oriented with an accuracy of about $\pm 0.1^\circ$.

There are two length scales of such undulations present along the SiGe layers, one is in the micro- and the second in the macro-scale. The striations visible in the topographs are periodical strain fluctuations due, for instance, to local Ge concentration fluctuations, in agreement with x-ray reflectivity measurements. In the sample annealed at 500 °C, the striations appear to be distributed more irregularly, with the presence of many short segments. A possible explanation of such features is the formation of bunches of misfit dislocation segments during annealing, induced by the local strain arising from Ge concentration fluctuations. In this case the limited mobility of dislocations in the SiGe alloy [168] would result in the formation of short misfit segments during annealing. It is suggested that changes of the interface strain field are likely to result in interface misfit formations even at moderate annealing temperatures.

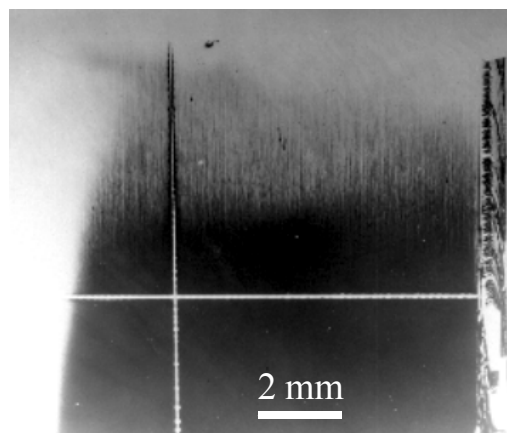


Figure 74: Double crystal 422 CuK α reflection X-ray topograph of the as grown sample.

5.2. RTCVD Samples

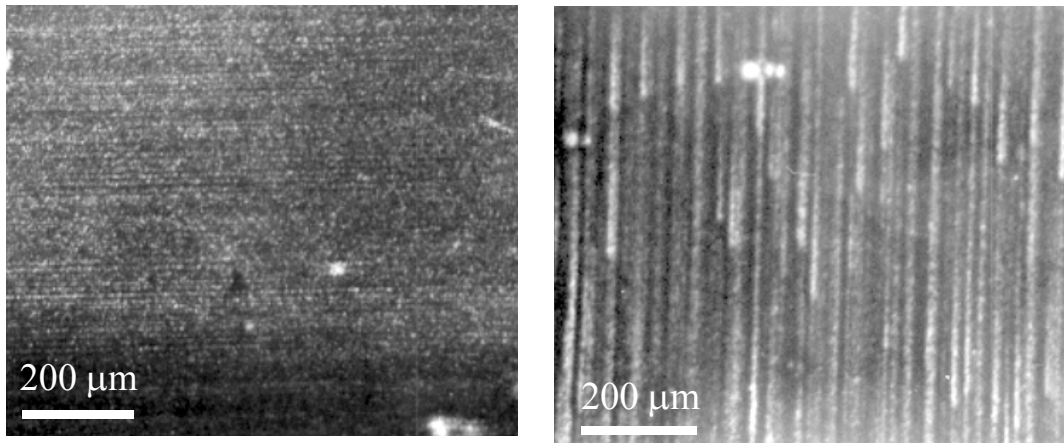


Figure 75: Double crystal $422 \text{ CuK}\alpha$ reflection X-ray topograph of the sample annealed for 10 min in Ar atmosphere at 200 °C (left) and of the sample annealed for 10 min in Ar atmosphere at 500 °C (right).

5.2.2.4. Transmission Electron Microscopy

Figure 76 shows a cross sectional TEM micrograph of an as-grown n-i-p⁺ RTCVD sample, recorded by Dr. S. Christiansen at the Friedrich-Alexander-Universität in Erlangen. The period and the layer thicknesses correspond well with the results obtained from x-ray reflectivity.

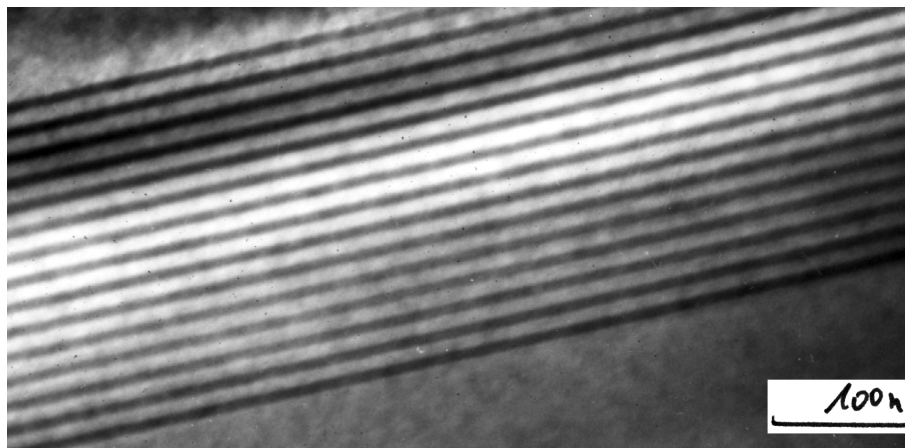


Figure 76: Cross sectional TEM micrograph of the n-i-p⁺ RTCVD sample showing the 15 period Si/Si_{0.77}Ge_{0.23} (4.1 nm/3.9 nm) multiple quantum well.

We observe a very good correlation with the results obtained from x-ray reflectivity experiments, i.e., layer thickness and layer roughness. SiGe surfaces are clearly rougher than the Si ones.

5.2. RTCVD Samples

HRTEM micrographs reveal strong undulations within the SiGe layers with a lateral period of about 7-11 nm as indicated by arrows in Figure 77.

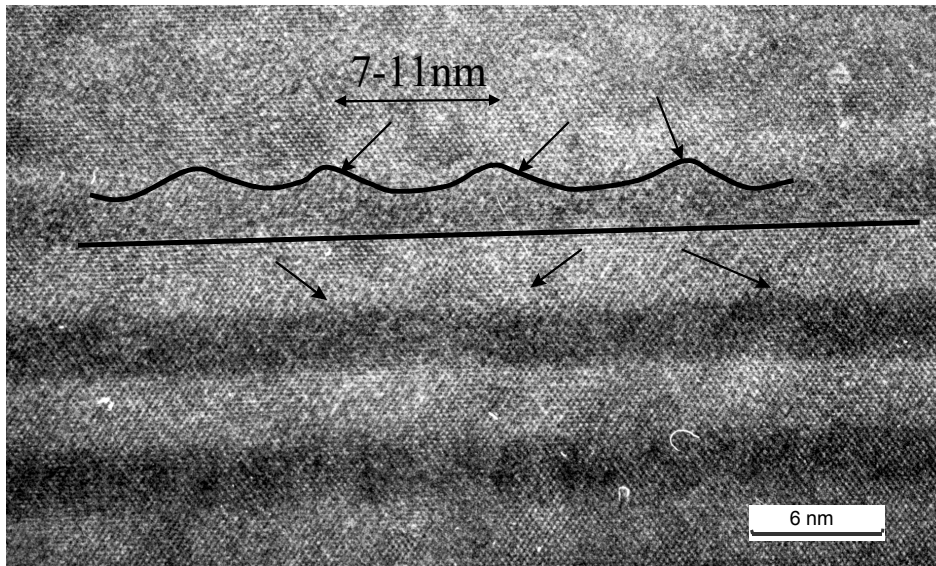


Figure 77: Cross sectional TEM image of the as-grown sample showing a closeup of the Si/SiGe interfaces. Undulations at the interfaces are marked by arrows. The layer thicknesses and the interface roughness are in good agreement with the results of x-ray reflectivity experiments.

From HRTEM and x-ray topography analysis two different lateral scales of such potential fluctuations were determined.

5.3. Comparison of MBE and RTCVD Samples

Figure 78 shows x-ray reflectivity scans of the two MBE grown sample L6 and I17 and of the as-grown RTCVD p-i-n⁺ sample together with the fits to curves. As the RTCVD sample has a different period than MBE samples, the superlattice reflections are shifted to lower incident angles θ . The period of the two MBE grown samples is 60 nm in contrast to 80 nm for the RTCVD sample.

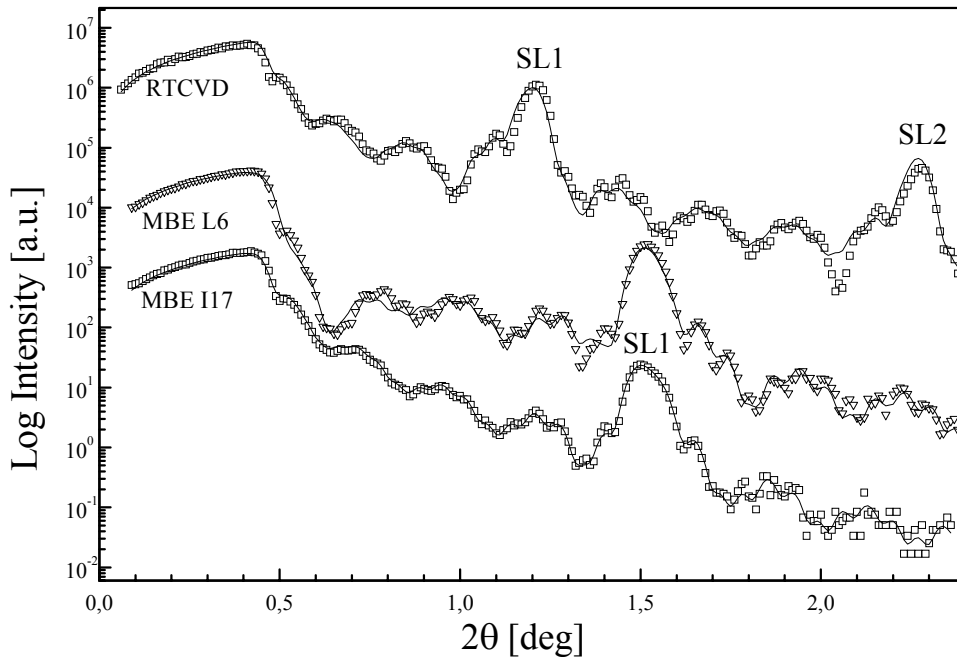


Figure 78: X-ray reflectivity data together with fitting curves based on Parratt formalism [130,131].

Figure 79 shows the x-ray diffraction data of the three samples in comparison. Similarly to the reflectivity data the superlattice reflection is shifted for the RTCVD sample closer to the Si(004) Bragg reflection from the silicon substrate. This is due to the slightly lower Ge concentration of 23 % in comparison to the 25 % for the MBE grown samples.

5.3. Comparison of MBE and RTCVD Samples

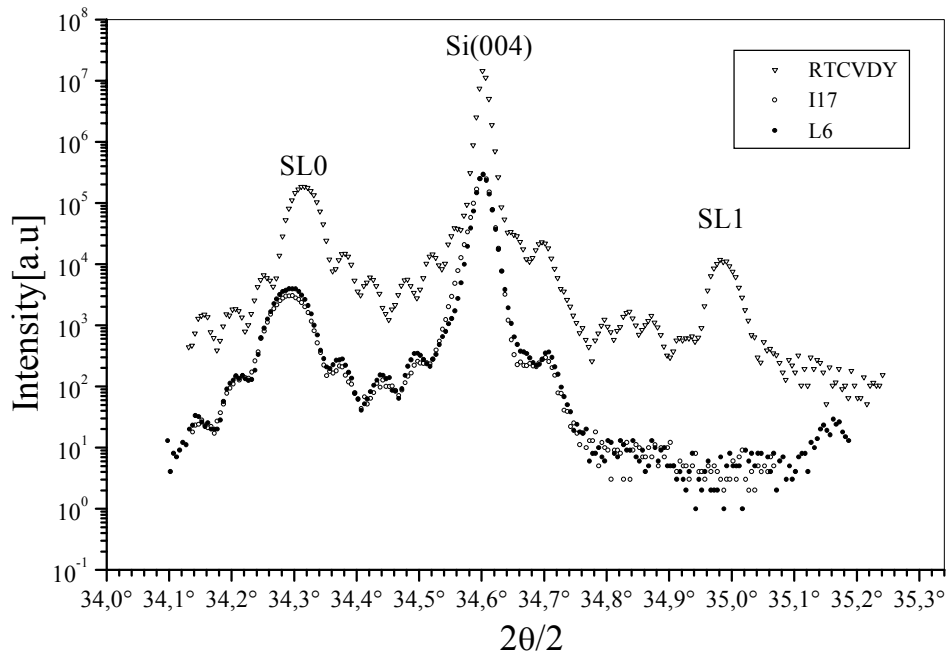


Figure 79: X-ray diffraction data showing Bragg reflection from the substrate at higher incident angles around 34.6° .

Figure 80 shows the integrated photoluminescence data of the three basic type of samples in an Arrhenius plot. In the case of the RTCVD sample thermal quenching could be reduced so that room temperature photoluminescence was observed, though this is still too weak to be of any practical use.

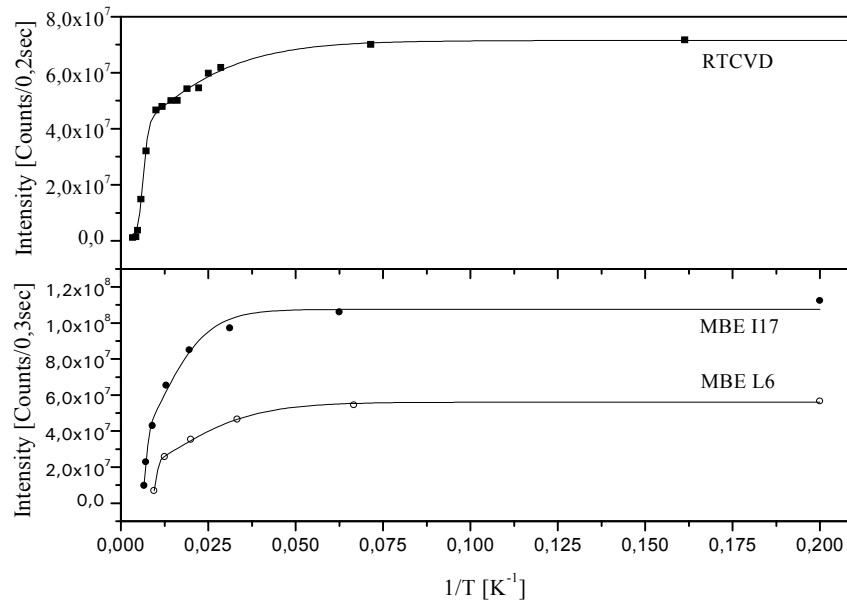


Figure 80: Arrhenius plot of the integrated SiGe PL intensity of an RTCVD grown MQW structure (upper part) and of two MBE samples of a similar structure (lower part), where the active regions were grown at different temperatures (MBE I17 at 650°C , MBE L6 at 600°C , and RTCVD at 625°C).

5.3. Comparison of MBE and RTCVD Samples

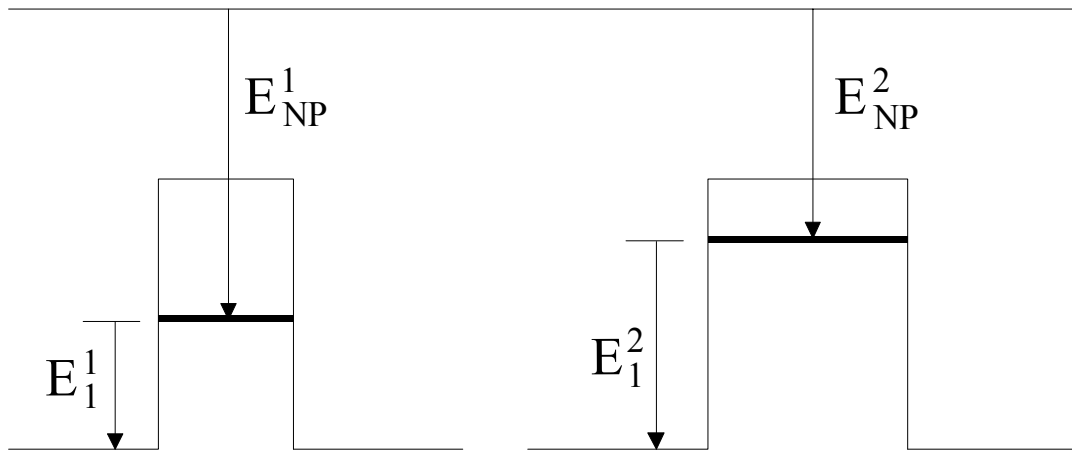


Figure 81: Schematic view of the different confinement levels for the thinner wells in the case of the MBE samples (left side) and for the thicker RTCVD samples (right side).

A thinner well leads to a stronger exciton confinement in the case of the MBE samples and therefore to a larger energy E_{NP}^1 energy, as clearly visible in the photoluminescence spectra of the different samples. However, the confinement also affects the quenching temperature. Due to the smaller energy E_1^1 in comparison to E_1^2 holes can easily escape out of the MBE wells at elevated temperature. This is, why the RTCVD sample shows luminescence up to room temperature. Thus, ideally, one would like to have even thicker $\text{Si}_{1-x}\text{Ge}_x$ wells hitting the critical thickness for the pseudomorphic growth. The Si-Ge^{TO} , Ge-Ge^{TO} and Si-Ge^{TA} replicas are stronger for the thicker RTCVD quantum wells than for the narrower MBE wells. This effect can also be attributed to the enhanced leakage of the exciton wavefunction into the barrier at smaller well thickness [169]. This trend is consistent with the intensity data given by Weber and Alonso [57] for unstrained SiGe alloys. In the case of the RTCVD sample, the thickness is already very close to the critical limit resulting in highly strained layers. Thus, already a moderate post-growth annealing was sufficient to create local misfit dislocations most probably at the very end of the Ge striations.

5.3. Comparison of MBE and RTCVD Samples

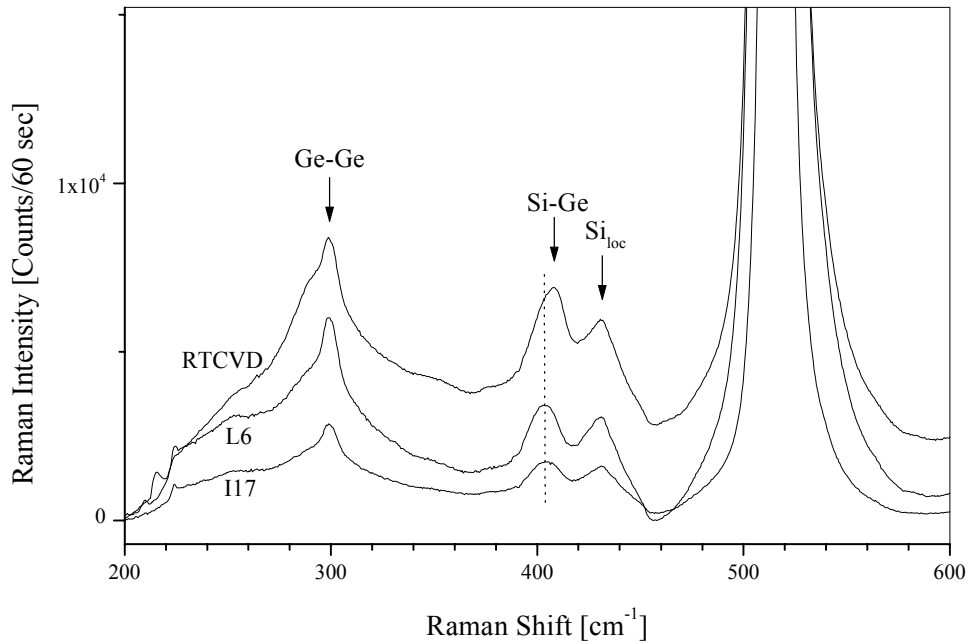


Figure 82: Raman spectra of the as-grown MBE and RTCVD samples recorded with the 514.5 nm line of an Ar^+ ion laser. Raman frequencies resulting from Ge-Ge and Si-Ge modes are indicated. The shift of the SiGe mode between the MBE and the RTCVD samples results from the slightly different Ge concentration of 25% and 23%, respectively.

The shift to higher frequencies between the MBE and RTCVD samples in the micro Raman spectra of the three different samples shown in Figure 82 clearly demonstrate the different Ge concentrations between the MBE and the RTCVD samples. This indicates one more, that Raman spectroscopy is a very sensitive tool to determine Ge concentrations. In this work no further analysis of the Raman data was performed, as the Ge concentration is well known from x-ray diffraction. Raman spectroscopy was only qualitatively used to determine the influence of interdiffusion due to the post-growth annealing.

5.4. Electroluminescence

5.4.1. Structure of the EL-Diode

To fabricate a light emitting diode a piece of the highly doped $n^+ - i - p^+$ RTCVD sample was used. A SIMS profile is shown in Figure 83 where the dopant profile is clearly distinguished.

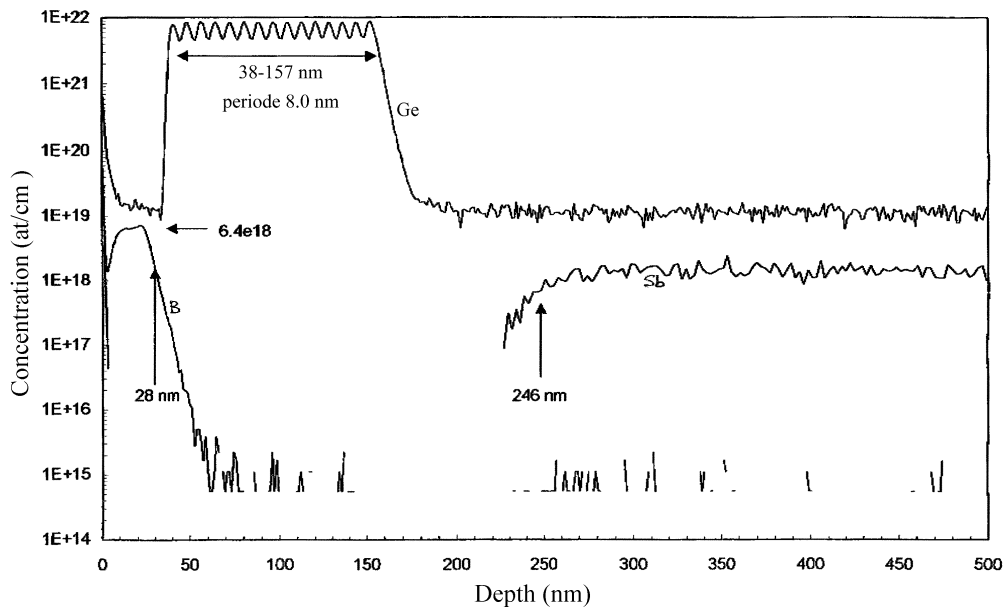


Figure 83: SIMS profile of the $n^+ - i - p^+$ RTCVD sample.

The spectrum was recorded with a sputtering rate of 1.980 nm/min. The B-doping profile agrees well with the target value. The thickness of the Si barriers as well as the SiGe quantum wells correspond to the x-ray data.

The upper curve is the Ge concentration (not calibrated), the lower one shows the Boron (B) and Antimonite (Sb) concentrations. One can see easily the multiple quantum well structure as the Ge concentration varies periodically from a depth of 38 to 157 nm, with a periodicity of 8,0 nm. These values correspond coarsely to the targeted growth rates as described in section 5.2. Moreover, the Boron concentration is high in the Si cap layer, which is intentionally p^+ -doped with Boron (B). The middle trace shows the Antimonide concentration in the buffer layer, which is ententionally n^+ -doped with Antimonide (Sb).

For the top-contact a 1500 Å ITO was grown. Prior to the ITO growth the Si/SiGe sample was cleaned using the standard RCA process. In this respect, the sample was first emerged in a $H_2O_2:NH_4OH:H_2O$ (1:1:1) solution at 80 °C for about 30 min.

5.4. Electroluminescence

After rinsing the sample in deionised H₂O, a second treatment was performed in a H₂O₂:HCl:H₂O (1:1:5) solution with an adjacent rinsing in deionised H₂O. Through this process metallic and organic contamination is removed. In the latter step the surface is oxidised, so that a thin and clean SiO₂ layer forms at the surface (~2-3 nm). Dipping the sample in HF shortly before introducing it into the evaporator removes the oxide layer and passivates the surface with hydrogen (H). Due to H-passivation the Si surface becomes hydrophobic. Thus, a further oxidation of the surface, e.g. due to O₂ in the air, can be avoided [170].

During ITO growth the sample was annealed to 450°C. The In/Sn was evaporated at a rate of ~1.5 Å/sec (T_{In}=835°C, T_{Sn}=1000°C). Prior to opening the cell shutters, an oxygen pressure of 2.1*10⁻⁴ mbar was adjusted and kept constant during the whole growth. The growth was performed through a molybdenum mask in order to obtain ITO stripes serving as a mask for a further wet chemical etching step. Figure 84 shows a schematic viewgraph of the LED structure.

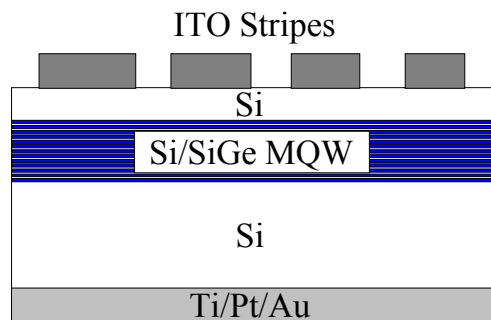


Figure 84: Schematic view of the Si/SiGe LED with a Ti/Pt/Au bottom and a ITO top contact.

However, although in the case of pure Si ITO served well as an etch mask using a potassium-hydroxide (KOH) /isopropanol solution, in the case of the Si/SiGe MQW this etching recipe did not work as the whole multilayer structure was etched away.

For the final LED device, one of the middle stripes was contacted using silver loaded epoxy.

5.4.2. PL of the EL structure

In Figure 85 the 15 K PL spectrum is shown.

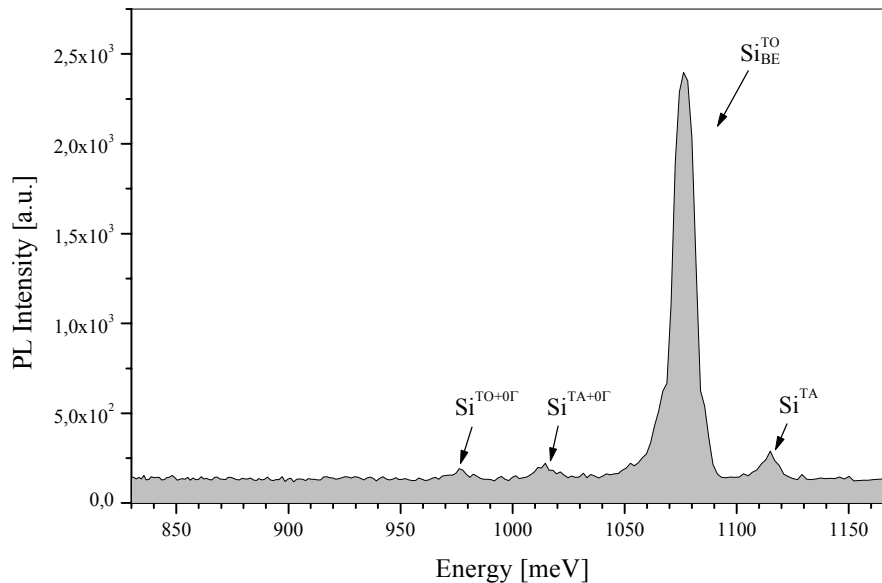


Figure 85: PL spectrum of the n^+i-p^+ RTCVD sample recorded at 15 K at an excitation power density of 400 mWcm^{-2} . The SiGe related emission is missing due to the high doping of the substrate.

Due to the very high doping of the substrate to about 10^{18} cm^{-3} (see 5.2) and thus the presence of non-radiative recombination centres for optically created carriers, the Si emission is strongly quenched. Emission from the SiGe quantum wells is not detectable in this scale. This clearly indicates that due to the high penetration depth of the laser line, excitons, mainly created in the substrate, diffuse to the quantum wells and recombine there. In Si the exciton diffusion length is about $400 \mu\text{m}$ at low temperatures.

5.4.3. Contact Deposition

5.4.3.1. ITO Deposition Tests

First preliminary films have been deposited on various substrates including glass and Si. Whereas the glass substrates are needed for transparency measurements, the silicon substrate is very useful for SEM cross-sectional analysis of the films, as silicon can easily be cleaved. Figure 86 shows two cross-sections of an ITO film on Si at different positions and at different magnifications. Though the ITO grows in a dendritic structure (left image), a closed, grainy layer grows right at the interface to the surface. This effect is clearly visible on the right image of Figure 86.

5.4. Electroluminescence

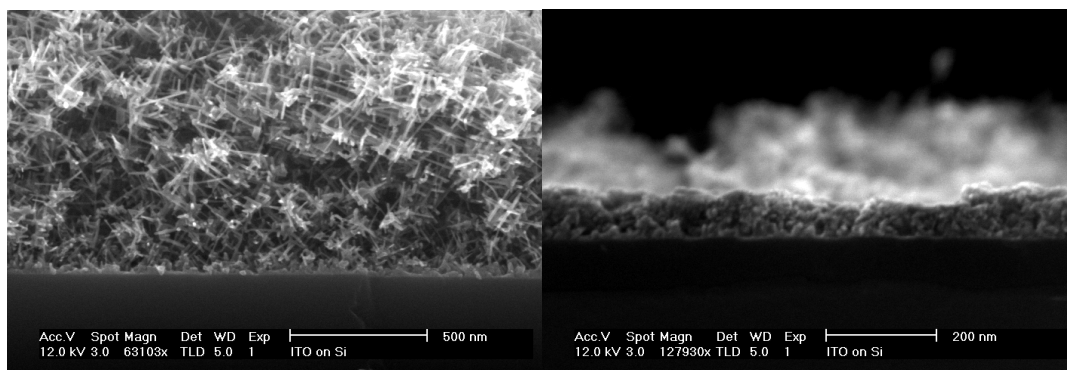


Figure 86: Cross sectional high resolution SEM micrographs of an ITO layer deposited on Si. Both images are recorded from the same sample at different positions. Clearly one can recognise a contiguous layer at the interface to the Si substrate, whereas on top of that layer dendritic growth starts.

One possible explanation for this distinct growth mode modification from grains to dendritic growth during deposition, while the growth parameters were not changed, is due to the difference in the growth rate. Using effusion cells, the shutters are regularly kept closed until the temperature in the cells is reached and the pressure in the chamber drops to a sufficiently low level after the increase due to heating of the cells ($\sim 10^{-6}$ mbar). Thus, there is a rather high pressure inside the cells. Therefore, the growth rate is about a factor of two higher than the normal evaporation rate, once shutters are opened. A high evaporation rate reduces the surface diffusion of the impinging atoms and molecules on the substrate surface enabling the growth of a closed layer. After the growth rate drops back to its normal value, diffusion phenomena gain importance resulting in the dendritic growth. An alternative explanation is related to the radiative heating of the substrates. Both, the glass and the Si substrates are highly transparent in the infrared.

After the deposition of ITO starts, the IR absorption (and thus also the temperature) of the thin film and substrates increases with ongoing film deposition. This would explain the modified growth mode. In conclusion, both effects may contribute to the existence of the grainy interface structure.

5.4. Electroluminescence

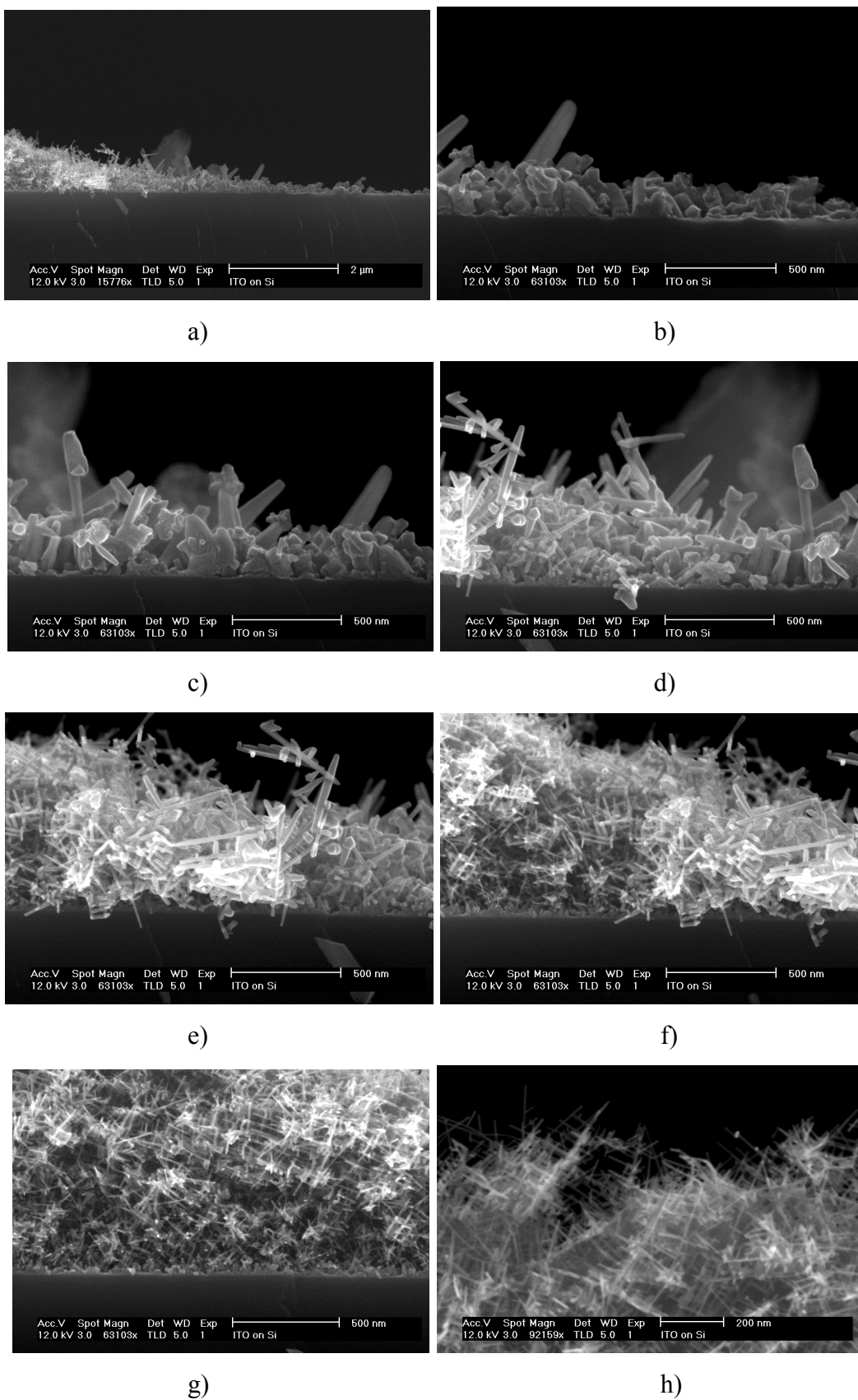


Figure 87: SEM micrographs showing the effect of a temperature gradient from approximately 200°C-600°C on the structural properties of ITO growth.

5.4. Electroluminescence

Figure 87 shows an ITO layer grown on a Si(100) substrate through a metallic stripe mask as indicated in Figure 88. The SEM micrographs are taken perpendicular to the length axis of such an ITO stripe. The metal mask in direct contact with the silicon substrate dramatically modifies the temperature of the substrate because it represents a huge heat sink. Thus, the silicon area underneath the stripe-like openings of the mask have the highest temperature ($\sim 600\text{ }^{\circ}\text{C}$) whereas the covered areas are much colder ($\sim 200\text{-}300\text{ }^{\circ}\text{C}$).

Figure 87 a shows the edge of the deposited ITO layer. The right side of the stripe which was near the metal during deposition shows much bigger structures than the areas with the higher substrate temperature. Figure 87 b-g show a series of SEM micrographs recorded at different positions from the right side of the ITO stripe in Figure 87 a to the left side which is approximately in the middle of the $\sim 2\text{mm}$ wide stripe. Figure 87 h additionally shows a close-up of the dendrites with single wires as thin as $\sim 10\text{nm}$.

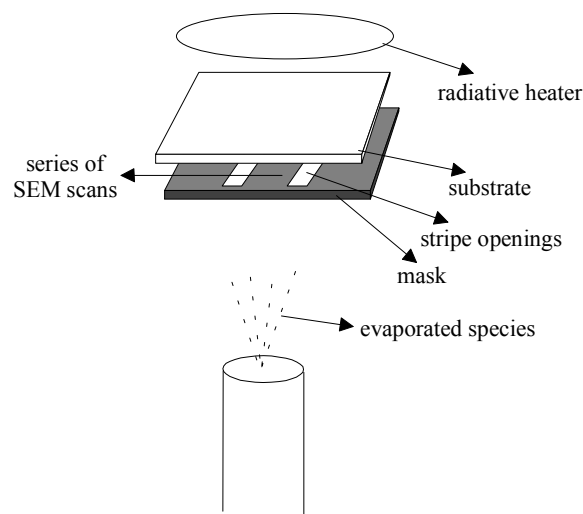


Figure 88: Schematic drawing of the use of a metallic mask for the evaporation process.

As already discussed above the growth rate and the growth temperature are key parameters determining for the structural properties of ITO.

Figure 89 shows the transmission of ITO films in the visible range at various substrate growth temperatures. The transmission increases with increasing growth temperature. Further investigations have shown that the higher the growth rate the more grainy the films get. At lower rates the growth is strongly diffusion driven and long dendritic needles are formed, as shown in Figure 90.

5.4. Electroluminescence

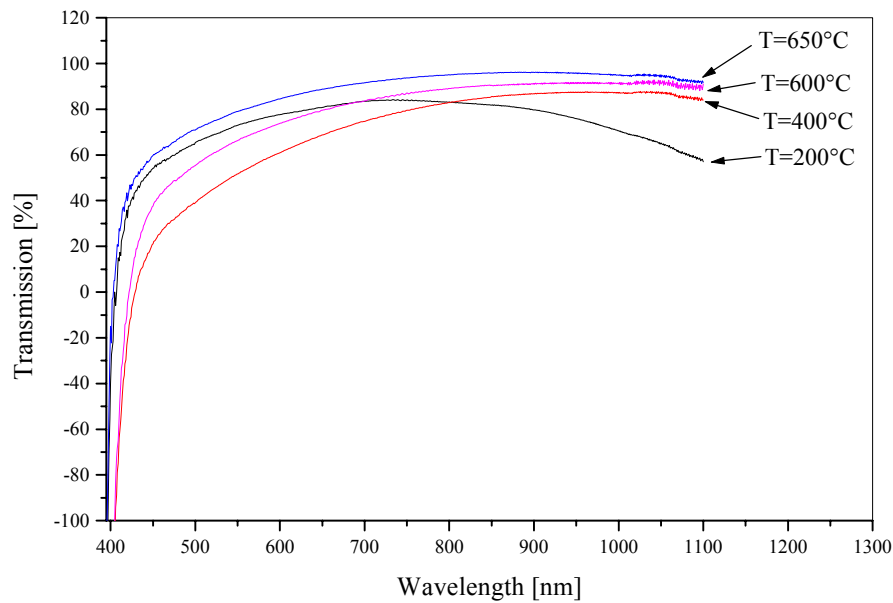


Figure 89: Transmission spectra of ITO films deposited at different substrate temperatures. The growth rate and the oxygen partial pressure were kept constant.

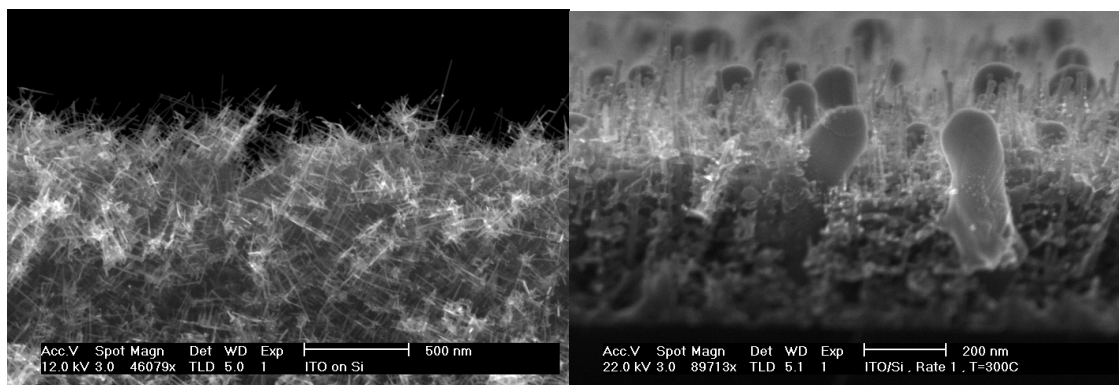


Figure 90: Cross sectional SEM micrographs of two different ITO layers grown at the same conditions. Only the growth rate was modified. The left figure shows the structure grown at 2 Å/sec, the right film is grown at a 13 Å/sec.

In Figure 91 the transmission spectra of three different films, only differing in the growth rate, are shown. Clearly with decreasing growth rate the transparency in the visible range increases up to around 90 %. The strong absorption of ITO for higher wavelengths is due to plasma absorption within the ITO layer due to their rather high electron density of about 10^{23} cm^{-3} .

5.4. Electroluminescence

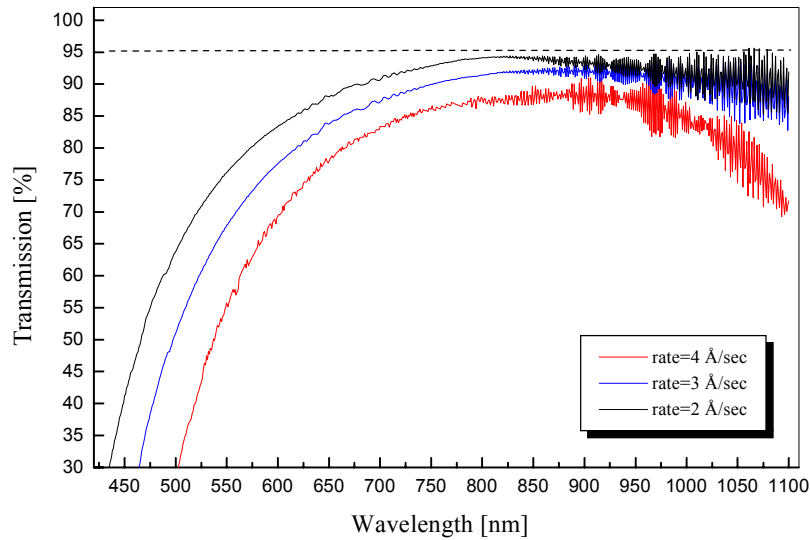


Figure 91: Transmission spectra of 100 nm ITO films grown at 650°C and at different growth rates as indicated in the legend.

For the actual deposition of the ITO layer of the Si/SiGe LED a growth temperature $T_G = 575^\circ\text{C}$ was chosen, resulting in a sheet resistance of about $1700\ \mu\Omega\text{cm}$.

Figure 92 shows transmission spectra of two 150 nm thick ITO layers deposited on glass at two different substrate temperatures. Clearly, the transmission in the near-IR range around 1200-1300 nm, where the LED is emitting, increases from around 20-30 % for a growth temperature of 200°C to about 60-80 % for a growth temperature of 574°C .

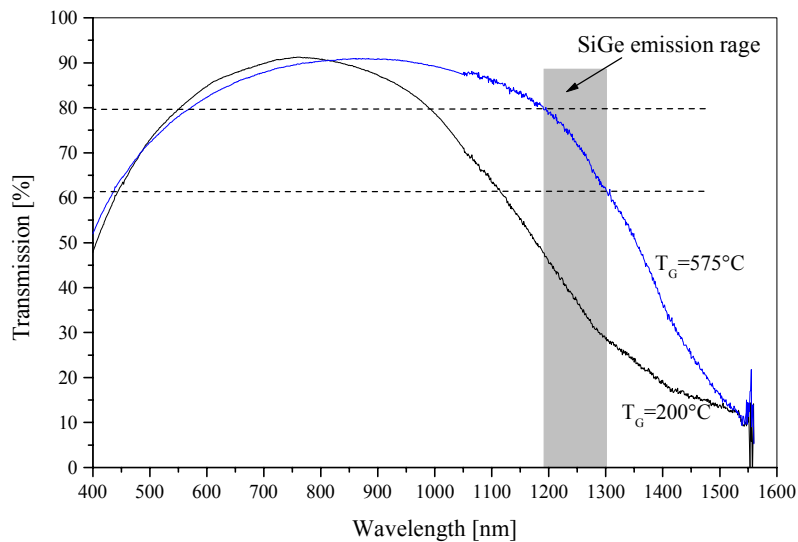


Figure 92: Transmission spectra of the 150 nm ITO film as deposited later on the Si/SiGe LED at a growth temperature $T_G=574^\circ\text{C}$ compared to an ITO layer grown at only 200°C .

At higher growth temperatures the transmission increases on the cost of the sheet resistance of the layer. At temperatures around 700°C , e.g., a sheet resistance of only

5.4. Electroluminescence

about 4000 $\mu\Omega\text{cm}$ was achieved. Thus, by choosing a medium temperature of 575 °C, a compromise between a high transparency and an acceptable sheet resistance was made.

5.4.3.2. Bottom Metal Contact

As aluminium (Al) makes a Schottky contact to n-Si, great care had to be taken to deposit the back-contact of the sample. A triple layer consisting of Ti/Pt/Au was used to this purpose. These layers were deposited by Ms. A.C. Martín in a MBE chamber at the Instituto de Microelectrónica de Madrid, CISC. A 500 Å Ti layer was deposited at room temperature at a rate of 1.5 Å /sec as a diffusion barrier, followed by a 500 Å Pt layer at the same conditions. As the final layer 1000 Å Au were deposited at room temperature at a rate of 3 Å /sec. The back contact was deposited over the whole back surface of the sample.

5.4.3.3. ITO Topcontact Deposition

After the growth parameters for a high transparency around 60-80 % and a sheet resistance of around 1000-2000 $\mu\Omega\text{cm}$ were determined the following parameters were finally chosen to deposit ITO on the $n^+ - i - p^+$ Si/SiGe MQW sample:

Substrate temperature:	575 °C
Growth rate:	~1.5 Å/s (together for both metals)
Layer thickness:	1500 Å
O ₂ partial pressure:	~2.1 · 10 ⁻⁴ mbar

Together with the Si/SiGe sample a glass control substrate was also mounted on the sample holder. The ITO layer deposited on glass was used to determine the sheet resistance and the transparency of the layer. For this sample a sheet resistance of about 1700 $\mu\Omega\text{cm}$ and a transparency of about 60-80 % were measured in the range, where the Si/SiGe LED emits.

The growth takes the form of dendrites under certain growth conditions. Away from the edge, where the ITO structure is modified by the cleaving process itself, single needles with a typical length of a few 100 microns and a width of about 10 to 50 nm seem to be oriented in the growth direction (see.Figure 93)

5.4. Electroluminescence

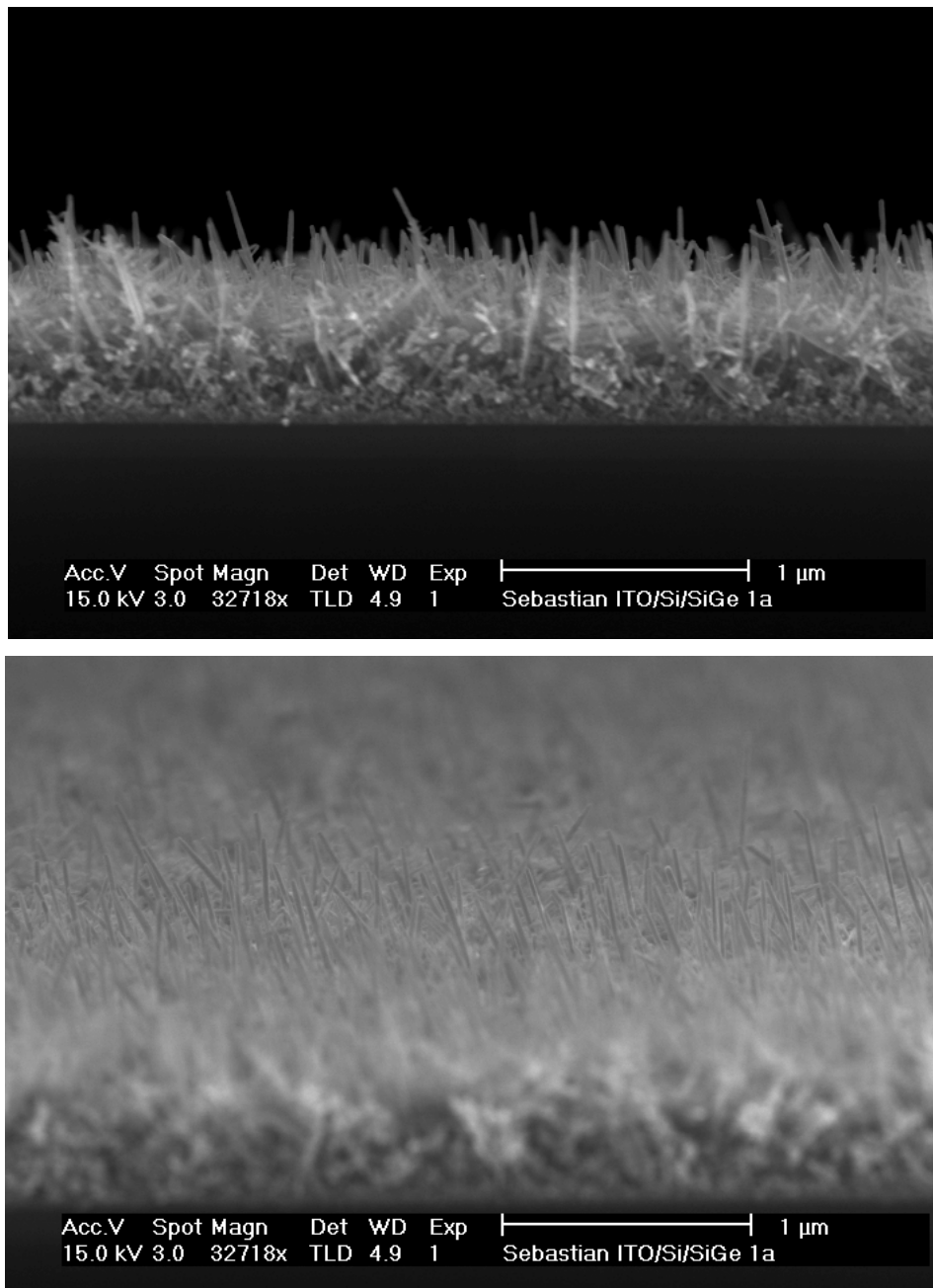


Figure 93: Cross sectional SEM micrographs of the ITO film on Si/SiGe. In the bottom micrograph the sample is tilted by about 7° to visualise also parts of the surface.

The reason for this effect is most probably related to the higher material diffusion in the z-direction towards the incoming atoms and molecules. This observation together with the temperature dependent changes in the structural properties clearly underline the dominant effect of diffusion in the growth mode. The growth of ITO needles is currently being pursued as a separate research project.

5.4. Electroluminescence

5.4.4. Electroluminescence Set-up

Figure 94 shows the electrical circuit driving the diode. As a pulse generator was not available for these experiments, a transistor was used as a switch and could be opened and closed by a pulsed electrical signal with a fixed frequency of 570 Hz supplied by a mechanical chopper. The applied voltage was up to about 4 V, leading to a current flow of up to about 1 A.

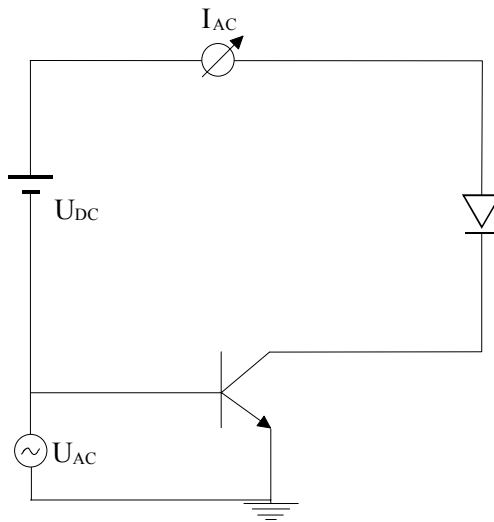


Figure 94: Schematics of the Si/SiGe LED with the driving transistor as a switch to modulate the injection current.

The signal of a DC current source could thus be modulated. From the chopper one could also feed the same signal to a lock-in amplifier measuring the output signal of the Ge detector. The same technique was used for all the PL experiments, only that in that case the primary laser beam was chopped.

5.4. Electroluminescence

5.4.5. EL Spectrum

5.4.5.1. Temperature Dependence of the Electroluminescence

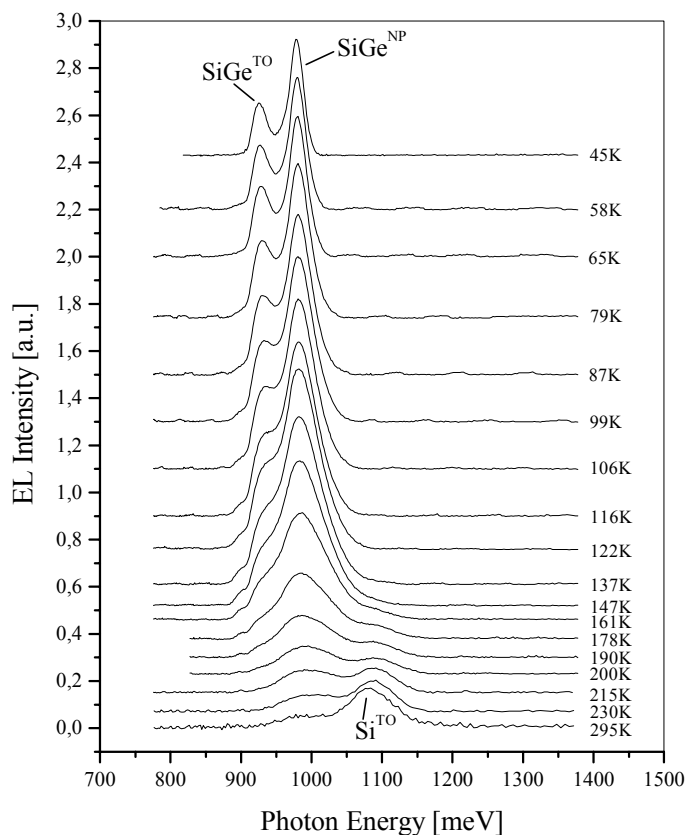


Figure 95: Temperature dependent EL spectra showing luminescence up to room temperature.

In Figure 95 the temperature dependent electroluminescence is shown. A constant driving current of 575 mA was used for these experiments. The supplied power heated up the device limiting the lowest temperature to about 45 K inside the cryostat. The SiGe band-edge electroluminescence is clearly visible up to room temperature. Figure 96 shows the room temperature electroluminescence at an injection current $I=575\text{mA}$. Also shown is a fit of the spectrum with two gaussian curves (dotted lines). At elevated temperatures Si transverse optical phonon assisted band-to-band emission dominates the spectra.

5.4. Electroluminescence

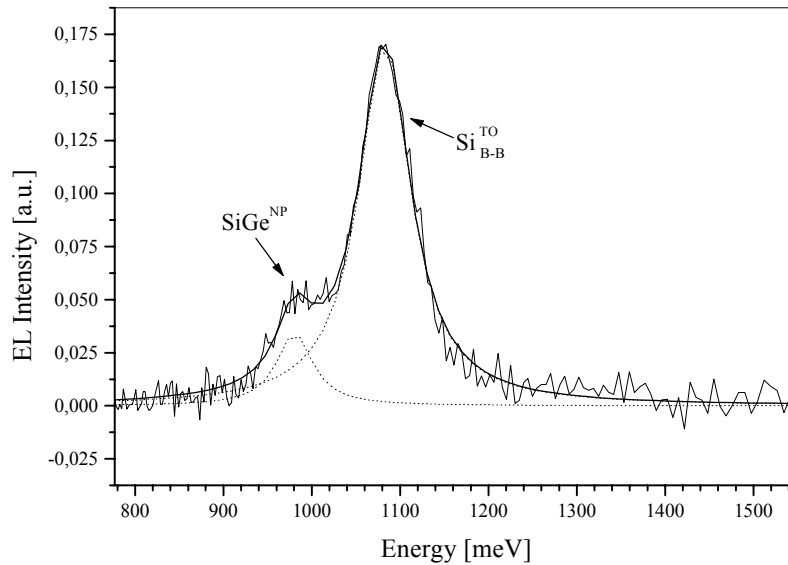


Figure 96 : Room temperature EL recorded at an injection current of 575 mA. The SiGe emission was extracted from all spectra with a multiple gaussian fit.

Figure 97 shows the integrated EL intensity in an Arrhenius plot. At high temperature the integrated EL intensity is strongly quenched as is the photoluminescence. The electro-luminescence is weaker at lower temperatures. The maximum luminescence intensity is observed at temperatures about 130-140 K. The reason for the intensity drop by about a factor of 1.4 to the lowest sample temperatures of about 45 K at this current density is probably related to the structure of the diode. At very low temperatures the current spreading within the SiGe layer is not very significant. Thus, the luminescence comes mainly from the areas directly under the ITO stripe. With increasing temperature the current would spread laterally and the increasing effective SiGe area would thus lead to a stronger luminescence. At even higher temperatures the carriers thermalise out of the wells leading to a strong temperature quenching of the luminescence intensity.

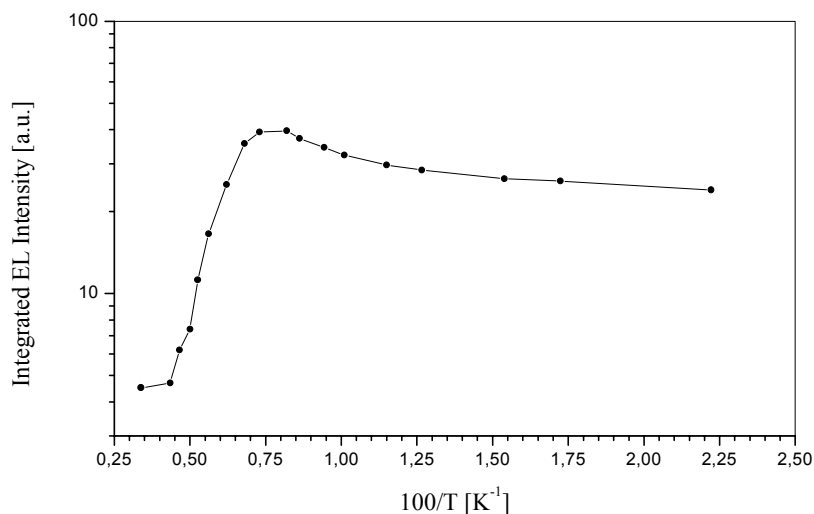


Figure 97: Arrhenius plot showing the integrated EL intensity.

5.4.6. I-V Characteristics

The current I of an ideal p-n or p-i-n diode is described by the Shockley equation. The I-region of p-i-n diodes can be treated such as an enlarged depletion regime. Hereby it is assumed that the current transport across the p-i-n junction is only mediated through thermal activated diffusion, i.e. there is no recombination in the depletion regime and the current density of electrons and holes is constant. The I-V characteristics is then a straight line in forward bias. In the case of real diodes, leakage currents along the surface or leakage currents due to dislocation in the crystal must be taken into account. For a high high quality crystal the diode equation is therefore given by [147]

$$I = I_{Shunt} \cdot e^{\left(\frac{eV}{n \cdot k \cdot T} - 1\right)} + I_{Sur}$$

with

I = current through the diode

I_{Shunt} = shunt current for $eV \ll kT$

I_{Sur} = leakage current along the surface

e = electron charge ($1.6 \cdot 10^{-19} C$)

V = applied voltage

n = ideality factor

k = Boltzmann constant ($5.670 \cdot 10^{-8} Wm^{-2} K^{-4}$)

T = temperature.

I_{Shunt} is only determined by the diffusion of minority carriers, which are thermally created outside the depletion regime. I_{Shunt} is determined by the bandgap and diffusion constants and increases exponentially with the temperature.

The ideality factor n contains information on the existing current mechanism. In the case of $n \approx 1$ diffusion currents dominate, if $n \approx 2$ recombination currents dominate. In the latter case n is measured at the steepest linear part of the forward characteristics. For $1 \leq n \leq 2$ both currents are present. In real diodes an ohmic serial resistance can be present leading to a departure from the ideal diode characteristics. Crystal imperfections affect specially the shunt current, which can increase by orders of magnitude.

5.4. Electroluminescence

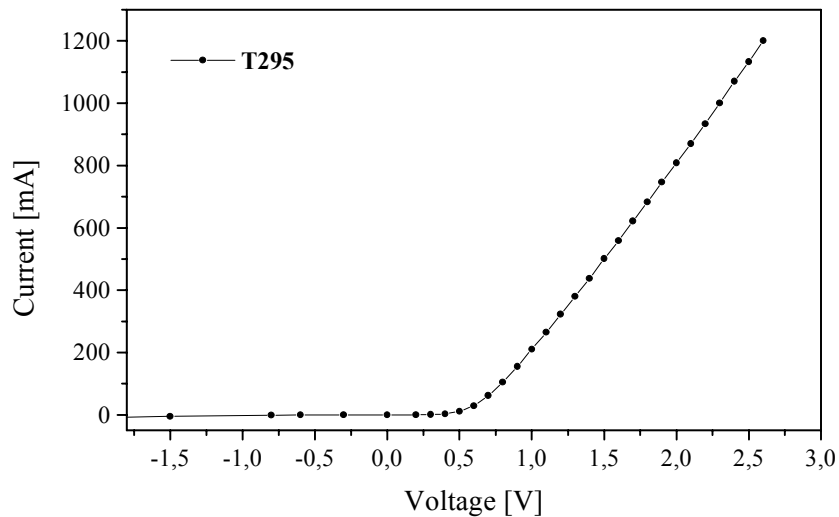


Figure 98: I-V characteristics of the LED recorded at room temperature while the sample is kept in the dark.

Figure 98 shows the room temperature I-V characteristics recorded in darkness to avoid additional carrier creation by room light.

5.4.7. Comparison of the EL- and PL-Spectrum

Figure 99 shows a comparison of photo- and electroluminescence recorded from the n - i - p^+ and the n^+ - i - p^+ RTCVD samples at 50 K, respectively. As expected from the equivalent growth parameters of both samples and from the structural characteristic, the SiGe band-edge luminescence appears at the same position. This indicated, that both luminescence types originate from the multiple quantum wells.

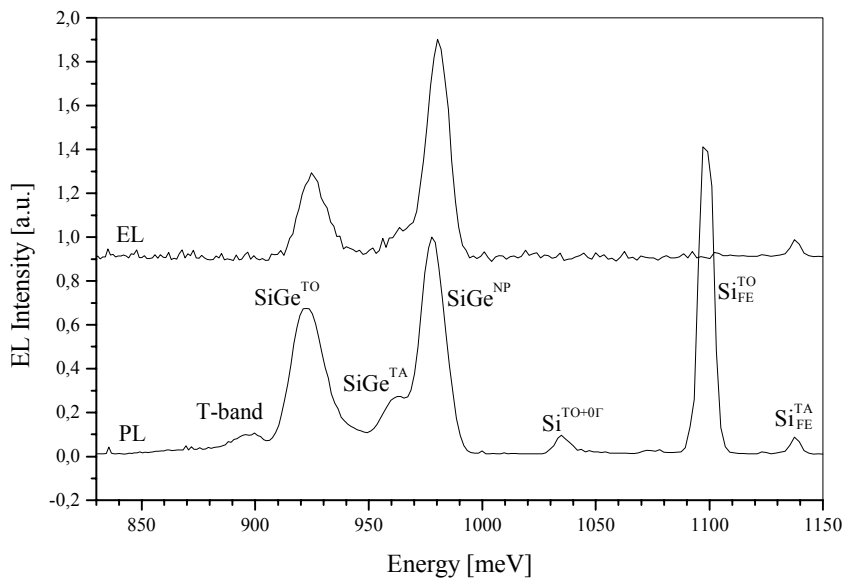


Figure 99: Comparison of the photo- and electroluminescence recorded from the n - i - p^+ and the n^+ - i - p^+ RTCVD samples, respectively.

5.4. Electroluminescence

5.4.8. EL-Intensity as a Function of Current Density

Similarly to the power dependent photoluminescence experiments the electroluminescence was monitored as a function of the injection current density. These spectra are shown in Figure 100.

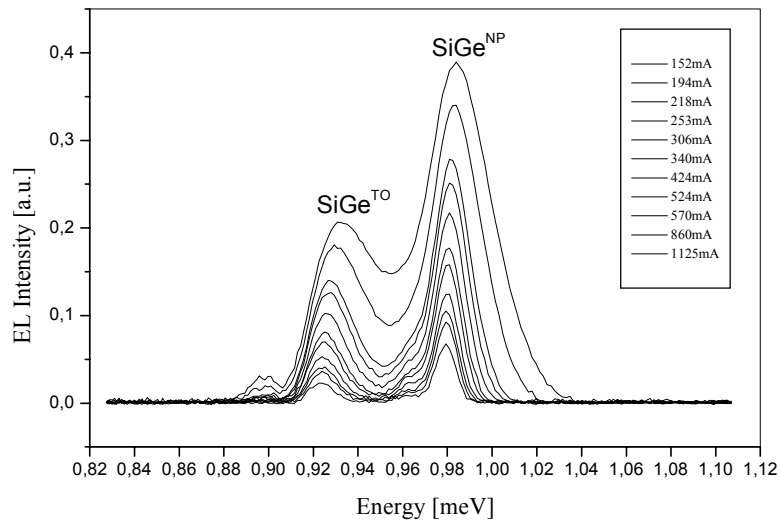


Figure 100: Dependence of the electroluminescence on the current density.

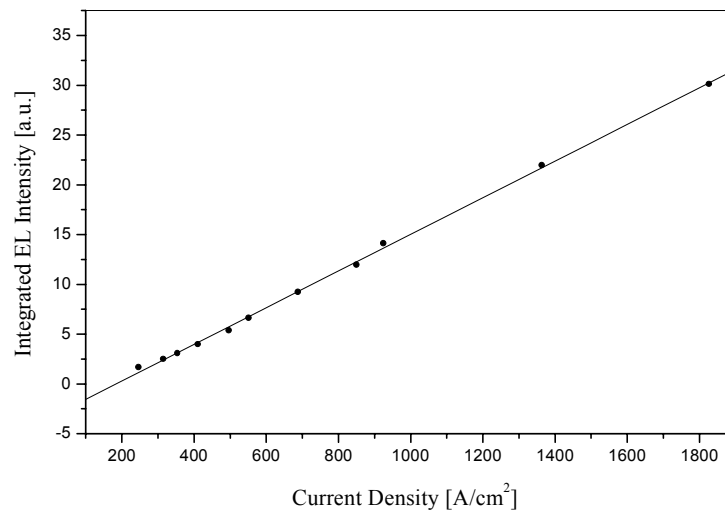


Figure 101: Integrated electroluminescence against the applied current density.

For convenience, Figure 101 also shows the integrated electroluminescence of both SiGe bands. No saturation is visible, though a current density of more than 1800 A/cm² was used. This indicates a very high quality of the diode itself with no deterioration in the contacts.

5.4. Electroluminescence

5.4.9. Power Efficiency

The external quantum efficiency is defined as the ratio of the electrical power input- to the optical power output. The optical power is given by

$$OP = \frac{\text{measured lockin signal [mV]}}{\text{responsivity} \cdot \text{spectral response}}.$$

For determining the quantum efficiency of the LED, a nitrogen cooled Northcoast Ge-detector (type EO-817L) was used. As the detector was only equipped with an integrated preamplifier, the typical responsivity is $5 \cdot 10^9$ V/W. The spectral response at $\sim 1.3 \mu\text{m}$ is about 50% of the peaked value. For the calculation of the optical losses from the sample to the detector it can be assumed that most of the intensity would be measured within a 60° collecting angle as shown in Figure 102. This is geometrically determined ($\tan \omega = 1/2$) by a distance of the sample to the collimating lens of about 40 mm and a radius of the lens of about 23 mm. The solid angle Ω is given by

$$\Omega = 2 \cdot \pi \cdot (1 - \cos \omega).$$

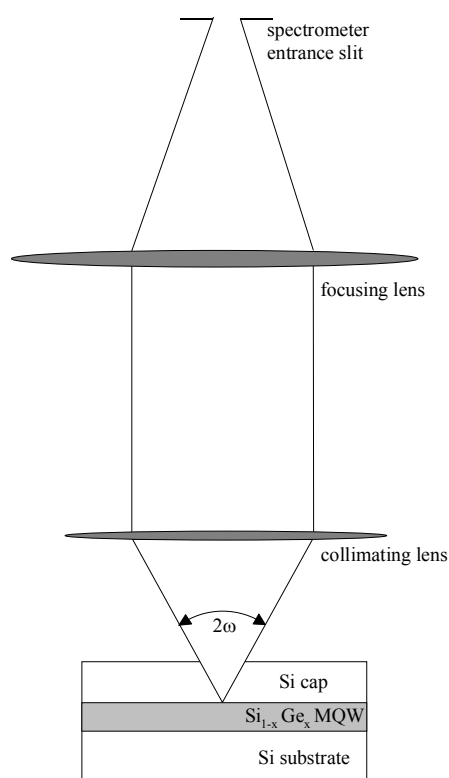


Figure 102: Schematic representation of the geometry used in this work to determine the external quantum efficiency of the LED.

5.4. Electroluminescence

Thus with $\omega=30^\circ$ one obtains $\Omega=0.84$ (full solid angle= 4π). Only 6.7% of the emitted light can be collected through the collimating lens in front of the cryostat, reaches the entrance slit of the spectrometer and thus can be registered by the detector. The measured electrical signal must therefore be corrected by a factor of 15 to compensate for this geometrical effect. Accounting for this geometrical effect the real optical output power is given by

$$OP_{real} = 15 \cdot OP.$$

The power efficiency is then determined by

$$PE = \frac{OP_{real}}{\text{input electrical power}}.$$

Having a driving current $I=575\text{mA}$, a driving voltage of 2.1V and a lockin signal of 4.2mV at $1.3\mu\text{m}$ one obtains an optical power of $1.68 \cdot 10^{-12}\text{W}$ for the $\text{Si}_{1-x}\text{Ge}_x/\text{ITO}$ LED. OP_{real} is given as $15 \cdot OP = 2.52 \cdot 10^{-11}\text{W}$. The power efficiency spectrally resolved at $1.3\mu\text{m}$ is thus given by $2.1 \cdot 10^{-11}$. As shown in Figure 96 it is important to account for the spectral distribution of the SiGe emission. The ratio of the integrated SiGe luminescence to the peak intensity at $1.3\mu\text{m}$ is 79. As up to now only the power efficiency at $1.3\mu\text{m}$ was accounted for, the value has to be corrected by a factor 79 (see Figure 96) resulting in a final power efficiency $PE = 1.7 \cdot 10^{-9}$.

One has to remark that the estimate of the geometrical converting factor is crucial. As every group is using its own way, this is why a large spread of efficiency values can be found in the literature.

For a grainy ITO layer the refractive index is commonly about 2.5. However, as our ITO layers consist mainly of voids, the refractive index determined by ellipsometry was only between 1.02 and 1.08 in the visible range up to about 1000nm. The ellipsometry characterisation was performed by D. Lebedev at the Lehrstuhl für Mikrostrukturtechnik, FB 13 Elektronik, University of Wuppertal. Without data available in the near-IR range, one can thus neglect internal reflections of the near-IR light emitted from the diode. Thus, no further correction with respect to such losses were performed for the power efficiency calculation.

6. Conclusions and Outlook

This thesis mainly addresses two aspects. The first part deals with the structural and optical characterisation of Si/SiGe multiple quantum wells. In particular the influence of Ge-cluster within the SiGe layers and the influence of the SiGe/Si interface roughness on photoluminescence was examined.

To increase the external quantum efficiency of Si/SiGe light emitting diodes, in the second part of this work the use of the ternary alloy Indium-Tin-Oxide (ITO) as a top-contact for Si/SiGe LEDs was demonstrated.

To this end, x-ray reflectivity, diffraction and topography, secondary electron mass spectroscopy, transmission electron microscopy, photoluminescence and Raman spectroscopy were used. The different characterisation techniques added value to each other and enabled a proof of the results in different ways. In the present work five different aspects were treated:

- 1) In the first part the design of a Si/SiGe multiple quantum well was optimised to achieve photo- and electroluminescence at room temperature. A 4 nm quantum well leads to a sufficient confinement of carriers, so that despite strong thermal quenching the luminescence was still preserved up to room temperature.
- 2) In the second part of the work it was demonstrated that, contrary to some recent controversial data of another research group [10-11], the formation of Ge clusters within the SiGe alloy did not lead to a reduction of the photoluminescence. This Hitachi research group assumed, that the formation of Ge clusters at a higher Ge segregation length in a temperature range between 400 and 650 °C would lead to a strong reduction of the photoluminescence. This was explained by assuming that the present s-like states would be transferred into p-like states as a result of the local change in crystal symmetry, leading to a drastic reduction of dipole transitions and of the radiative recombination rate. However, within the frame of the experiments performed in this work, static displacements of even 7% of the SiGe lattice parameter within the SiGe layers, caused by Ge concentration fluctuations, did have no significant effect on the photoluminescence. Thus, we assume that defects and impurities lead to the observed damping of photoluminescence.
- 3) In the third part of the thesis possible effects of exciton scattering and localisation at rough SiGe/Si interfaces were studied. The interface roughness was found to have a rather weak effect on the photoluminescence properties. Only in the case of extremely

6. Conclusions and Outlook

rough interfaces interfacial potential fluctuations can localise excitons and can therefore lead to a slight shift of the photoluminescence of about 8 meV to higher energies. The relevant length scale here is the exciton Bohr radius. For lateral interfacial fluctuations smaller than the exciton Bohr radius, the excitonic wavefunction simply averages over these fluctuations without being affected. In the case of very large fluctuations of the order of the Bohr radius, for SiGe approximately 7-8 nm, a clear confinement effect is present in the form of a shift of the photoluminescence to higher energies with increasing power density. It would be extremely interesting for further research to have a whole series of samples with different interface roughnesses. In this way it would even be possible to determine the exact onset of the relevant length scale.

- 4) In the fourth part of this work the origin of defect-luminescence in group-IV semiconductor heterostructures was discussed briefly. Presently the significance of a metallic decoration of dislocations in Si crystals is hotly debated. In this work it was shown, that in addition to the presence of dislocations a metallic decoration such as iron is necessary to induce radiative recombination at such dislocations.
- 5) To increase the external quantum efficiency of Si/SiGe LEDs, in the final part of this work a Si/SiGe light emitting diode (LED) was fabricated using the ternary alloy Indium-tin-Oxide (ITO) as the top ohmic contact for group-IV heterostructures. To our knowledge it was the first Si/SiGe LED using an ITO top contact. An important step relied on the set-up of a high-vacuum thermal evaporation chamber in cooperation with the company “MBE Komponenten”. ITO films with a transparency of about 90% in the visible spectral range and with a transparency of 60-80% in the range 1.2 - 1.3 μm were realised. This is the range of interest since here the Si/SiGe LED has its electroluminescence maximum. These films have a sheet resistance of about 2000 $\mu\Omega\text{cm}$. Due to a strong hole confinement within the SiGe quantum wells, electroluminescence was obtained up to room temperature. However, only a very low external power efficiency of 10^{-9} could be demonstrated. In this work it could be demonstrated, that using a simple technique ohmic contacts for the use for LEDs could be fabricated. Through this, the conventional metallic contacts with a high absorption can be replaced by ITO contacts with only weak absorption. As the growth of ITO is rather independent of the underlying substrate, it can as well be used as a transparent contact for III-V alloys.

6. Conclusions and Outlook

With respect to the strong thermal quenching of the PL and EL of Si/Si_{1-x}Ge_x based heterostructures, such LEDs are not really expected to be efficient enough to be applicable in real circuits at room temperature.

However, the progress of structural optimisation together with further increase of carrier confinement in lower than three dimensional nanostructures, such as quantum dots, gives hope to some brighter future. In the ideal case, to reduce non-radiative Auger recombination as much as possible, one would like to have only one exciton per dot. This comprises, that the density of the islands has to be increased by several orders of magnitude.

Furthermore, using ITO alloys can additionally improve the efficiency as one would avoid the undesired optical absorption by the commonly used metallic contacts. However, the fragile, dendritic structure of ITO films, as grown in this work, does not look very promising for device application with respect to mechanical stability, though the existence of a grainy interfacial layer enables a constant current injection of the previously percolating current over the whole surface covered with ITO.

For future experiments it seems to be essential to find a parameter range for ITO deposition, where the layers grow in the common grainy structure. It is believed from these preliminary tests, that one would need higher deposition rates of about some nm/sec and a smaller oxygen partial pressure. Both conditions can be easily realised and would only require a sophisticated parameter characterisation.

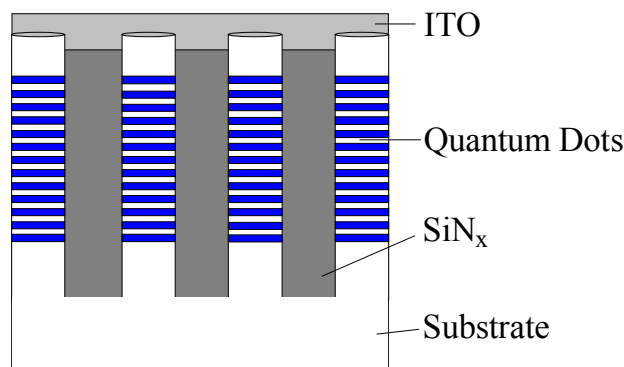


Figure 103: Schematic viewgraph of a series of quantum dots fabricated by electron-beam lithography and reactive ion etching. Prior to the ITO deposition the voids are filled by SiN_x as an electrical isolation.

Once this is achieved, one could use ITO as a top contact for Si/SiGe quantum dots, fabricated by e-beam lithography and reactive ion etching as schematically shown in Figure 103.

References

- 1 L. T. Canham, *Appl. Phys. Lett.* **57**, 1046-1048 (1990).
- 2 A. G. Cullis and L. T. Canham, *Nature* **353**, 335-338 (1991).
- 3 V. P. Kesan, E. Bassous, P. Munguia, S. F. Pesarcik, M. Freeman, and S. S. Iyer, *J. Vac. Sci. Technol. A* **11**, 1736-1738 (1993).
- 4 J. Stimmer, A. Reittinger, J. F. Nützel, G. Abstreiter, H. Holzbrecher, and C. Buchal, *Appl. Phys. Lett.* **68**, 3290 (1996).
- 5 M. Q. Huda, A. R. Peaker, J. H. Evans-Freeman, D. C. Houghton, and G. W.P., *Electronic Letters* **33**, 1182-1183 (1997).
- 6 W.-X. Ni, K. B. Joelsson, C.-X. Du, I. A. Buyanova, G. Pozina, W. M. Chen, G. V. Hansson, B. Monemar, J. Cardenas, and B. G. Svensson, *Appl. Phys. Lett.* **70**, 3383-3385 (1997).
- 7 S. Coffa, G. Franzò, and F. Priolo, *MRS Bulletin* **23**, 25-32 (1998).
- 8 A. Schuppen, U. Erben, A. Gruhle, H. Kibbel, H. Schumacher, and U. König, *Techn. Digest IEDM 95*, 742-746 (1995).
- 9 E. Ma, C. V. Thompson, and L. A. Clevenger, *J. Appl. Phys.* **69**, 2211-2218 (1991).
- 10 M. Miyao, K. Nakagawa, Y. Kimura, and M. Hirao, *Thin Solid Films* **294**, 204-207 (1997).
- 11 M. Miyao, K. Nakagawa, Y. Kimura, and M. Hirao, *J. Vac. Sci. Technol. B* **16**, 1529-1532 (1998).
- 12 K. Nakagawa and M. Miyao, *J. Appl. Phys.* **69**, 3058 (1991).
- 13 L. Pauling, *The nature of the chemical bond* (Cornell University Press, Ithaca, New York, 1960).
- 14 C. A. King, J. L. Hoyt, and J. F. Gibbons, *IEEE Trans. Electron Devices* **36**, 2093 (1989).
- 15 H. C. Liu, D. Landheer, M. Buchanan, and D. C. Houghton, *Appl. Phys. Lett.* **52**, 1809 (1988).

References

- 16 R. People, J. C. Bean, D. V. Lang, A. M. Sergent, H. L. Stromer, K. W. Wecht, R. T. Lynch, and K. Baldwin, *Appl. Phys. Lett.* **45**, 1231 (1984).
- 17 L. K. Bera, S. K. Ray, D. K. Nayak, N. Usami, Y. Shiraki, and C. K. Maiti, *J. of Electronic Materials* **28**, 98-104 (1999).
- 18 Y. H. Xie, E. A. Fitzgerald, D. Monroe, G. P. Watson, and P. J. Silverman, *Jpn. J. Appl. Phys* **33**, 2372 (1994).
- 19 B. S. Meyerson, E. Ganin, D. A. Smith, and T. N. Nguyen, *J. Electrochem. Soc.* **133**, 1232 (1986).
- 20 B. S. Meyerson, K. J. Uram, and F. K. LeGoues, *Appl. Phys. Lett.* **53**, 2555 (1988).
- 21 Y. Shiraki and S. Fukatsu, *Semicond. Sci. Technol.* **9**, 2017 (1994).
- 22 T. P. Sidiki, A. Rühm, W.-X. Ni, G. V. Hansson, and C. M. Sotomayor Torres, *Journal of Luminescence* **80**, 503-507 (1999).
- 23 W. B. d. Boer and D. J. Meyer, *Appl. Phys. Lett.* **58**, 1286-1288 (1991).
- 24 L. Vescan, W. Jäger, C. Dieker, K. Schmidt, A. Hartmann, and H. Lüth, *Mat. Res. Soc. Symp. Proc.* **263**, 23 (1992).
- 25 E. Kasper, H.-J. Herzog, and H. Kibbel, *Appl. Phys. Lett.* **8**, 199 (1975).
- 26 G. L. Patton, S. S. Iyer, S. L. Delage, S. Tiwari, and J. M. C. Stork, *IEEE Electron. Dev. Lett.* **9**, 165 (1988).
- 27 D.-X. Xu, G. D. Shen, M. Willander, W.-X. Ni, and G. V. Hansson, *Appl. Phys. Lett.* **52**, 2239 (1988).
- 28 T. Tatsumi, H. Hirayama, and N. Aizaki, *Appl. Phys. Lett.* **52**, 895 (1988).
- 29 H. Temkin, J. C. Bean, A. Antreasyan, and R. Leibenguth, *Appl. Phys. Lett.* **52**, 1089 (1988).
- 30 J. C. Bean, L. C. Feldman, L. C. Fiory, A. T. Nakahara, and I. K. Robinson, *J. Vac. Sci. Technol. A* **2**, 436 (1984).
- 31 F. W. Smith and G. Ghidini, *J. Electrochem. Soc.* **129**, 1300 (1982).
- 32 G. Ghidini and F. W. Smith, *J. Electrochem. Soc.* **131**, 2924 (1984).
- 33 T. O. Sedgwick, M. Berkenblitt, and T. S. Kuan, *Appl. Phys. Lett.* **54**, 2689 (1989).

References

- 34 R. People and S. A. Jackson, in *Strained layer superlattices: Physics; Vol. Chap. 4*, edited by T. P. Pearsall (Academic Press, Boston, 1991), p. 119-174.
- 35 J. W. Matthews, *J. Vac. Sci. Technol.* **12**, 126 (1975).
- 36 J. H. van der Merwe, *J. Appl. Phys.* **34**, 123 (1963).
- 37 R. People and J. C. Bean, *Appl. Phys. Lett.* **47**, 322 (1985).
- 38 F. C. Frank and J. H. Van der Merwe, *Proc. Roy. Soc. London A* **198**, 205 (1949).
- 39 E. Bauer, *Z. Kristallogr.* **110**, 430 (1958).
- 40 M. Volmer and A. Weber, *Z. Phys. Chem.* **119**, 227 (1926).
- 41 I. N. Stranski and L. Krastanow, *Akad. Wiss. Lit. Mainz Math.-Natur. Kl. Iib* **146**, 797 (1939).
- 42 H. Sunamura, S. Fukatsu, and Y. Shiraki, *Appl. Phys. Lett.* **66**, 953-955 (1995).
- 43 P. Schittenhelm, M. Gail, J. Brunner, J. F. Nützel, and G. Abstreiter, *Appl. Phys. Lett.* **67**, 1292-1294 (1995).
- 44 H. P. Zeindl and S. Nilsson, *J. Appl. Phys.* **77**, 1753-1757 (1995).
- 45 A. Souifi, T. Benyattou, G. Guillot, G. Brémond, D. Dutartre, and P. Warren, *J. Appl. Phys.* **76**, 4039-4045 (1995).
- 46 M. L. Cohen and T. L. Bergstresser, *Phys. Rev.* **141**, 789 (1966).
- 47 C. G. van de Walle and R. M. Martin, *Phys. Rev. B* **34**, 5621-5634 (1986).
- 48 R. People and J. C. Bean, *Appl. Phys. Lett.* **48**, 538 (1986).
- 49 L. Colombo, R. Resta, and S. Baroni, *Phys. Rev. B* **44**, 5572-5579 (1991).
- 50 W.-X. Ni, J. Knall, and G. V. Hansson, *Phys. Rev. B* **36**, 7744-7747 (1987).
- 51 K. Nauka, T. I. Kamins, J. E. Turner, C. A. King, J. L. Hoyt, and J. F. Gibbons, *Appl. Phys. Lett.* **60**, 195 (1992).
- 52 L. Vescan, R. Apetz, and H. Lüth, *J. Appl. Phys.* **73**, 7427 (1993).
- 53 K. Schmalz, I. N. Yassievich, H. Rucker, H. G. Grimmeiss, H. Frankenfeld, W. Mehr, H. J. Osten, P. Schley, and H. P. Zeindl, *Phys. Rev. B* **50**, 14287 (1994).
- 54 D. J. Robbins, L. T. Canham, S. J. Barnett, A. D. Pitt, and P. Calcott, *J. Appl. Phys.* **71**, 1407 (1992).

References

- 55 D. V. Lang, R. People, J. C. Bean, and A. M. Sergent, *Appl. Phys. Lett.* **47**, 1333-1335 (1985).
- 56 D. Dutartre, G. Brémond, A. Souifi, and T. Benyattou, *Phys. Rev. B* **44**, 11525-11527 (1991).
- 57 J. Weber and I. Alonso, *Phys. Rev. B* **40**, 5683 (1989).
- 58 Y. P. Varshni, *Physica* **34**, 149 (1967).
- 59 C. D. Thurmond, *J. Electrochem. Soc.* **122**, 1133 (1975).
- 60 C. Weisbuch and B. Vinter, *Quantum Semiconductor Structures* (Academic Press, Boston, 1991).
- 61 *Physics Of Nanostructures; Vol. 38*, edited by J. H. Davies and A. R. Long (SUSSP, 1991).
- 62 G. Schmidt, W. Langheinrich, and K. Heime, *Solid State Electr.* **37**, 587 (1994).
- 63 J. N. Randall and J. H. Luscombe, in *VLSI Electronics: Microstructure Science; Vol. 24, Chap. 13*, edited by N. G. Einspruch and W. R. Frensley (Academic Press, Inc, San Diego, 1994), p. 419-445.
- 64 Y. S. Tang, C. M. Sotomayor Torres, R. A. Kubiak, T. E. Whall, E. H. C. Parker, H. Presting, and H. Kibbel, *J. of Electr. Mat.* **24**, 99 (1995).
- 65 G. Bai, K. H. Kim, and M.-A. Nicolet, *Appl. Phys. Lett.* **57**, 2247 (1990).
- 66 J. Brunner, P. Schittenhelm, J. Gonderman, B. Spangenberg, B. Hadam, T. Köster, H. G. Roskos, H. Kurz, H. Gossner, I. Eisele, and G. Abstreiter, *J. Cryst. Growth* **150**, 1060 (1995).
- 67 E. Hammerl, F. Wittmann, J. Messarosch, I. Eisele, V. Huber, and H. Oppolzer, *Mater. Res. Soc. Symp. Proc.* **220**, 27 (1991).
- 68 A. Hartmann, L. Vescan, C. Dieker, and H. Lüth, *Mater. Sci. and Technol.* **11**, 410 (1995).
- 69 A. Hartmann, C. Dieker, R. Loo, L. Vescan, H. Lüth, and U. Bangert, *Appl. Phys. Lett.* **67**, 1888 (1995).
- 70 S. C. Jain, *Germanium - Silicon Strained Layers and Heterostructures* (ACADEMIC PRESS, Boston, 1994).

References

- 71 *Group IV compounds; Vol. 33*, edited by E. Kasper and F. Schäffler (Academic Press, Boston, 1991).
- 72 L. Vescan, *Appl. Phys. Lett.* **60**, 2183 (1992).
- 73 X. Xiao, *Appl. Phys. Lett.* **60**, 2135 (1992).
- 74 S. Fukatsu, H. Yoshida, A. Fujiwara, Y. Takahashi, Y. Shiraki, and R. Ito, *Appl. Phys. Lett.* **61**, 804 (1992).
- 75 A. Rühm, T. P. Sidiki, W. B. de Boer, W.-X. Ni, T. Köpke, and C. M. Sotomayor Torres, in *A study of growth temperature on interface quality and luminescence of Si/Si_{1-x}Ge_x multiple-quantum wells*, Castelvechio Pascoli, Italy, 1998 (TMS).
- 76 Y. Shiraki, H. Sunamura, S. Fukatsu, and N. Usami, *Electrochemical Society Proceedings* **95-17**, 31-36 (1995).
- 77 Y. S. Tang, C. D. W. Wilkinsin, C. M. Sotomayor Torres, D. W. Smith, T. E. Whall, and E. H. C. Parker, *Superlatt. and Microstruct.* **12**, 535 (1992).
- 78 J. Gondermann, B. Spangenberg, T. Köster, B. Hadam, H. G. Roskos, H. Kurz, J. Brunner, P. Schittenhelm, G. Abstreiter, H. Goßner, and I. Eisele, *Microelectronic Eng.* **27**, 83-86 (1995).
- 79 J. Brunner, W. Jung, P. Schittenhelm, M. Gail, G. Abstreiter, J. Gonderman, B. Hadam, T. Koester, B. Spangenberg, H. G. Roskos, H. Kurz, H. Gossner, and I. Eisele, *J. Cryst. Growth* **157**, 270-275 (1995).
- 80 T. Köster, B. Hadam, J. Gondermann, B. Spangenberg, H. G. Roskos, H. Kurz, J. Brunner, and G. Abstreiter, *Microelectronic Eng.* **30**, 341-344 (1996).
- 81 L. Vescan, C. Dieker, A. Souifi, and T. Stoica, *J. Appl. Phys.* **81**, 6709-6715 (1997).
- 82 Y.-S. Tang, C. D. W. Wilkinson, C. M. Sotomayor Torres, D. W. Smith, T. E. Whall, and E. H. C. Parker, *Solid State Communications* **85**, 199-202 (1993).
- 83 Y. S. Tang, C. M. Sotomayor Torres, T. E. Whall, E. H. C. Parker, H. Presting, and H. Kibbel, *Materials in Electronics* **6**, 356 (1995).
- 84 H. Sunamura, N. Usami, Y. Shiraki, and S. Fukatsu, *Appl. Phys. Lett.* **66**, 3024 (1995).

References

- 85 G. Abstreiter, P. Schittenhelm, C. Engel, E. Silveira, A. Zrenner, D. Meertens, and W. Jäger, *Semicond. Sci. Technol.* **11**, 1521 (1996).
- 86 K. Amano, M. Kobayashi, A. Ohga, T. Hattori, N. Usami, and Y. Shiraki, *Semicond. Sci. Technol.* **13**, 1277-1283 (1998).
- 87 W.-X. Ni, J. Birch, Y.-S. Tang, K. B. Joelsson, C. M. Sotomayor Torres, Å. Kvik, and G. V. Hansson, *Thin Solid Films* **294**, 300 (1997).
- 88 A. A. Darhuber, T. Grill, J. Stangl, G. Bauer, D. J. Lockwood, J.-P. Noël, P. D. Wang, and C. M. Sotomayor Torres, *Phys. Rev. B* **58**, 4825-4831 (1998).
- 89 R. Hull and J. C. Bean, *Appl. Phys. Lett.* **55**, 1900 (1980).
- 90 D. B. Noble, J. L. Hoyt, J. F. Gibbons, M. P. Scott, S. S. Laderman, S. J. Rosner, and T. I. Kamins, *Appl. Phys. Lett.* **55**, 1978 (1989).
- 91 G. F. A. van de Walle, L. J. van Ijzendoorn, A. A. van Gorkum, R. A. van den Heuvel, and A. M. L. Theunissen, *Semicond. Sci. & Technol.* **5**, 345 (1990).
- 92 R. Hull and J. C. Bean, *CRC Solid St. Mater. Sc.* **17**, 507 (1992).
- 93 D. C. Houghton, *J. Appl. Phys.* **70**, 2136 (1991).
- 94 L. B. Freund, *MRS Bull.* **XVII**, 52 (1992).
- 95 J. Y. Tsao and B. W. Dodson, *Appl. Phys. Lett.* **53**, 848 (1988).
- 96 L. Vescan, T. Stoica, C. Dieker, and H. Lüth, *Mat. Res. Soc. Symp. Proc.* **298**, 45 (1993).
- 97 J. W. Matthews and A. E. Blakeslee, *J. Crystal Growth* **27**, 118 (1974).
- 98 A. Benninghoven, F. G. Rüdener, and H. W. Werner, *Secondary ion mass spectrometry* (John Wiley & Sons, New York, 1987).
- 99 C. M. Wolfe, H. J. N., and G. E. Stillman, *Physical Properties of Semiconductors* (Prentice-Hall, New Jersey, 1989).
- 100 V. P. Varshni, *Phys. Stat. Solidi* **19**, 459 (1967).
- 101 W. P. Dumke, *Phys. Rev.* **105**, 139 (1957).
- 102 W. Heitler, *The Quantum Theory of Radiation* (Oxford University Press, Oxford, 1944).

References

- 103 G. Bremond, A. Souifi, T. Benyattou, and D. Dutartre, *Thin Solid Films* **222**, 60 (1992).
- 104 L. C. Lenchyshyn, L. W. Thewalt, J. C. Sturm, P. V. Schwartz, E. J. Prinz, N. L. Rowell, J.-P. Noël, and D. C. Houghton, *Appl. Phys. Lett.* **60**, 3174-3176 (1992).
- 105 J. F. Nützel, C. M. Engelhardt, and G. Abstreiter, in *Properties of Strained and Relaxed Silicon Germanium; Vol. 12*, edited by E. Kasper (INSPEC, London, 1995).
- 106 M. Rieger and P. Vogl, *Phys. Rev. B* **48**, 14276 (1993).
- 107 R. Loo, L. Vescan, A. Hartmann, R. Aprtz, U. Zastrow, T. Schäpers, A. Leuther, C. Dieker, and H. Lüth, *Phys. Rev. B* **50**, 18113-18123 (1994).
- 108 J. Humlíček, in *Properties of Strained and relaxed Silicon Germanium*, edited by E. Kasper (INSPEC, London, 1995).
- 109 Y. A. Pokrovskii, *Stat. Sol. (a)* **11**, 385 (1972).
- 110 R. B. Hammond, T. C. McGill, and J. W. Mayer, *Phys. Rev. B* **13**, 3566 (1976).
- 111 G. A. Thomas, T. M. Rice, and J. C. Hensel, *Phys. Rev. Lett.* **33**, 219 (1974).
- 112 D. J. Lockwood, G. C. Aers, L. B. Allard, B. Bryskiewicz, S. Charbonneau, D. C. Houghton, J. P. McCaffrey, and A. Wang, *Can. J. Phys.* **70**, 1184 (1992).
- 113 D. C. Houghton, J.-P. Noël, and N. L. Rowell, *Mat. Sci. Eng. B* **9**, 237 (1991).
- 114 J.-P. Noël, N. L. Rowell, D. C. Houghton, and D. D. Perovic, *Appl. Phys. Lett.* **57**, 1037 (1993).
- 115 A. Hartmann, L. Vescan, C. Dieker, T. Stoica, and H. Lüth, *Phys. Rev. B* **48**, 18279 (1993).
- 116 G. Abstreiter, E. Bauser, A. Fisher, and K. Ploog, *Appl. Phys.* **16**, 345 (1978).
- 117 M. Cardona, , 1987, p. 2.
- 118 P. M. Mooney, F. H. Dacol, J. C. Tsang, and J. O. Chu, *Appl. Phys. Lett.* **62**, 2069 (1993).
- 119 F. Cerdeira, A. Pinczuk, J. Bean, B. Batlogg, and B. A. Wilson, *Appl. Phys. Lett.* **45**, 1138 (1984).
- 120 M. A. Renucci, J. B. Renucci, and M. Cardona, in *Light Scattering in Solids*, Paris, 1971 (Flammarion), p. p. 326.

References

- 121 M. I. Alonso and K. Winer, *Phys. Rev. B* **39**, 10056-10062 (1989).
- 122 J. C. Tsang, P. M. Mooney, F. Dacol, and J. O. Chu, *J. Appl. Phys.* **75**, 8098-8108 (1994).
- 123 A. H. Compton and K. Allison, *X-Rays in Theory and Experiment* (Nostrand Inc., D.v., New York, 1935).
- 124 H. Dosch, , Vol. 126 (Springer Verlag, 1992).
- 125 G. H. Vineyard, *Phys. Rev. B* **26**, 4146 (1982).
- 126 S. Dietrich and H. Wagner, *Z. Phys. B* **56**, 207 (1984).
- 127 S. Dietrich and A. Haase, *Physics Reports* **Vol. 260 Nr. 1&2** (1995).
- 128 W. K. H. Panofski and M. Phillips, *Classical Electricity and Magnetism* (London, 1962).
- 129 J. Als-Nielsen, *Structure and Dynamics of Surfaces II*, Vol. 43 (Springer, 1987).
- 130 L. Névot and P. Croce, *Revue Phys. Appl.* **15**, 761-779 (1979).
- 131 L. G. Parratt, *Phys. Rev.* **95**, 359 (1954).
- 132 T. P. Sidiki, in *Physics, Chemistry and Application of Nanostructures*, edited by V. E. Borisenko, S. V. Gaponenko, A. B. Filonov, and V. S. Gurin (World Scientific, Singapore, 1999), p. 140-144.
- 133 D. Chescoe and P. J. Goodhew, *The operation of transmission and scanning electron micoscopes* (Oxford University Press, Oxford, 1990).
- 134 L. C. Feldman and J. C. Mayer, *Fundamentals of surface and thin film analysis* (Elsevier Science Publishing, Amsterdam, 1986).
- 135 M. P. Hirsh, A. Howie, R. B. Nicholson, and D. W. Pashley, *Electron microscopy of thin crystals* (Butterworths, London, 1971).
- 136 P. Nath, R. F. Bunshah, B. M. Basol, and O. M. Staffsud, *Thin Solid Films* **72**, 463-468 (1980).
- 137 J. L. Yao, S. Hao, and J. S. Wilkinson, *Thin Solid Films* **189**, 227-233 (1990).
- 138 R. Latz, K. Michael, and M. Scherer, *Jpn. J. Appl. Phys.* **30**, 149-151 (1991).
- 139 H. Köstlin, R. Jost, and W. Lems, *Phys. Stat. Sol. (a)* **29**, 87-93 (1975).

References

- 140 T. Köpke, Thesis, Wuppertal, 1998.
- 141 L. Davis, *Thin Solid Films* **90**, 323-326 (1993).
- 142 R. N. Joshi, V. P. Singh, and J. C. McClure, *Thin Solid Films* **257**, 32-35 (1995).
- 143 J. Kane, H. Schweitzer, and W. Kern, *Thin Solid Films* **29**, 155 (1975).
- 144 A. Hjortsberg, I. Hamberg, and C. G. Granqvist, *Thin Solid Films* **90**, 323-326 (1982).
- 145 H. L. Ma, D. H. Zhang, P. Ma, S. Z. Win, and S. Y. Li, *Thin Solid Films* **236**, 105-110 (1995).
- 146 R. W. Berry, P. M. Hall, and M. T. Harris, *Thin film technology* (van Nostrand Reinhold, 1968).
- 147 S. M. Sze, *Physics of Semiconductor Devices*, second edition ed. (John Wiley & Sons, New York, 1981).
- 148 J. C. C. Tsai, in *VLSI Technology*, second edition ed., edited by S. M. Sze (McGraw-Hill, New York, 1988), p. 272.
- 149 W. M. Chen, I. A. Buyanova, W.-X. Ni, G. V. Hansson, and B. Monemar, *Phys. Rev. Lett.* **77**, 4214 (1996).
- 150 F. Priolo, G. Francò, S. Coffa, A. Polman, S. Libertino, R. Barklie, and D. Carey, *J. Appl. Phys.* **78**, 3874-3882 (1995).
- 151 T. Fromherz and G. Bauer, in *Properties of Strained and relaxed Silicon Germanium*, edited by E. Kasper (INSPEC, London, 1995), p. 87-93.
- 152 L. A. Nagahara, P. I. Oden, A. Majumdar, J. P. Carrejo, J. Graham, and K. Alexander, *Proc. SPIE* **1639**, 171 (1992).
- 153 P. A. Coon, P. Gupta, M. L. Wise, and S. M. Goerge, *J. Vac. Sci. Technol. A* **10**, 324 (1992).
- 154 S. T. Lai and M. V. Klein, *Phys. Rev. B* **29**, 3217 (1984).
- 155 M. Queslati, M. Zouaghi, M. E. Pistol, L. Samuelson, H. G. Grimmeiss, and M. Balkanski, *Phys. Rev. B* **32** (1985).
- 156 S. Kalem, T. Curtis, W. B. de Boer, and G. E. Stillman, *Appl. Phys. A* **66**, 23-27 (1998).

References

- 157 N. A. Drozdov, A. A. Patrin, and V. D. Tkachev, *Phys. Stat. Solidi (b)* **83**, 137 (1977).
- 158 R. Sauer, C. Kisielowski-Kemmerich, and H. Alexander, *Phys. Rev. Lett.* **57**, 1472 (1985).
- 159 H. Lee and S.-H. Choi, *J. Appl. Phys.* **85**, 1771-1774 (1999).
- 160 M. Suezawa, Y. Sasaki, and K. Sumino, *Phys. Stat. Solidi (a)* **79**, 173 (1983).
- 161 R. Sauer, J. Weber, J. Stolz, E. R. Weber, K.-H. Kusters, and H. Alexander, *Appl. Phys. A* **36**, 1 (1985).
- 162 M. Suezawa and K. Sumino, *Phys. Stat. Solidi (a)* **78**, 639 (1983).
- 163 M. Suezawa, S. Y., Y. Nishina, and K. Sumino, *Jpn. J. Appl. Phys.* **20**, 537 (1981).
- 164 K. Weronek, J. Weber, A. Hopner, F. Ernst, R. Buchner, M. Stefaniak, and H. Alexander, *Mater. Sci. Forum* **83-87**, 1315 (1992).
- 165 V. Higgs, L. E.C., C. E. Norman, and P. C. Kightley, *Mater. Sci. Forum* **83-87**, 1309 (1992).
- 166 V. Higgs, C. E. Norman, E. C. Lightowlers, and P. C. Kightley, in *Proceedings of the 20th International Conference on the Physics of Semiconductors*, edited by A. E.M. and J. D. Joannopoulos (World Scientific, Singapore, 1990).
- 167 V. Higgs, E. C. Lightowlers, and P. C. Kightley, *Mat. Res. Soc. Symp. Proc.* **163**, 57 (1990).
- 168 I. Yonenaga and K. Sumino, *J. Appl. Phys.* **80**, 3244 (1996).
- 169 J. C. Sturm, H. Manoharan, L. C. Lenchyshyn, M. L. W. Thewalt, N. L. Rowell, J.-P. Noël, and D. C. Houghton, *Phys. Rev. Lett.* **66**, 1362 (1991).
- 170 G. S. Higashi and Y. J. Chabal, in *Handbook of Semiconductor Wafer Cleaning Technology; Vol. Chap.10*, edited by W. Kern (Noyes Publications, Park Ridge, New Jersey, 1993), p. 433-496.

Acknowledgements

I wish to express my sincere thanks to a number of friends and colleagues who have strongly influenced and encouraged me during my Ph.D studies. Without their efforts, this thesis would not have been completed.

- Prof. Dr. Clivia M. Sotomayor Torres, my supervisor, not only for three years of close collaboration, constant encouragement, creative criticism and stimulating guidance throughout the work, but also for a wonderful time and an unforgettable experience both in scientific research and daily life.
- Prof. Dr. H. Lüth and Prof. Dr. A.R. Peaker for the kind offer to act as co-supervisors for my thesis.
- Dr. Wie-Xin Ni (Linköping University, Sweden) for the growth of the MBE wafers, for very helpful hints concerning the interpretation of the PL data, for being a friend during our collaboration and finally for the invitation to Linköping.
- Dr. Thomas Hoffmann for help in using scanning electron microscopy, invaluable discussions and constant support.
- Dr. Adrian Rühm for supporting me with x-ray reflectivity, performing some of the measurements and for many invaluable discussions in the data evaluation and modeling.
- Dr. Wiebe de Boer from Philips Research in Eindhoven for the growth of the RTCVD wafers and for performing the SIMS measurements.
- Dr. Silke Christiansen (Friedrich-Alexander-Universität, Erlangen, Germany) for performing the TEM measurements and for many fruitful discussion.
- Dr. Claudio Ferrari (CNR Maspec Institute, Parma 43100, Italy) for performing the x-ray topography images.
- Prof. Chris D.W. Wilkinson for inviting me to Glasgow and for giving me the opportunity to use the PL lab while the one in Wuppertal was being set up. Also Mr. A. Ross for all his technical assistance during this period.
- Dipl.-Phys. Thorsten Maka for many fruitful discussions, for his constant support and backup in solving many problems in the lab and for being a trustful friend during the whole PhD phase.
- Jens Uwe Bruch and Nils Roos for their excellent, continuous support in the lab, for many happy joint trading hours and for being friends during the whole time.

- Dipl.-Ing. Thorsten Köpke for the excellent pioneering work on the deposition of ITO films, that was of great help for me, for the fruitful discussion and for a nice working atmosphere in general.
- Sebastian Chabert for many nice discussions on SiGe and for his general help during the work on the diode fabrication.
- Ms. Carmen Runte, our Secretary, for giving me all support needed to survive the daily University life, for wonderful discussions around the scientific problems and for telling everybody about handling me credit cards and candles.
- The mechanical workshop (FB13) for fabricating much of the equipment used during this work.

A great thank to my parents, brother and sister for their understanding and support during the period. A special thank and a kiss to Simone Frömel, my girl-friend, for keeping my mind and my heart in a state of true happiness and also sometimes for such impatience that I was forced to go back to the world where human beings live.

Financial support, from the European Esprit project SIBLE and from the University of Wuppertal is acknowledged.

Hiermit versichere ich, die vorliegende Arbeit selbständig verfaßt und nur die angegebenen Quellen und Hilfsmittel verwendet zu haben.

Wuppertal, Dec. 07, 1999

Tamim P. Sidiki